République Algérienne Démocratique et Populaire
الجمهورية الجزائرية الديمقراطية الشعبية
Ministère de l'Enseignement Supérieur et de la Recherche Scientifique
وزارة التعليم العالي و البحث العلمي
Ecole Nationale Polytechnique
المدرسة الوطنية متعددة التقنيات

Département d'automatique

End of studies project thesis

For the attainment of the State Engineer's Degree in Control Engineering

Enhancing battery lifespan: estimation of Lithium-ion cells with « quasi-flat » voltage chemistry

Realized by:

ROUMANE Meriem Nihad

Publicly presented and defended on the 18th of September, 2023, before the jury composed of:

President	M.Mohamed TADJINE	École Nationale Polytechnique
Examiner	M. Djamel BOUDANA	École Nationale Polytechnique
Promoters	M. Djamel BOUKHETALA	École Nationale Polytechnique
	M. Romain POSTOYAN	CNRS, U. de Lorraine, CRAN
Guest	M. Pierre-Oliver LAMARE	SAFT

ENP 2023

République Algérienne Démocratique et Populaire
الجمهورية الجزائرية الديمقراطية الشعبية
Ministère de l'Enseignement Supérieur et de la Recherche Scientifique
وزارة التعليم العالي و البحث العلمي
Ecole Nationale Polytechnique
المدرسة الوطنية متعددة التقنيات

Département d'automatique

End of studies project thesis

For the attainment of the State Engineer's Degree in Control Engineering

Enhancing battery lifespan: estimation of Lithium-ion cells with « quasi-flat » voltage chemistry

Realized by:

ROUMANE Meriem Nihad

Publicly presented and defended on the 18th of September, 2023, before the jury composed of:

President	M.Mohamed TADJINE	École Nationale Polytechnique
Examiner	M. Djamel BOUDANA	École Nationale Polytechnique
Promoters	M. Djamel BOUKHETALA	École Nationale Polytechnique
	M. Romain POSTOYAN	CNRS, U. de Lorraine, CRAN
Guest	M. Pierre-Oliver LAMARE	SAFT

ENP 2023

République Algérienne Démocratique et Populaire
الجمهورية الجزائرية الديمقراطية الشعبية
Ministère de l'Enseignement Supérieur et de la Recherche Scientifique
وزارة التعليم العالي و البحث العلمي
Ecole Nationale Polytechnique
المدرسة الوطنية متعددة التقنيات

Département d'automatique

Mémoire de projet de fin d'études

Pour l'obtention du diplôme d'Ingénieur d'État en Automatique

Mieux connaître l'état des batteries pour augmenter leur durée de vie : estimation des cellules Lithium-ion dites à « chimie plate »

Réalisé par :

ROUMANE Meriem Nihad

Présenté et soutenu le 18 septembre 2023, devant le jury composé de :

Président	M.Mohamed TADJINE	École Nationale Polytechnique
Examinateur	M. Djamel BOUDANA	École Nationale Polytechnique
Promoteurs	M. Djamel BOUKHETALA	École Nationale Polytechnique
	M. Romain POSTOYAN	CNRS, U. de Lorraine, CRAN
Invité	M. Pierre-Olivier LAMARE	SAFT

ENP 2023

Dédicace

À la personne la plus précieuse à mon cœur, la plus chère de toutes, celle qui m'a comblé d'amour, d'encouragement, de douceur et de bonheur : ma maman. Sans toi, je n'aurais jamais pu accomplir tout cela. Je te serai éternellement reconnaissante,

À tous les membres de ma famille qui m'ont soutenu et encouragé, en particulier mes frères et ma sœur Manel à qui je souhaite tout le succès possible dans leur vie,

À ma meilleure amie, Meriem, qui a toujours été là pour moi, m'a constamment encouragé, soutenu, poussé vers le haut et m'a aimé inconditionnellement. Tu es une source inestimable de bonheur dans ma vie,

À tous mes amis et camarades de classe, même si je ne peux malheureusement pas tous les nommer, Amine, Thiziri, Khaled, Islem, Abdelhak, Maroua, Imane, et bien d'autres..., je tiens à exprimer ma profonde gratitude pour tout leur soutien et pour les moments incroyables que nous avons partagés ensemble,

À mes promoteurs Romain, Stéphane, Pierre-Olivier, Sébastien, ainsi qu'à tous mes collègues qui ont contribué à faire de mon expérience au sein du CRAN l'une des meilleures.

Au groupe Charmois qui m'a chaleureusement accueilli parmi eux et qui est devenu une véritable deuxième famille pour moi à Nancy,

À mes chers enseignants et tous ceux qui ont contribué à me guider vers une nouvelle étape de ma vie,

Merci.

Remerciements

Au tout début, je tiens à exprimer ma gratitude envers Allah le tout-puissant, source de toute force, en qui j'ai placé ma confiance et qui m'a donné la détermination nécessaire pour mener à bien mon travail.

Je tiens également à exprimer mes plus sincères remerciements à ma chère maman pour ses sacrifices incessants, son amour inconditionnel, ses précieux conseils, et ses encouragements constants. Sans elle, je n'aurais pas pu arriver là où je suis aujourd'hui.

Je tiens à exprimer ma profonde reconnaissance envers mes encadrants : Mr Romain POSTOYAN du CRAN, Mr Stéphane RAEL du GREEN, Mr Pierre-Olivier LAMARE et Mr Sébastien BENJAMIN de la SAFT, pour leur précieuse guidance, leur assistance inestimable, leur patience et leurs conseils avisés, ainsi que pour le temps généreusement consacré à mon projet. Je leur suis infiniment reconnaissante.

Je tiens également à exprimer ma gratitude envers mon encadrant et enseignant, Mr Djamel BOUKHETALA, pour son soutien constant, ses précieux conseils, ainsi que pour les cours précieux qu'il a dispensés dans ma spécialité. Mes remerciements vont également à l'ensemble des membres du jury, Mr Mohamed TADJINE et Mr Djamel BOUDANA, pour leurs efforts lors de l'évaluation de mon travail ainsi que leurs cours enrichissants.

Je remercie également toute l'équipe du CRAN pour leur accueil chaleureux et leur soutien.

Je souhaite également remercier chaleureusement tous mes chers amis en Algérie et à Charmois qui se reconnaitront. Vous êtes vraiment les meilleurs !

ملخص

مشروعنا يركز على التقدير الدقيق لمقدار شحن بطاريات ليثيوم فوسفات الحديد، المعروفة بضغط الدائرة المفتوحة شبه الثابت بالنسبة لمقدار الشحن، و الذي يمثل معاملا مهما لنظام إدارة البطارية. باستعمال نموذج لدائرة مكافئة، قمنا بتصميم مراقبين يعتمدون على الوضع المنزلق : مراقب كلاسيكي يضمن تقارب الخطأ في ناتج النظام إلى الصفر في وقت محدد، و مراقب بديل يعتمد على تقارب تقدير حالة ضغط الدائرة المفتوحة بالإضافة إلى خطأ الناتج. تم إجراء عمليات المحاكاة في البداية بافتراض المعاملات ثابتة. بعد ذلك، قمنا باختبار دقة المراقبين من خلال دمج قيم المعاملات الحقيقية و التي تختلف باختلاف تيار البطارية، درجة الحرارة و مقدار الشحن. يساهم هذا العمل في التطور في تقييم مقدار شحن بطاريات ليثيوم فوسفات الحديد، مما يعزز أداء نظام إدارة البطارية.

كلمات مفتاحية : بطاريات الليثيوم، بطاريات ليثيوم فوسفات الحديد، مقدار الشحن، ضغط الدائرة المفتوحة الثابت، نموذج الدائرة المكافئة، مراقب الوضع المنزلق، تقدير، تحليل ليابونوف، تحليل المتانة.

Résumé

Notre recherche se focalise sur l'estimation de l'état de charge des batteries LiFePO4, connues pour leur profil OCV constant par rapport à la SOC, un paramètre essentiel pour le BMS. Nous concevons deux observateurs en mode glissant, l'un mettant l'accent sur la convergence de l'erreur de tension terminale et l'autre sur la précision de l'estimée de l'OCV. Les simulations ont initialement utilisé des paramètres constants et ont ensuite été validées avec des valeurs réelles considérant les variations de courant, de température et de SOC. Ce travail contribue aux avancées dans l'estimation du SOC des batteries LiFePO4, améliorant ainsi les performances du BMS.

Mots clés : Batteries Lithium-ion, Batteries LiFePO4, état de charge (SOC), OCV plate, circuit électrique équivalent, observateur par mode de glissement, estimation, analyse de Lyapunov, robustesse.

Abstract

Our research focuses on SOC estimation for LiFePO4 batteries, known for their flat OCV profile across SOC values—a vital BMS parameter. We design two sliding mode observers, one emphasizing battery voltage error convergence and the other OCV estimate accuracy. Simulations initially used constant parameters and were later validated with real values accounting for current, temperature, and SOC variations. This work contributes to advancements in LFP batteries SOC estimation, enhancing BMS performance.

Keywords : Lithium-ion batteries, LiFePO4 batteries, state of charge (SOC), flat OCV, equivalent circuit model, sliding mode observer, estimation, Lyapunov analysis, robustness.

Contents

List of tables

List of figures

List of acronyms

BMS	Battery Management System
ECM	Equivalent Circuit Model
EV	Electric Vehicule
LFP	LiFePO4
OCV	Open Circuit Voltage
SMO	Sliding Mode Observer
SOC	State Of Charge

Preface

Preface

This internship, proposed by SAFT in collaboration with two laboratories of Université de Lorraine: CRAN "Centre de Recherche en Automatique de Nancy" and GREEN "Groupe de Recherche en Énergie Électrique de Nancy", is a coordination between the latters and the laboratory "Commande des Processus" of the National Polytechnic School of Algiers.
SAFT is a French company and a part of TotalEnergie. It specializes in advanced battery systems and has a history dating back to 1918. Their battery technologies include Lithium-ion, nickel-cadmium, and more. SAFT serves various industries, providing critical backup power, energy storage, and propulsion solutions. The company focuses on sustainability and collaborates with TotalEnergie to support clean energy initiatives. SAFT operates globally, emphasizing innovation and research to stay at the forefront of the energy storage industry. My supervisors from SAFT were: Pierre-Olivier LAMARE, research engineer and Sébastien BENJAMIN, manager of the battery management & modeling team.
CRAN (Centre de Recherche en Automatique de Nancy) is a CNRS-Université de Lorraine research unit in Nancy, France, specializing in automatic control and systems engineering. It collaborates with academic institutions and industries. My supervisor from CRAN was Romain POSTOYAN, researcher at CNRS.
GREEN (Groupe de Recherche en Énergie Électrique de Nancy) is a research group based in Nancy, France, focused on electrical energy research. Their work includes renewable energy technologies, power systems, grid integration, and energy efficiency. Affiliated with an academic institution, GREEN collaborates with various disciplines and industry partners, publishing research findings and participating in projects. They also contribute to educational initiatives, promoting knowledge dissemination and nurturing future experts in the field. My supervisor from GREEN was Stephane RAEL, professor at Université de Lorraine.

Introduction

Introduction

Lithium-ion batteries are becoming crucial for building a civilization that is both technologically advanced and sustainable. Lithium-ion batteries are used to power a wide range of portable devices as well as the rapidly expanding fleet of electric vehicles (EVs) throughout the world given their comparatively high energy density [1].

Benefits of Lithium-ion batteries include higher power density, quicker charging, no memory effect, lower maintenance, higher open-circuit voltage and longer lifespan compared to other rechargeable batteries like lead-acid (Pb), nickel-metal hydride (Ni-MH), and nickel-cadmium (Ni-Cd) batteries [11]. On the other hand, this technology requires a careful management for safety and reliability purposes. [3].

A well-designed battery management system (BMS) is necessary to enhance efficiency, reliability and safety by controlling and monitoring battery performance. One crucial variable for the BMS is the state of charge (SOC), which serves as the fuel gauge for the battery system. Accurate monitoring of SOC is particularly important for predicting the battery system's operating range and improving overall utilization efficiency. It also helps preventing overcharging and over-discharging of batteries. The SOC is an internal state that cannot be directly measured by a sensor. It appears that robustly estimating the SOC is challenging due to the battery nonlinear dynamics. This requires an elaborate algorithm based on external physical measurements.

In recent years, several techniques have been developed to estimate the SOC for Lithium-ion batteries. These techniques can be categorized into two groups. The first group includes the ampere-hour integration method, the open-circuit voltage method, and artificial intelligence-based methods [22, 21, 30] that do not rely on establishing a battery model and are not of closed-loop nature and thus are non-robust a priori. The ampere-hour integration approach is simple and easy to implement for SOC estimation. However, its accuracy is significantly affected by initial SOC errors and accumulated errors caused by measurement noise. The open circuit voltage (OCV) method estimates SOC based on the batteries OCV, but it requires a long rest time, making it impractical for electric vehicles (EVs) and hybrid electric vehicles (HEVs). Artificial intelligence methods, such as neural networks and fuzzy logic, can estimate SOC accurately due to their ability to handle nonlinear functions. However, these methods heavily rely on the quantity and quality of training data, and battery behavior patterns are random, making real-time implementation challenging [32]. The second group consists of model-based methods and

consists in first modeling the battery and then estimating its internal state using observers such as the Kalman filter (KF) and the sliding mode observer (SMO), and so on [32, 30, 29].

In this work, we focus on the second category of these estimation techniques.

One of the most notable advancements in Lithium-ion battery technology is the growing adoption of LiFePO4 batteries, which have gained significant interest in recent times. These lithium iron phosphate batteries, also known as LFP batteries, offer a multitude of distinct advantages when compared to other types of lithium-ion batteries. LFP batteries offer cost-effectiveness owing to the availability of iron and phosphate, setting them apart from other metal variants. Their distinct environmental advantage emerges from their reduced toxicity and enhanced eco-friendliness, due to the absence of cobalt or nickel content. Moreover, these batteries provide an extended lifecycle and demonstrate minimal power degradation over time, enhancing their overall reliability. However, it is important to acknowledge certain limitations of LFP batteries. Among these, a significant focus in our current study is their OCV-SOC curve, characterized by its flat profile across a wide range of SOC values. This distinctive feature poses a challenge in accurately estimating the battery state of charge, warranting careful consideration in our analysis. The objective of this work is to address this challenge, namely to develop an algorithm to estimate the SOC of LFP batteries.

This project is organized in four chapters as follows.

Chapter 1 is an introduction to Lithium-ion Batteries. In this chapter, we provide an overview of Lithium-ion batteries, aiming to familiarize the readers with this technology. We begin by explaining the operating principle of a Lithium-ion battery and defining its key components. Additionally, we delve into the advantages and disadvantages of this technology, focusing particularly on LiFePO4 batteries.

Chapter 2 explores various Lithium-ion battery models commonly used in literature to describe their behavior. The pros and cons of each model are discussed to provide a clear understanding of their strengths and limitations. Subsequently, we select a suitable model for our work, present its different parameters, and provide numerical simulation results.

Chapter 3 deals with the main objective of this project: the design of state-observers for the model selected in Chapter 2. Before that, we present in this chapter, a review of estimation techniques employed in literature. Furthermore, we introduce two distinct state observers that we have developed specifically for this purpose. The chapter includes numerical simulations of both methods, assuming constant parameters.

In Chapter 4, we address the challenge of non-constant parameters in the battery model obtained from the SAFT Matlab model. We demonstrate numerical simulations considering these variable parameters to provide a more realistic representation of the system's behavior. Finally, we will do a comparison of the two observers.

Finally, a conclusion that serves to provide a summary of the research undertaken and offers insights into future perspectives.

General knowledge of Lithium-ion batteries

Chapter 1

General knowledge of Lithium-ion batteries

In 1800, the Italian engineer Alessandro Giuseppe Antonio Anastasio Volta revolutionized the world of energy storage by inventing the first battery known as the voltaic pile. This groundbreaking innovation allowed for the storage and release of electric charge through a chemical reaction, marking a pivotal moment in the history of electrical science.

Since then, batteries have become an indispensable component, powering various electrical devices that have become an integral part of our daily lives.

In the automotive industry, the Lithium-ion energy storage system has emerged as the leading solution to meet the high demands for specific energy and specific power in electric vehicles (EVs) [18]. The numerous benefits of Lithium-ion batteries include higher power density, faster charging times, reduced memory effect, lower maintenance requirements, higher open-circuit voltage, and an extended lifespan compared to other rechargeable batteries like lead-acid (Pb), nickel-metal hydride (Ni-MH), and nickel-cadmium (Ni-Cd) batteries.

This chapter aims to delve into the functionality of lithium-ion batteries and present an overview of their advantages and disadvantages.

1.1 Composition

The battery is an electrochemical accumulator i.e., a device that stores electrical energy via a chemical reaction and which restores it in the form of current, made up of an anode, cathode, separator, electrolyte, and two current collectors as shown in Figure 1.1.

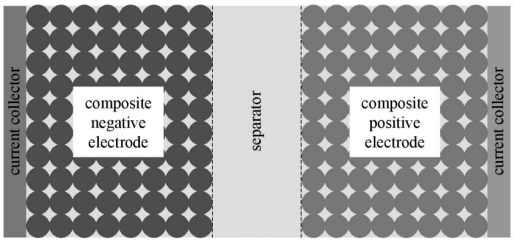

Figure 1.1: Constitution of a Lithium-ion battery, taken from [24].

An electrolyte is a substance containing mobile ions. It can be liquid or solid, organic or aqueous, what matters is that ions can move there. It is locally electrically neutral and does not leave past electrons. Electrolytes are usually associated with electrodes.

An electrode is a conductor in contact with an electrolyte, called a cathode when it hosts a reduction reaction and an anode when it hosts an oxidation reaction.

An oxidation-reduction reaction, or a redox reaction is the transfer of electrons between two chemical species. The oxidizing agent captures the electrons, the reducing agent yields them.

A separator is a type of polymeric membrane that is positioned between the two electrodes of an accumulator. This positioning helps prevent electrical short-circuiting.

A current collector is a bridging component that collects electrical current generated at the electrodes and connects with external circuits.

Now equipped with an understanding of the battery's components, we will explore its operating principle.

1.2 Operating principle

Lithium-ion batteries functioning is based on the "Rocking Chair" operating principle. The ions of lithium shift back and forth between the intercalation hosts of the cathode and anode through redox reactions. The back-and-forth movement of Li^+ ions reminds of the movement of a rocking chair.

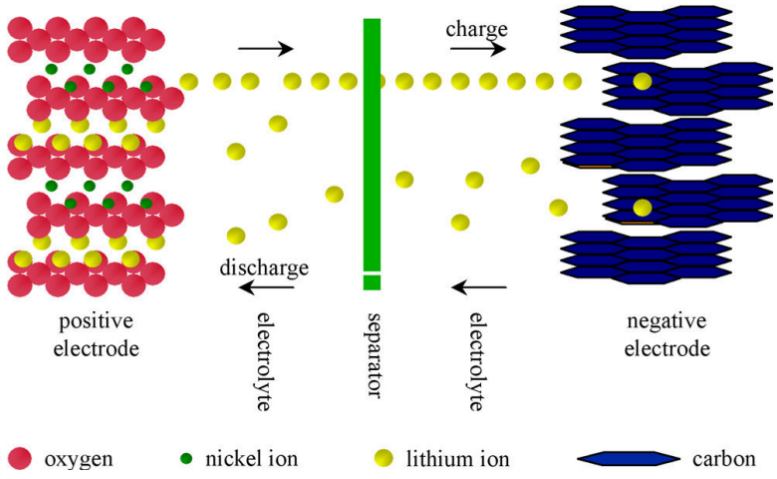

Figure 1.2: Lithium-ion battery operating principle, taken from [24].

The core of Lithium-ion battery operation lies in redox (reduction-oxidation) reactions. As stated in Section 1.1, redox reactions are an essential process for energy storage and

release. In the context of Lithium-ion batteries, these reactions occur within the cathode and anode materials.

- Charge Process: During the charging process, lithium ions move from the cathode to the anode. This involves the insertion of Li^+ ions into the host material of the negative electrode (anode), a process called intercalation. Simultaneously, lithium ions are deinserted from the host material of the positive electrode (cathode). These movements of lithium ions are crucial in restoring the battery's energy for future use.
- Discharge Process: When the battery discharges, the reverse process takes place. Lithium ions are inserted into the cathode material while being deinserted from the anode material. This flow of lithium ions releases stored energy, which is harnessed as electric current for external use.

The coordinated dance of these redox reactions is what powers the battery's operation, enabling it to store and release electrical energy efficiently. This "Rocking Chair" principle, with its back-and-forth movement of lithium ions, underlies the cyclic charge and discharge of lithium-ion batteries. Transitioning to the essential characteristics and challenges of Lithium-ion batteries, the upcoming section will provide a comprehensive exploration of the advantages and drawbacks associated with this technology.

1.3 Pros and cons of Lithium-ion batteries

Lithium-ion batteries have gained immense popularity due to their remarkable characteristics, but they also face certain limitations that warrant careful consideration. In this section, we will explore both the pros and cons of this technology.

1.3.1 Pros

- *High specific energy:* from 120 to 160 Wh/kg for energy cells. Specific energy refers to the amount of energy that a battery can store per unit of weight. It indicates the battery energy density and represents how much energy it can deliver relative to its weight or volume. Higher specific energy means that a battery can store more energy in a given size or weight, allowing for longer operating times in devices.
- *High specific power:* up to several kW/kg for power cells. Specific power refers to the rate at which a battery can deliver energy per unit of weight. It represents the battery's power density and indicates how quickly it can discharge energy. Higher specific power means that a battery can deliver energy more rapidly, enabling it to handle high-power applications or fast charging requirements.
- *High specific capacity:* 3.86 Ah/g. Battery capacity is an essential parameter as it determines how long a battery can power a device before needing recharging. It is influenced by factors such as battery chemistry, size, and design.

- *Self-discharge:* very low (a few percents per month). The self-discharge of a battery refers to the gradual loss of charge or capacity over time when the battery is not in use. It occurs due to various factors such as internal chemical reactions, leakage currents, and parasitic reactions within the battery.
- *Longer cycle life:* from 500 to 3000 cycles, depending on technologies. Lithium-ion batteries generally have a longer cycle life compared to other battery chemistries. They can endure a larger number of charge and discharge cycles before their capacity significantly degrades. This makes them a reliable choice for applications where long-term performance is desired.
- *No Memory Effect:* Lithium-ion batteries do not suffer from the memory effect, a phenomenon that affects some other rechargeable batteries. Memory effect refers to the reduction in a battery capacity when it is not fully discharged before recharging. With Lithium-ion batteries, users can recharge them at any point in the discharge cycle without impacting their overall capacity.

1.3.2 Cons

- *Sensitivity to High Temperatures:* Lithium-ion batteries are sensitive to high temperatures. Exposure to elevated temperatures can accelerate the aging process and lead to capacity loss or even thermal runaway, which can result in safety hazards. Proper thermal management and operating within recommended temperature ranges are essential to mitigate these risks.
- *Rapid Charging:* Lithium-ion batteries can be charged at a faster rate compared to some other battery chemistries, which increases the risk of lithium plating at the negative electrode.
- *Safety Concerns:* While Lithium-ion batteries are generally considered safe, certain factors can increase the risk of safety incidents. Mishandling, physical damage, manufacturing defects, or using damaged or counterfeit batteries can lead to thermal runaways, fires, or explosions. Proper care, usage, and adherence to safety guidelines are crucial to ensure safe operation.

With a foundational overview of Lithium-ion batteries in place, our exploration now takes us towards a specific type within this category: LiFePO4 batteries. These batteries will form the core focus of our study.

1.4 LiFePO4 batteries

Lithium iron phosphate (LiFePO4) batteries, commonly referred as LFP batteries, offer numerous advantages over other types of Lithium-ion batteries. As a result, they are rapidly gaining popularity as a prominent alternative for various electric devices across industries.

In this work, we will focus on this type of batteries, intending to contribute valuable insights that can further enhance the utilization of the latter in the industry.

1.4.1 Main advantages

- *Environmental Friendliness:* LFP batteries are considered more environmentally friendly compared to some other Lithium-ion chemistries because they don't contain toxic metals such as cobalt or nickel. They have lower environmental impact and are easier to recycle.
- *Cycle Life:* LFP batteries have a long cycle life, allowing them to endure a large number of charge and discharge cycles without significant capacity degradation. They can typically handle thousands of cycles, making them durable and suitable for applications that require frequent cycling, such as electric vehicles (EVs) and energy storage systems.
- *Low cost:* LFP batteries use iron and phosphate which are much more abundant compared to other types of metals.
- *Consistent discharge voltage:* Less power loss occurs when discharging compared to other types of batteries.

1.4.2 Main disadvantages

- *Low energy density:* requires then more protection.
- *Open circuit voltage (OCV):* The main drawback of LFP batteries is that the open circuit voltage, which is a nonlinear function of the SOC, is flat over a long interval as shown in Figure 1.3, obtained from SAFT Matlab model, where V_{oc} is the OCV.

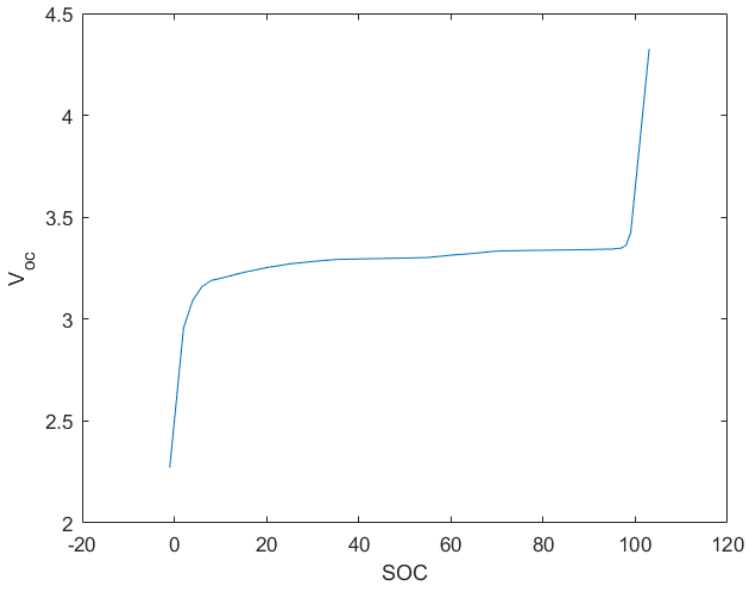

Figure 1.3: OCV (volts) versus SOC (%) for LiFePO4 batteries.

This OCV behavior poses a significant challenge for accurate SOC estimation, as very similar values for V_{oc} are obtained for SOC in $[7\%, 98\%]$, which limits the ability of the Battery Management System (BMS) to preserve the battery life. In the next section, we will introduce the latter.

1.5 Battery Management System

A Battery Management System (BMS) is an electronic system that monitors and manages the charging, discharging, and overall performance of a rechargeable battery, such as those used in electric vehicles, renewable energy storage systems, and portable electronics.
Its primary function is to ensure the safe and efficient operation of the battery, prolong its lifespan, and optimize its performance during various usage scenarios.

The SOC is a fundamental parameter for the proper functioning of the BMS.

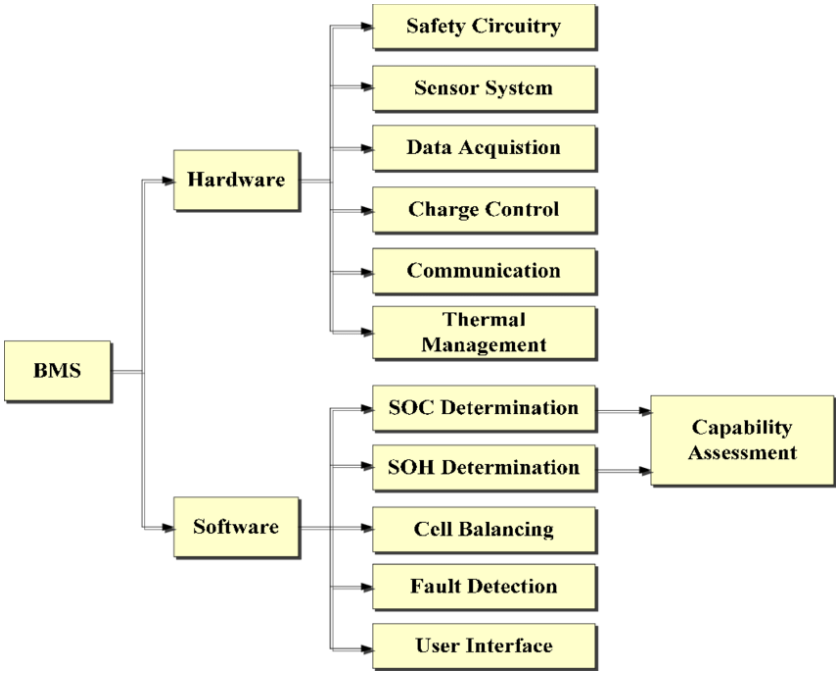

Figure 1.4: The BMS functions, taken from [33].

1.6 Conclusion

In this chapter, we gained an understanding of Lithium-ion batteries, as it introduced us to their components and operating principles. Furthermore, we explored their advantages and drawbacks, with a specific focus on LFP batteries, which are central to our research. Armed with this knowledge of the technology, we are now prepared to get into their modeling in the upcoming chapter.

Lithium-ion battery modelling

Chapter 2

Lithium-ion battery modelling

In this chapter, we will first present the two main types of models used in literature to describe lithium-ion battery dynamics and discuss their pros and cons. Our focus then shifts to an Equivalent Circuit Model (ECM) suitable for the battery management system, which we carefully model. Finally, we will simulate this model to better understand the behavior of our system's internal states before getting into the estimation problem.

2.1 Types of Lithium-ion battery models

Several types of models have been developed to describe Lithium-ion dynamics in the literature. They can be divided into two main categories. Electrochemical models [9, 5], on the one hand, describe the internal phenomena of the battery by relying on physical and chemical laws. These models give a faithful description of the battery dynamics but are generally more challenging to exploit for management purposes as they need to be of high enough dimension to generate accurate data and they rely on parameters, which may not be easy to know. On the other hand, the second popular category is made of Equivalent Circuit Models (ECM) [12, 34], which consist in describing the main battery variables, like the SOC and the output voltage, using simple electrical circuits. They basically consist of coupled voltage sources, resistors and capacitors in series and parallel. Their design is then much simpler to deal with but they usually require a non-trivial parameterization to fit experimental data.

2.1.1 Electrochemical models

In Lithium-ion batteries, many complex phenomena are involved such as mass transport, migrations of ions, red-ox reactions and side reactions. Electrochemical models tend to describe these internal key behaviors of battery cells.

To create a current flow in the external circuit of the battery, it is necessary that a transfer of lithium takes place between the two electrodes. Depending on the electrode considered and the direction of the current, two types of phenomena occur:

— *Insertion:* lithium ions in solution in the electrolyte at the solid-electrolyte interphase

are reduced in the electrode. This takes place during charge at the negative electrode and during discharge at the positive electrode;
— *Deinsertion:* lithium atoms at the solid-electrolyte interphase ionize to release electrons. This occurs during charge at the positive electrode and discharge to the negative electrode [2].

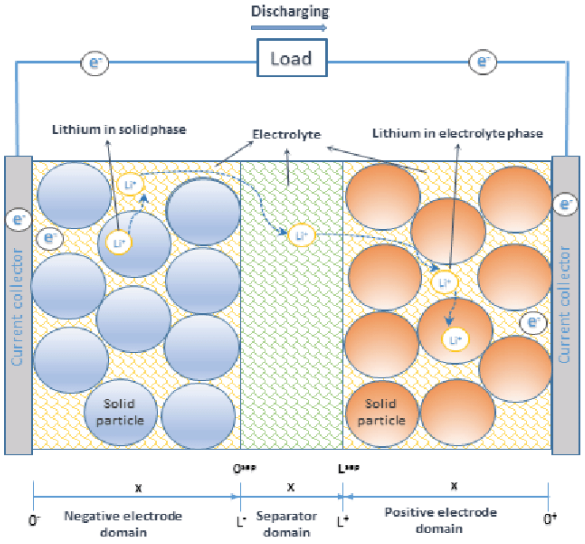

Figure 2.1: Electrochemical scheme of a lithium-ion battery, taken from [24].

The above phenomena are well captured by partial differential equations [5]. The P2D model, i.e., the Pseudo-Two-Dimensional model, as the origin of the electrochemical model, was proposed by M. Doyle, T. Fuller, and J. Newman [9, 25]. This model described the working processes inside the Lithium-ion battery in detail with formulas based on the porous electrode theory and the concentrated solution. In the Pseudo Two-Dimensional (P2D) model, the battery behavior is approximated as if it were occurring in a 2D domain, which simplifies the computational complexity while still capturing important electrochemical and transport phenomena. Subsequently, it underwent rigorous review and improvement by the authors e.g., [17, 26]. These equations may then be used to obtain finite-dimensional models. The latter is more convenient for implementation but still usually requires high dimensions to generate accurate data. They are hardly suitable for the BMS design [7].

2.1.2 Equivalent Circuit Models

Lithium-ion batteries are often modeled using ECM since they are easy to manipulate, more intuitive and easily integrated into the BMS.

Various battery equivalent circuit models have been proposed to reflect dynamic characteristics of the battery as a result of the trade-off between modelling accuracy and complexity [12, 23], such as the first-order RC [34, 8, 16], second-order RC [6, 10] and N-order RC models [13, 14, 20]. The parameters in these models need to be adjusted, either using data-driven methods or a bank of Kalman filters [3]. They are related to

several physical quantities:

- the terminal voltage;
- the current;
- the state of charge (SOC);
- the temperature.

2.2 Selected model

In this study, based on experimental validations from SAFT, we have chosen to work with the first-order Equivalent Circuit Model shown in Figure 2.2.

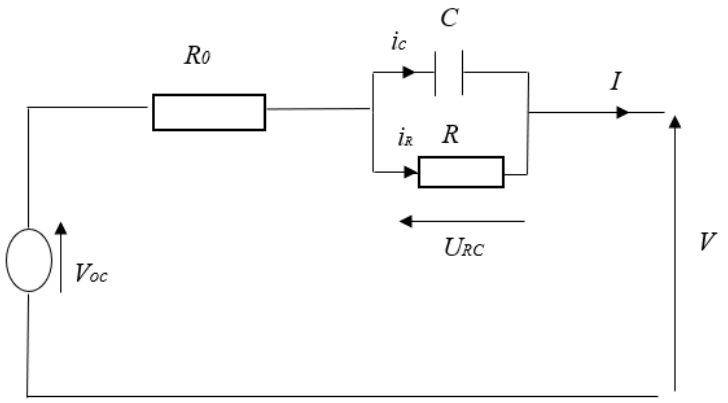

Figure 2.2: First order Equivalent Circuit Model.

- The series resistance R_0 stands for the ohmic voltage drop that occurs in electrode and electrolyte.
- The RC parallel circuit represents behavior during transients.
- U_{RC} is the voltage across the RC network.
- V_{oc} is the open circuit voltage.
- V is the battery terminal voltage.
- I is the battery current.

We derive from Figure 2.2 the next equalities

$$V = V_{oc}(SOC) - U_{RC} - R_0 I \tag{2.1}$$

$$I = i_C + i_R \tag{2.2}$$

$$U_{RC} = R i_R \tag{2.3}$$

Since

$$i_c = C\frac{dU_{RC}}{dt}, \tag{2.4}$$

then

$$\frac{dU_{RC}}{dt} = \dot{U}_{RC} = \frac{(I - i_R)}{C} \tag{2.5}$$

From (2.3) and (2.5), we obtain

$$\dot{U}_{RC} = -\frac{U_{RC}}{RC} + \frac{I}{C} \tag{2.6}$$

On the other hand, the state of charge is defined as the ratio of the remaining capacity to the nominal capacity of the battery

$$SOC(t) = 100\Big(SOC(0) + \int_0^t \frac{I(z)}{Q} dz \ \Big) \qquad \forall t \geq 0 \tag{2.7}$$

where $Q = 3600 Q_n$ with Q_n the nominal capacity of the battery in Ampere-hour (AH) when time is expressed in seconds. We derive from (2.3) that

$$\dot{SOC} = 100\frac{I}{Q} \tag{2.8}$$

Our goal is to have a state space model of the following form

$$\begin{cases} \dot{x} = Ax + Bu \\ \\ y = h(x) + Du \end{cases} \tag{2.9}$$

Given (2.1), (2.6) and (2.8) we obtain

$$\begin{cases} \dot{SOC} = 100\dfrac{I}{Q} \\ \\ \dot{U}_{RC} = -\dfrac{U_{RC}}{\tau} + \dfrac{I}{C} \\ \\ y = V = V_{oc}(SOC) - U_{RC} - R_0 I \end{cases} \tag{2.10}$$

where the state vector is $x = \begin{pmatrix} SOC \\ U_{RC} \end{pmatrix}$, $h(x) = V = V_{oc}(SOC) - U_{RC} - R_0 I$, $D = -R_0$, $u = I$, and the dynamics matrix and the input matrix are respectively

$$A = \begin{bmatrix} 0 & 0 \\ 0 & \frac{-1}{\tau} \end{bmatrix}, \; B = \begin{bmatrix} \frac{100}{Q} \\ \frac{1}{C} \end{bmatrix}$$

where $\tau = RC$, and V_{oc} is a nonlinear function. In this thesis, as mentioned in Chapter 1, we focus on LFP cells, which are characterized by an almost flat part for a large interval, as illustrated in Figure 2.3 obtained from SAFT Matlab model by experiments with the real parameters.

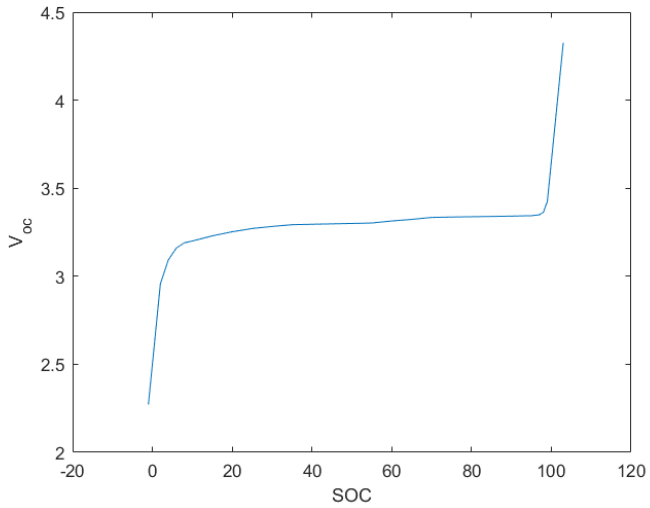

Figure 2.3: V_{oc} versus SOC curve for LiFePO4 batteries.

2.3 Numerical simulations

We have used Matlab-Simulink to simulate model (2.10) with the parameters values given in Table 2.1.

Parameters	R_0	R	C	τ	Q_n	$U_{RC}(0)$	$SOC(0)$
Values	0.0005	0.002	3500	7	189	0	1
Units	Ω	Ω	F	s	AH	V	%

Table 2.1: Parameters values and initial conditions

The current profile and real terminal voltage figures are shown below, induced from SAFT Matlab model. The resulting SOC, U_{RC} and y are respectively given in Figures 2.4, 2.5 and 2.6.

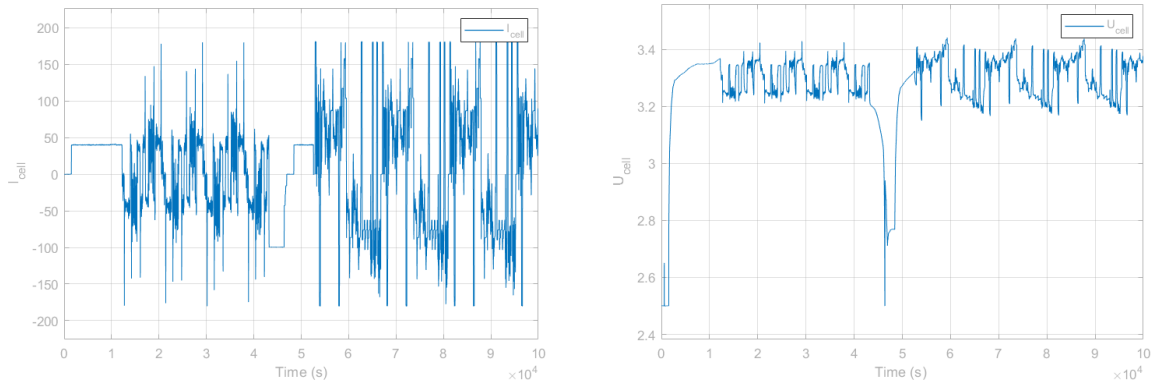

(a) Battery current I_{cell} (amperes). (b) Real terminal voltage U_{cell} (volts).

Figure 2.4: (a) The current profile and (b) real terminal voltage figures drawn from SAFT Matlab model.

We are considering successive charge and discharge cycles as shown in the SOC curve in Figure 2.5.

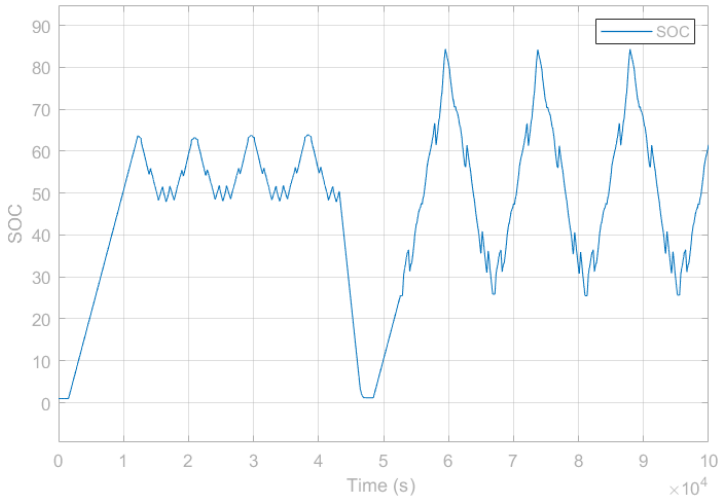

Figure 2.5: Model SOC in %.

The convention used for the current sign is positive in charge and negative in discharge.

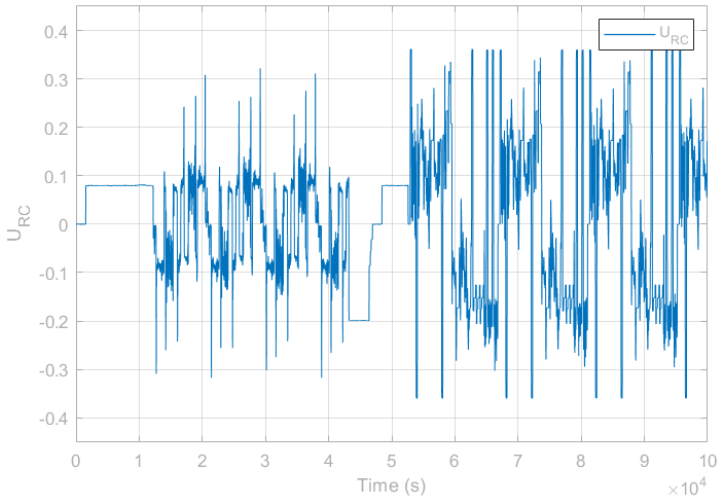

Figure 2.6: Model U_{RC}.

The value of U_{RC} varies nearly in $[-0.36\ 0.36]$ V as shown in Figure 2.6.

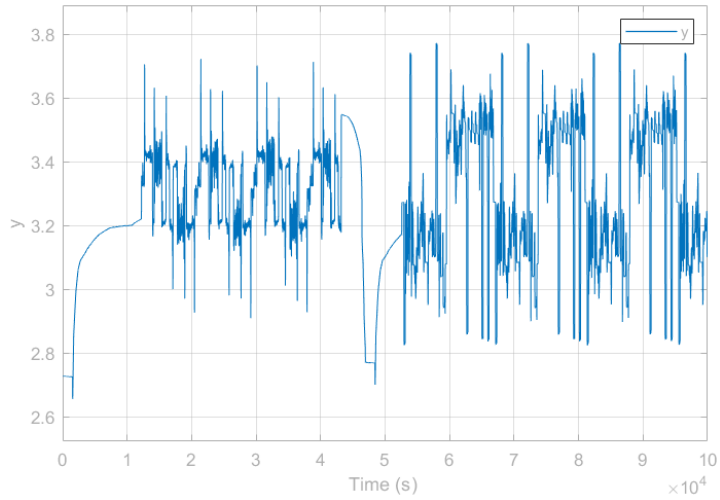

Figure 2.7: Model terminal voltage y.

The model terminal voltage varies in $[2.65, 3.77]$ V. Let us note that it is slightly different from the real terminal voltage that varies in $[2.5, 3.65]$ V as shown in Figure 2.7, due to the use of constant parameters without considering their dependencies.

2.4 Conclusion

In this chapter, we have presented the main types of models used in literature to describe lithium-ion battery dynamics. We have seen their pros and cons and expressed the selected model for this work, based on experimental validations done by SAFT.

Now that we are familiar with the battery cell model, we will focus in the next chapter on the main challenge of this thesis: observer design for the online estimation of the state of charge.

Observer design

Chapter 3

Observer design

As mentioned in Chapters 1 and 2, obtaining an accurate estimation of the SOC holds significant importance for the BMS, as it plays a crucial role in preventing overcharge or discharge, ultimately extending the battery lifespan. However, due to its dependence on internal chemical parameters within the battery cell, the SOC cannot be directly measured by a sensor. In this chapter, our objective is to develop a state observer that is both suitable and precise for SOC estimation, specifically tailored for LFP batteries.

Initially, we will assume that the model parameters are known and constant. By establishing this foundation, we can focus on creating an effective SOC estimation algorithm, laying the groundwork for further advancements in our pursuit of accurate battery monitoring and management. The case of varying parameters is discussed in Chapter 4.

3.1 State of the art

A variety of estimation techniques are available for Lithium-ion models in the literature in order to estimate the SOC precisely and accurately. They can be classified into four main categories [4] which are summarized below

- Direct measurement methods are employed to estimate the SOC by exploiting the battery physical properties. One such method is the Open Circuit Voltage approach, which relies on the stable battery electromotive force in the open circuit state and its relationship with SOC to estimate the SOC value. However, as highlighted in Chapter 2, the OCV function for LFP batteries exhibits a nearly flat behavior over a wide range of SOC values. This inherent characteristic poses a significant issue, rendering accurate SOC estimation through the OCV curve unfeasible [22].

- Bookkeeping estimation methods utilize the battery charge and discharge currents as inputs to estimate the state of charge (SOC). One prominent method in this category is the Coulomb counting method, which involves integrating the battery charging and discharging currents over time to calculate the SOC. However, it is essential to note that the accuracy of these bookkeeping methods can be significantly influenced by two critical factors: initial SOC error and measurement noise [21].

- Artificial intelligence-based methods offer promising data-oriented approaches for

accurately estimating the SOC even without precise initial information. However, it is crucial to acknowledge that these methods demand significant computational time and storage capacity as they need a large amount of data to train [30].

- Lastly, the model-based methods where the battery parameters and SOC are estimated using adaptive filters and observers such as variants of Kalman filter, sliding mode observers, etc. These methods have the advantage of being insensitive to initial SOC, which seems to be a better tradeoff between accuracy and computing efficiency [28, 19].

In this thesis, our focus will be on the last category as they are of a closed-loop nature and thus robust in general.

3.2 Observability analysis

To ease the observability analysis, we approximate the OCV by a piecewise linear function. This allows to analyse the observability of the original model (2.10) in the different regions separately by exploiting linear systems theoretic tools. The piecewise linear approximation leads to the following linear system

$$\begin{cases} \dot{SOC} = 100\dfrac{I}{Q} \\ \dot{U}_{RC} = -\dfrac{U_{RC}}{\tau} + \dfrac{1}{C}I \\ y = V = V_{oc} - U_{RC} - R_0 I = \alpha(SOC)SOC + \beta(SOC) - U_{RC} - R_0 I \end{cases} \tag{3.1}$$

where

$$\alpha(SOC) = \begin{cases} \alpha_1 > 0 & \text{if} \quad SOC \in [0\%, 7\%] \\ \alpha_2 \simeq 0 & \text{if} \quad SOC \in [7\%, 98\%] \\ \alpha_3 > 0 & \text{if} \quad SOC \in [98\%, 100\%] \end{cases}$$

and

$$\beta(SOC) = \begin{cases} \beta_1 < 0 & \text{if} \quad SOC \in [0\%, 7\%] \\ \beta_2 > 0 & \text{if} \quad SOC \in [7\%, 98\%] \\ \beta_3 < 0 & \text{if} \quad SOC \in [98\%, 100\%] \end{cases}$$

System (3.1) can be written in the form

$$\begin{cases} \dot{x} = Ax + Bu \\ y = Cx + Du \end{cases} \tag{3.2}$$

where the dynamics matrix and the output matrix are respectively:

$$A = \begin{bmatrix} \frac{-1}{\tau} & 0 \\ 0 & 0 \end{bmatrix}, C = \begin{bmatrix} \alpha(SOC) & -1 \end{bmatrix}$$

The observability matrix is then given by $O = \begin{bmatrix} C \\ CA \end{bmatrix} = \begin{bmatrix} \alpha(SOC) & -1 \\ \frac{-1}{\tau}\alpha(SOC) & 0 \end{bmatrix}$
The observability matrix is full rank which means the system (3.1) is observable for $\alpha = \alpha_1$ or $\alpha = \alpha_3$. On the flat region, the observability is lost due to the nearly constant value of V_{oc}.

3.2.1 Nonlinear observability analysis

In order to test the observability of the non-linear system, we have the following observability matrix:

$$M = \frac{\partial}{\partial x} \begin{bmatrix} h(x) \\ L_f h(x) \end{bmatrix}$$

where $h(x) = V_{oc} - U_{RC} - R_0 I$, $L_f h(x) = \frac{\partial h}{\partial x} f(x)$, $f(x) = \begin{bmatrix} 0 \\ \frac{-U_{RC}}{\tau} \end{bmatrix}$.
We have

$$L_f h(x) = \begin{bmatrix} \frac{\partial h}{\partial SOC} & \frac{\partial h}{\partial U_{RC}} \end{bmatrix} \begin{bmatrix} f_1 \\ f_2 \end{bmatrix}$$

We obtain then

$$L_f h(x) = \begin{bmatrix} \frac{\partial V_{oc}(SOC)}{\partial SOC} & -1 \end{bmatrix} \begin{bmatrix} 0 \\ \frac{-U_{RC}}{\tau} \end{bmatrix} = \frac{U_{RC}}{\tau}$$

This gives us the following

$$M = \frac{\partial}{\partial x} \begin{bmatrix} V_{oc} - U_{RC} - R_0 I \\ \frac{U_{RC}}{\tau} \end{bmatrix} = \begin{bmatrix} \frac{\partial V_{oc}(SOC)}{\partial SOC} & -1 \\ 0 & \frac{1}{\tau} \end{bmatrix}$$

We deduce from the observability matrix that the system is weakly locally observable.

In the next section, we aim to explore the regions of observability in the OCV curve by employing sliding mode observers.

3.3 Sliding mode observer

The Sliding Mode Control (SMC) technique was first introduced by Utkin [31]. It is a robust control technique applicable to uncertain, perturbed nonlinear systems. It aims to construct a sliding surface in which the system has a desirable behavior, and then drive the model state to that surface and maintain it, as illustrated in Figure 3.1, i.e., once the system state reaches the sliding surface, it continuously slides along it, achieving robust and stable performance.

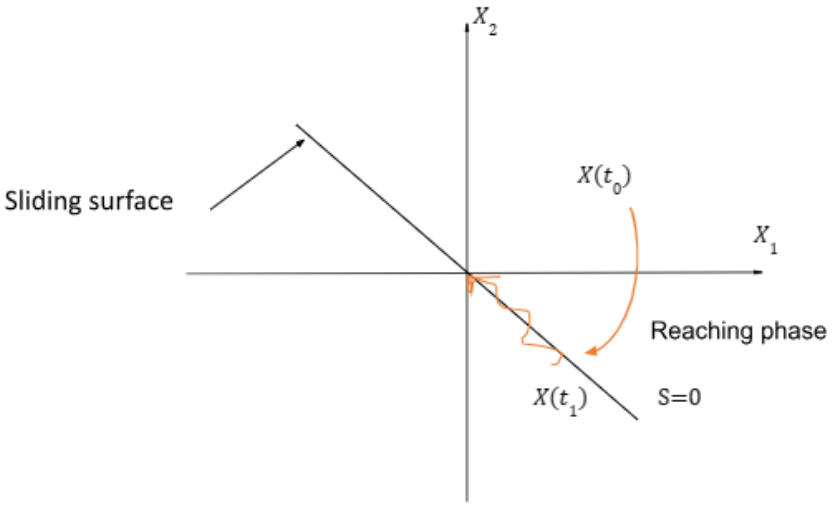

Figure 3.1: Sliding mode control general principle.

where X_1 and X_2 are the state variables and S is the sliding surface.

The sliding mode observer (SMO) is a copy of the plant model in addition to a feedback term that corrects the estimates by injecting back the discrepancy between its output and the output of the system via the discontinuous sign function [27]. In this case, the sliding surface is the error between the real output and its estimate $s = y - \hat{y}$.

For a state space model of the form of (2.9), the SMO takes the form below

$$\begin{cases} \dot{\hat{x}} = A\hat{x} + Bu + L\text{sign}(y - \hat{y}) \\ \\ \hat{y} = h(\hat{x}) + Du \end{cases} \tag{3.3}$$

where L is a 2x1 real matrix gain to be determined. The sign function is defined as

$$\forall e \in \mathbb{R} \qquad \text{sign}(e) = \begin{cases} 1 & \text{if} \quad e > 0 \\ 0 & \text{if} \quad e = 0 \\ -1 & \text{if} \quad e < 0 \end{cases}$$

The SMO layout is illustrated in Figure 3.2 below.

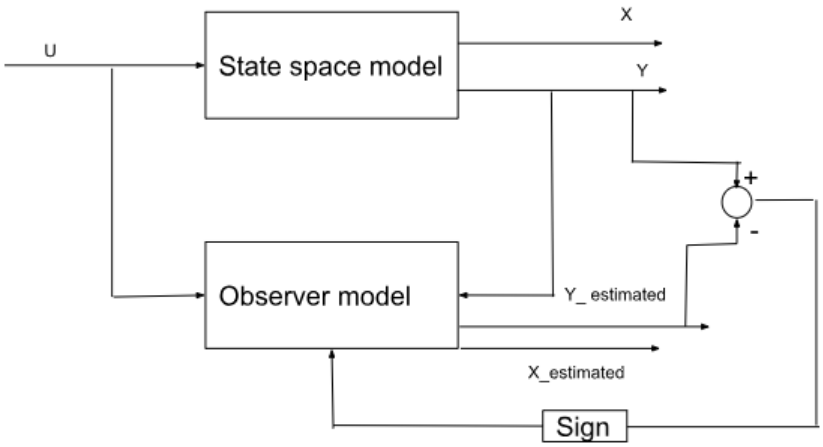

Figure 3.2: Sliding mode observer matlab scheme

Our idea behind the use of SMOs for the estimation of the SOC in this type of battery is to be able to exploit the areas where the OCV is not flat to ensure a finite-time convergence to the sliding surface, then try to maintain it there, and be also able to compensate the model uncertainties with the switching gains.

3.3.1 Conventional sliding mode observer

Our first attempt was to design a conventional first order SMO as presented next.

3.3.1.1 Change of coordinates

To design a SMO for system (2.10), we first need to change the coordinates. We define for this purpose the following state variable $v = \begin{pmatrix} \tilde{y} \\ SOC \end{pmatrix}$. $\tilde{y}$ is the output of the system defined as

$$\tilde{y} = \tilde{V} = V_{oc}(SOC) - U_{RC} = y + R_0 I \tag{3.4}$$

We derive $\tilde{y}$ from (3.4)

$$\dot{\tilde{y}} = -\dot{U}_{RC} + \frac{\partial V_{oc}(SOC)}{\partial SOC} S\dot{O}C = -\Big(-\frac{1}{\tau} U_{RC} + \frac{1}{C} I \Big) + \frac{\partial V_{oc}(SOC)}{\partial SOC} S\dot{O}C,$$

That brings us to the following equation of $\dot{\tilde{y}}$

$$\dot{\tilde{y}} = -\frac{1}{\tau}\tilde{y} + \frac{1}{\tau} V_{oc}(SOC) + I\Big(-\frac{1}{C} + \frac{100}{Q}\frac{\partial V_{oc}(SOC)}{\partial SOC}\Big) \tag{3.5}$$

We deduce from (2.8) and (3.5)

$$\begin{cases} \dot{\tilde{y}} = -\frac{1}{\tau}\tilde{y} + \frac{1}{\tau} V_{oc}(SOC) + I\Big(-\frac{1}{C} + \frac{100}{Q}\frac{\partial V_{oc}(SOC)}{\partial SOC}\Big) \\ \\ S\dot{O}C = 100\dfrac{I}{Q} \end{cases} \tag{3.6}$$

The output is $\tilde{y} = V_{oc}(SOC) - U_{RC}$. It is important to note that this change of coordinates is bijective. In fact, we can seamlessly switch between the previous model (see Chapter 2) and the current one without losing any information.

3.3.1.2 Observer equations

The SMO equations, which are a copy of the model's equations in addition to a correction term, are given below

$$\begin{cases} \dot{\hat{\tilde{y}}} = -\frac{1}{\tau}\hat{\tilde{y}} + \frac{1}{\tau} V_{oc}(\widehat{SOC}) + I\Big(-\frac{1}{C} + \frac{100}{Q}\frac{\partial V_{oc}(\widehat{SOC})}{\partial SOC}\Big) + L_1 \text{sign}(e_1) \\ \\ \dot{\widehat{SOC}} = 100\dfrac{I}{Q} + L_2 \text{sign}(e_1) \end{cases} \tag{3.7}$$

where $e_1 := \tilde{y} - \hat{\tilde{y}}$, $\hat{\tilde{y}}$ is the integral of $\dot{\hat{\tilde{y}}}$ defined in equation (3.7), and let $e_2 := SOC - \widehat{SOC}$, L_1 and L_2 are scalars to be determined.

3.3.1.3 Error dynamics

Subtracting (3.6) from (3.7) gives the dynamical reconstruction error system as

$$\begin{cases} \dot{e}_1 = -\frac{1}{\tau}(\tilde{y} - \hat{\tilde{y}}) + \frac{1}{\tau}(V_{oc}(SOC) - V_{oc}(\widehat{SOC})) + 100\dfrac{I}{Q}\Big(\dfrac{\partial V_{oc}(SOC)}{\partial SOC} - \dfrac{\partial V_{oc}(\widehat{SOC})}{\partial SOC}\Big) - L_1 \text{sign}(e_1) \\ \\ \dot{e}_2 = -L_2 \text{sign}(e_1) \end{cases} \tag{3.8}$$

Our objective is now to determine L_1 and L_2 so that the stability of the system (3.8) is guaranteed.

3.3.1.4 Lyapunov analysis

The stability of the previous error system has to be studied. This can be done by the Lyapunov analysis by exploiting the next theorem.

Theorem : [15]

Consider the autonomous system

$$\dot{x} = f(x) \tag{3.9}$$

Let $V : D \to R$ be a contnuously differentiable function defined in a domain $D \subset \mathbb{R}^n$ that contains the orgin. The derivative of V along the trajectories of (3.9), denoted by $\dot{V}(x)$, is given by

$$\dot{V}(x) = \sum_{i=1}^{n} \frac{\partial V}{\partial x_i}\dot{x}_i = \sum_{i=1}^{n} \frac{\partial V}{\partial x_i} f_i(x) = \Big[\frac{\partial V}{\partial x_1}, \frac{\partial V}{\partial x_2}, ..., \frac{\partial V}{\partial x_n}\Big] \begin{bmatrix} f_1(x) \\ f_2(x) \\ . \\ . \\ . \\ f_n(x) \end{bmatrix} = \frac{\partial V}{\partial x} f(x) \tag{3.10}$$

The derivative of V along the trajectories of a system is dependent on the system's equation. Hence, $\dot{V}(x)$ will be different for different systems. If $\psi(t; x)$ is the solution of (3.9) that starts at initial state x at time $t = 0$, then

$$\dot{V}(x) = \frac{d}{dt} V(\psi(t; x)) \quad \text{for} \quad t = 0 \tag{3.11}$$

Therefore, if $\dot{V}(x)$ is negative, V will decrease along the solution of (3.9). We are now ready to state Lyapunov's stability theorem.

Let $x = 0$ be an equilibrium point for (3.9) and $D \subset \mathbb{R}^n$ be a domain containing $x = 0$. Let $V : D \to R$ be a continuously differentiable function such that

$$V(0) = 0 \quad \text{and} \quad V(x) > 0 \quad \text{in} \quad D - \{0\} \tag{3.12}$$

$$\dot{V}(x) \leq 0 \quad \text{in} \quad D \tag{3.13}$$

then, $x = 0$ is stable. Moreover, if

$$\dot{V}(x) < 0 \quad \text{in} \quad D - \{0\} \tag{3.14}$$

then $x = 0$ is asymptotically stable.

Let us consider the following function: $V_1 = \frac{1}{2}e_1^2 \quad \forall e_1 \in \mathbb{R}$

$$\dot{V}_1 = e_1\Big[\frac{1}{\tau}(V_{oc}(SOC) - V_{oc}(\widehat{SOC})) + 100\frac{I}{Q}\Big(\frac{\partial V_{oc}(SOC)}{\partial SOC} - \frac{\partial V_{oc}(\widehat{SOC})}{\partial SOC}\Big)\Big] - e_1 L_1 \text{sign}(e_1) \tag{3.15}$$

Assume

$$\begin{cases} V_{oc}(SOC) - V_{oc}(\widehat{SOC}) \leq m_1 \\ \\ \dfrac{\partial V_{oc}(SOC)}{\partial SOC} - \dfrac{\partial V_{oc}(\widehat{SOC})}{\partial SOC} \leq m_2 \end{cases}$$

We have:

$$\dot{V}_1 \leq |e_1|(\frac{1}{\tau}m_1 + 100\frac{|I|}{Q}m_2) - L_1|e_1|$$

By taking

$$L_1 = \frac{m_1}{\tau} + 100\frac{|I|}{Q}m_2 + \epsilon_1, \qquad \epsilon_1 > 0$$

the following holds

$$\dot{V}_1 \leq -\epsilon_1|e_1| \tag{3.16}$$

Now, considering the Lyapunov function:

$$W_1 = \sqrt{V_1} \tag{3.17}$$

By deriving equation (3.17) we obtain $\dot{W}_1 = \dfrac{1}{2}\dfrac{\dot{V}_1}{\sqrt{V_1}} \leq \dfrac{-\epsilon_1|e_1|}{2\sqrt{V_1}}$

which gives

$$\dot{W}_1 \leq \frac{-\sqrt{2}\epsilon_1}{2} \quad \forall e_1 \neq 0 \tag{3.18}$$

then, $\dot{W}_1$ is a negative definite function.

Let us consider the following function: $V_2 = \frac{1}{2}e_2^2 \quad \forall e_2 \in \mathbb{R}$

$$\dot{V}_2 = e_2\big[- L_2\text{sign}(e_1)\big]$$

$$\dot{V}_2 = e_2\left[- \tfrac{L_2}{L_1}\left(\frac{1}{\tau}(V_{oc}(SOC) - V_{oc}(\widehat{SOC})) + 100\frac{I}{Q}\Big(\frac{\partial V_{oc}(SOC)}{\partial SOC} - \frac{\partial V_{oc}(\widehat{SOC})}{\partial SOC}\Big)\right)\right]$$

$$\dot{V}_2 = -\frac{L_2}{L_1}e_2\Delta V_{oc} - 100\frac{L_2}{L_1}\frac{I}{Q}e_2\Delta\partial V_{oc} \tag{3.19}$$

where $\Delta V_{oc} = V_{oc}(SOC) - V_{oc}(\widehat{SOC})$, $\Delta\partial V_{oc} = \dfrac{\partial V_{oc}(SOC)}{\partial SOC} - \dfrac{\partial V_{oc}(\widehat{SOC})}{\partial SOC}$

Since $V_{oc}(SOC)$ is a monotonous function, then $(SOC - S\hat{O}C)(V_{oc}(SOC) - V_{oc}(\widehat{SOC})) \geq 0$.

Therefore, one has

$$-\tfrac{L_2}{L_1}e_2\Delta V_{oc} \leq 0$$

Similarly, we have, assuming the monotony of the function $\frac{\partial V_{oc}(SOC)}{\partial SOC}$

$$(SOC - \widehat{SOC})\Big(\frac{\partial V_{oc}(SOC)}{\partial SOC} - \frac{\partial V_{oc}(\widehat{SOC})}{\partial SOC}\Big) \geq 0$$

$$\dot{V}_2 \leq -\frac{L_2}{L_1} e_2 \Delta V_{oc} + 100 \frac{L_2}{L_1} \frac{|I|}{Q} e_2 \Delta \partial V_{oc} \tag{3.20}$$

$$\dot{V}_2 \leq -\frac{L_2}{L_1} |e_2 \Delta V_{oc}| + 100 \frac{L_2}{L_1} \frac{|I|}{Q} |e_2 \Delta \partial V_{oc}| \tag{3.21}$$

By taking $\epsilon_2 = \frac{L_2}{L_1}\Big(|\Delta V_{oc}| + 100\frac{|I|}{Q}|\Delta \partial V_{oc}|\Big)$, we obtain the inequality:

$$\dot{V}_2 \leq -\epsilon_2 |e_2| \tag{3.22}$$

Now, considering the Lyapunov function:

$$W_2 = \sqrt{V_2} \tag{3.23}$$

Deriving equation (3.23) gives us $\dot{W}_2 = \frac{1}{2}\frac{\dot{V}_2}{\sqrt{V_2}} \leq \frac{-\epsilon_2 |e_2|}{2\sqrt{V_2}}$

That leads to this final inequality:

$$\dot{W}_2 \leq \frac{-\sqrt{2}\epsilon_2}{2} \quad \forall e_2 \neq 0 \tag{3.24}$$

then, $\dot{W}_2$ is a negative definite function.

3.3.1.5 Numerical simulations

We have used Matlab-Simulink to simulate model (3.7) with the parameters values and initial conditions given in Table 3.1.

Parameters	R_0	R	C	τ	Q_n	L_1	L_2	$\tilde{y}(0)$	$\hat{\tilde{y}}(0)$	$SOC(0)$	$\hat{SOC}(0)$
Values	0.002	0.002	3500	7	189	0.2	2	2.7	0	2	0
Units	Ω	Ω	F	s	AH			V	V	%	%

Table 3.1: Parameters values and initial conditions.

The current profile used as an input to the system, as presented in the previous chapter, is shown in Figure 3.3, drawn from SAFT Matlab model.

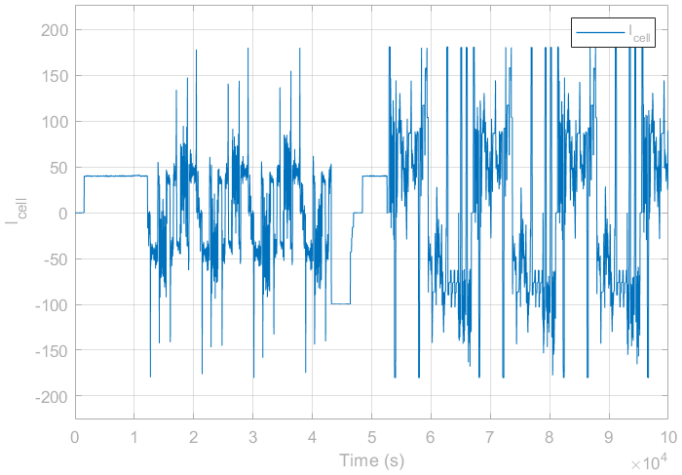

Figure 3.3: Battery current used as an input.

Figures 3.4 and 3.5 show respectively model and estimated $\tilde{y}$ and $\tilde{y}$ estimation error.

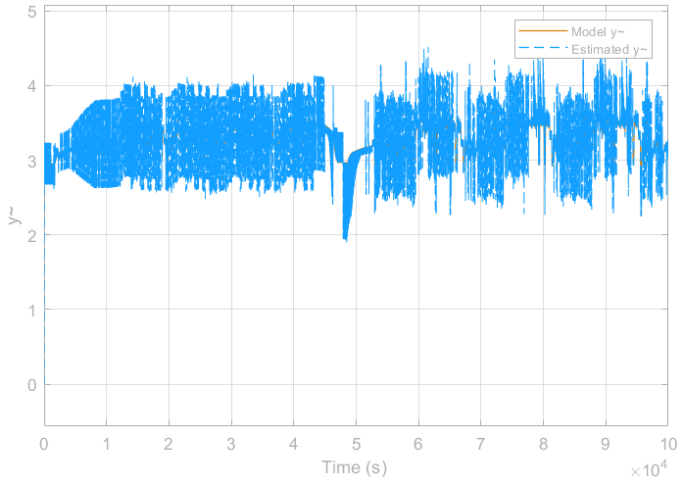

Figure 3.4: Model and estimated $\tilde{y}$ by the first observer.

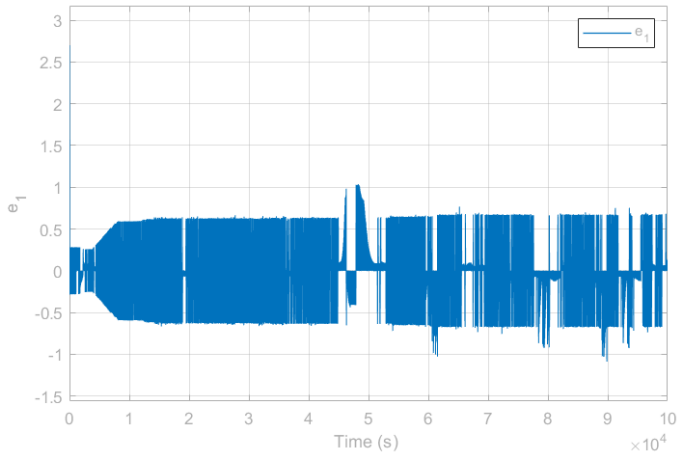

Figure 3.5: $\tilde{y}$ estimation error by the first observer.

Figures 3.6 and 3.7 show respectively model and estimated SOC and SOC estimation error.

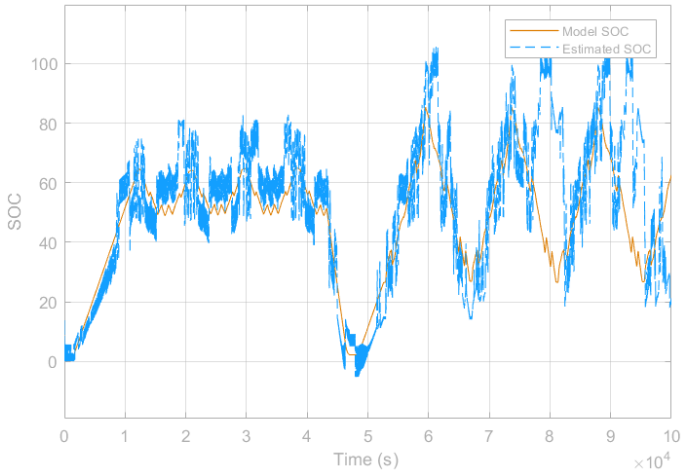

Figure 3.6: Model and estimated SOC by the first observer.

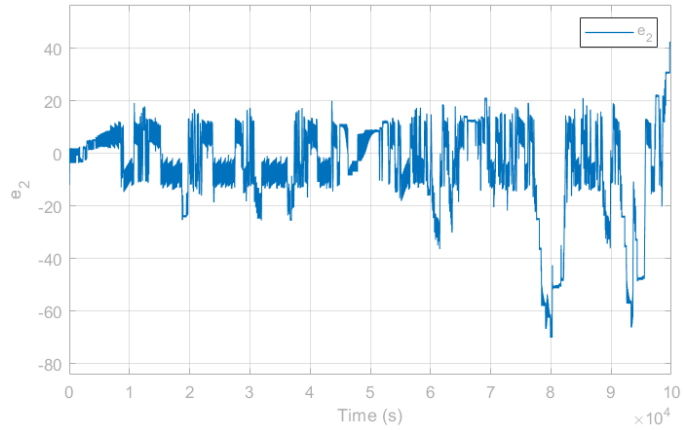

Figure 3.7: SOC estimation error by the first observer.

We have observed a significant amount of chattering, which is noticeably impeding the analysis of the results.
To smoothen the results and reduce the chattering effect, we replaced the sign function in the SMO equations with the following continuous function that can approximate it:

$$f(e) = \frac{e}{\sqrt{e^2 + \epsilon^2}} \tag{3.25}$$

With $\epsilon = 0.01$

We will present the results for different initial SOC and $\hat{SOC}$ conditions, within and outside the flat region, without and under measurement noise.

•Without measurement noise

We will first consider both SOC and $\widehat{SOC}$ initial conditions outside the flat region as shown in Table 3.2.

Variables	$SOC(0)$	$\widehat{SOC}(0)$	$\tilde{y}(0)$	$\hat{\tilde{y}}(0)$	L_1	L_2
Values	6	0	2.7	0	7	15
Units	%	%	V	V		

Table 3.2: Initial conditions and gain values.

Figures 3.8 and 3.9 show respectively model and estimated $\tilde{y}$, and its estimation error.

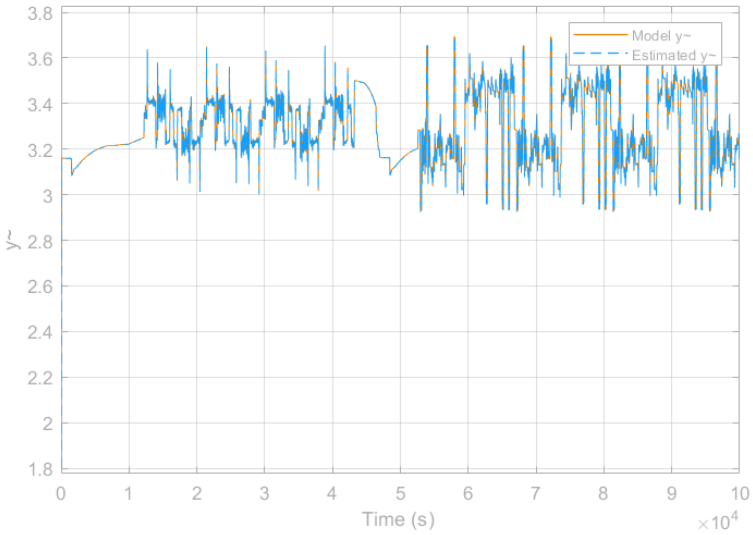

Figure 3.8: Model and estimated $\tilde{y}$ by the first observer, without measurement noise, assuming constant parameters and initial conditions outside the flat region.

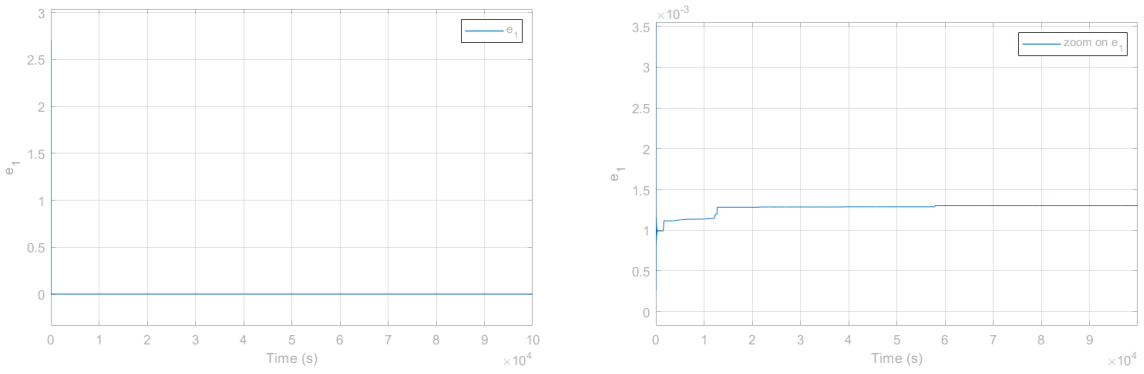

Figure 3.9: $\tilde{y}$ estimation error by the first observer, without measurement noise, assuming constant parameters and initial conditions outside the flat region.

We notice that the estimated $\tilde{y}$ smoothly tracks the real one and the error is around $0.001V$.

Figures 3.10 and 3.11 show respectively model and estimated SOC, and its estimation error.

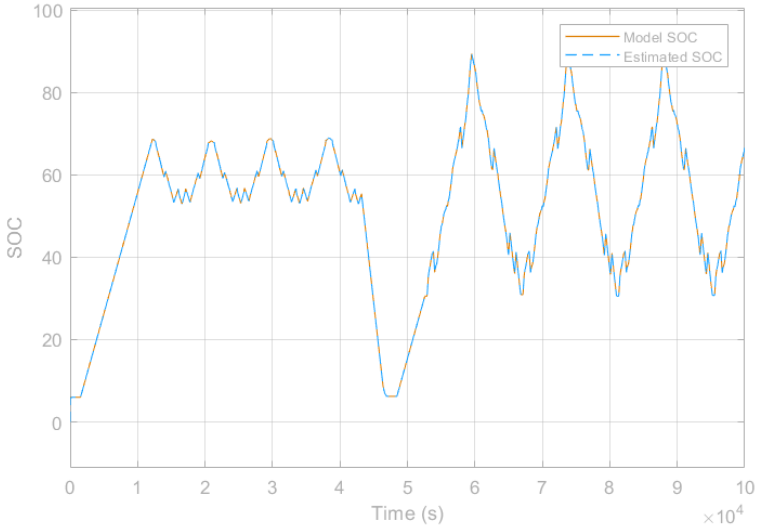

Figure 3.10: Model and estimated *SOC* by the first observer, without measurement noise, assuming constant parameters and initial conditions outside the flat region.

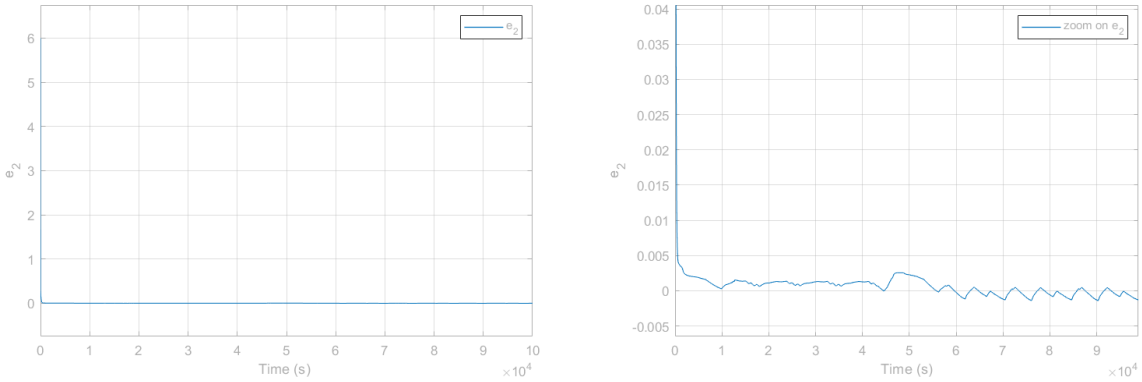

Figure 3.11: *SOC* estimation error by the first observer, without measurement noise, assuming constant parameters and initial conditions outside the flat region.

Let us note that the state of charge estimation error is less than 0.005 %, which proves the observer's good tracking using these initial conditions.

Next, we will consider both model and estimated *SOC* initial conditions within the flat region as shown in Table 3.3.

Variables	$SOC(0)$	$\widehat{SOC}(0)$	$\tilde{y}(0)$	$\hat{\tilde{y}}(0)$	L_1	L_2
Values	10	90	2.7	0	7	15
Units	%	%	V	V		

Table 3.3: Initial conditions and gain values.

Figures 3.12 and 3.13 show respectively model and estimated $\tilde{y}$, and its estimation error.

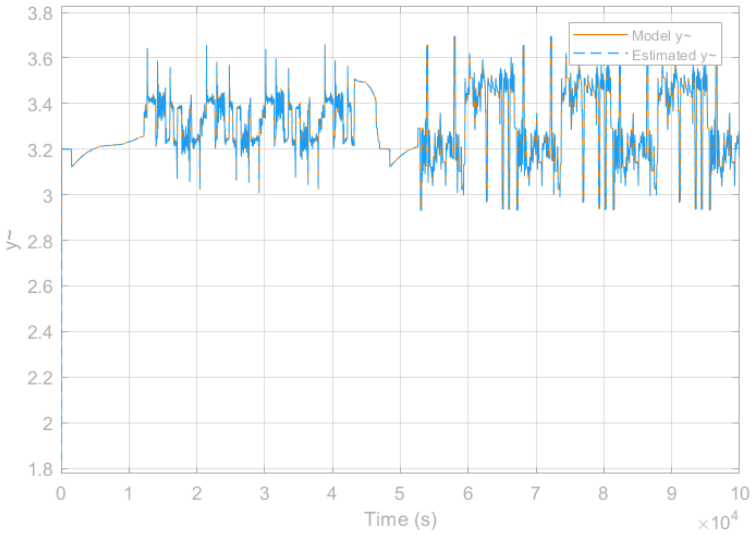

Figure 3.12: Model and estimated $\tilde{y}$ by the first observer, without measurement noise, assuming constant parameters and initial conditions within the flat region.

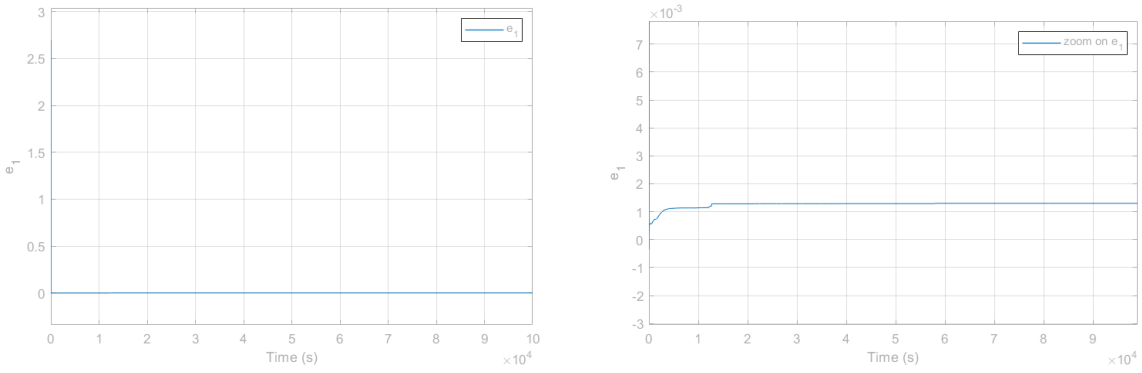

Figure 3.13: $\tilde{y}$ estimation error by the first observer, without measurement noise, assuming constant parameters and initial conditions within the flat region.

We can see that changing the initial conditions does not affect $\tilde{y}$ estimation. The error is still around $0.001V$.

Figures 3.14 and 3.15 show respectively model and estimated SOC and its estimation error.

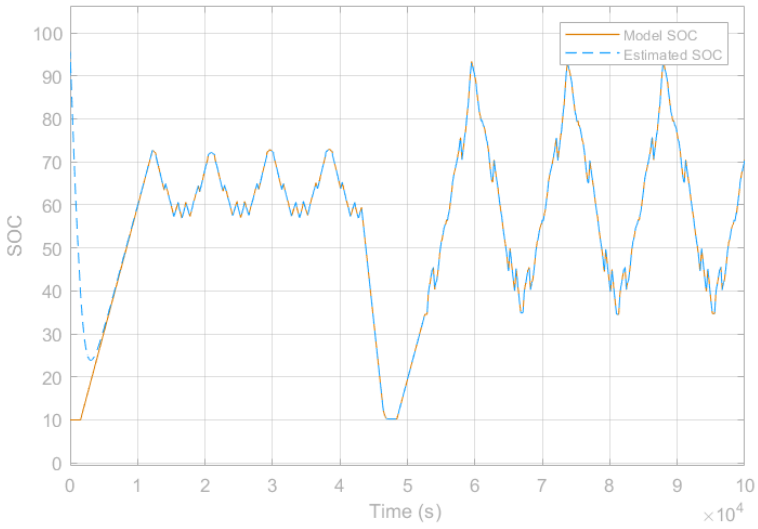

Figure 3.14: Model and estimated *SOC* by the first observer, without measurement noise, assuming constant parameters and initial conditions within the flat region.

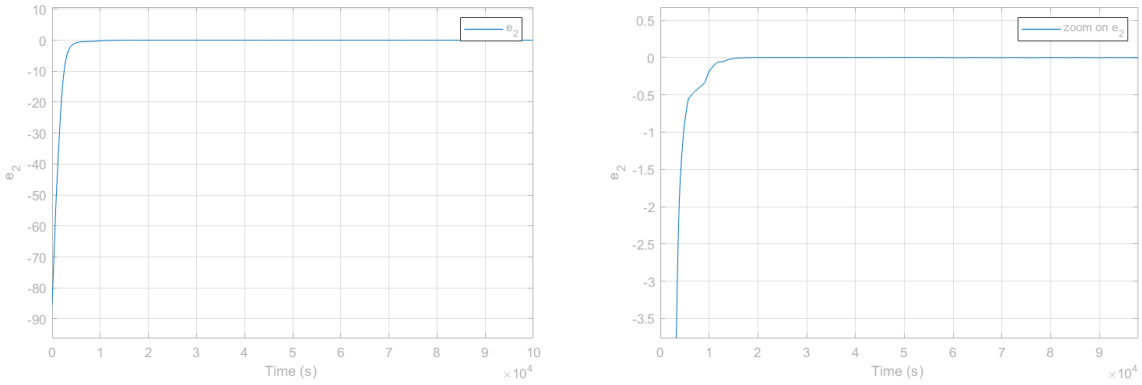

Figure 3.15: *SOC* estimation error by the first observer, without measurement noise, assuming constant parameters and initial conditions within the flat region.

Even by challenging the observer and considering both initial conditions within the flat region with an 80 % difference between them, the tracking is still good with an estimation error of less than 0.05 %.

Our observer demonstrates good performance in estimating the state of charge (SOC) under various initial conditions, whether the system is within or outside the flat region. The estimated SOC maintains an error margin of less than 0.05%. Additionally, the tracking of $\tilde{y}$ is flawless, with a low estimation error of 0.001 V, equivalent to 0.02%.

•Under measurement noise

To test the observer's robustness, we chose the following measurement noise to add to our model

$$n = 0.01sin(30t) \tag{3.26}$$

This choice has been based on experimentations. Its frequency $f = \frac{w}{2\pi} = 2.38Hz$.

We will test the observer for the same previous initial conditions to be able to do a comparison. Therefore, we will first consider both SOC and SOC initial conditions outside the flat region as shown in Table 3.2.

Figures 3.16 and 3.17 show respectively model and estimated SOC, and its estimation error.

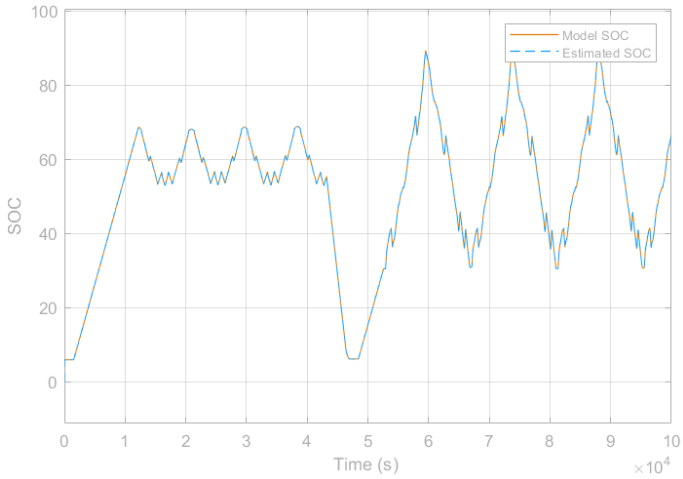

Figure 3.16: Model and estimated SOC by the first observer, under measurement noise, assuming constant parameters and initial conditions outside the flat region.

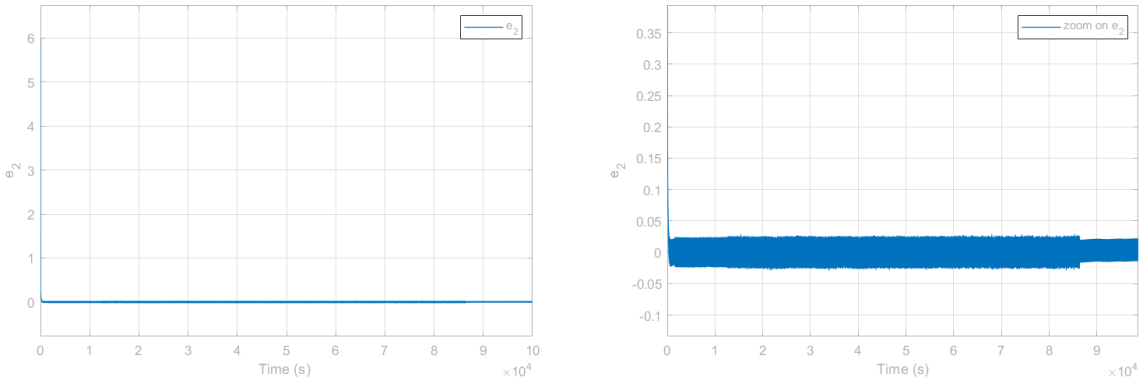

Figure 3.17: SOC estimation error by the first observer, under measurement noise, assuming constant parameters and initial conditions outside the flat region.

We can notice that the state of charge tracking is still good with an estimation error that slightly increases under noise to less than 0.05 %. We also notice an increase in chattering.

Figures 3.18 and 3.19 show respectively model and estimated $\tilde{y}$, and its estimation error.

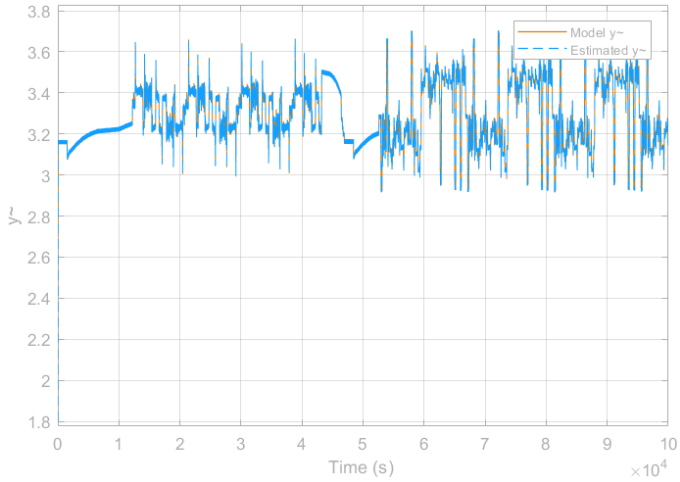

Figure 3.18: Model and estimated $\tilde{y}$ by the first observer, under measurement noise, assuming constant parameters and initial conditions outside the flat region.

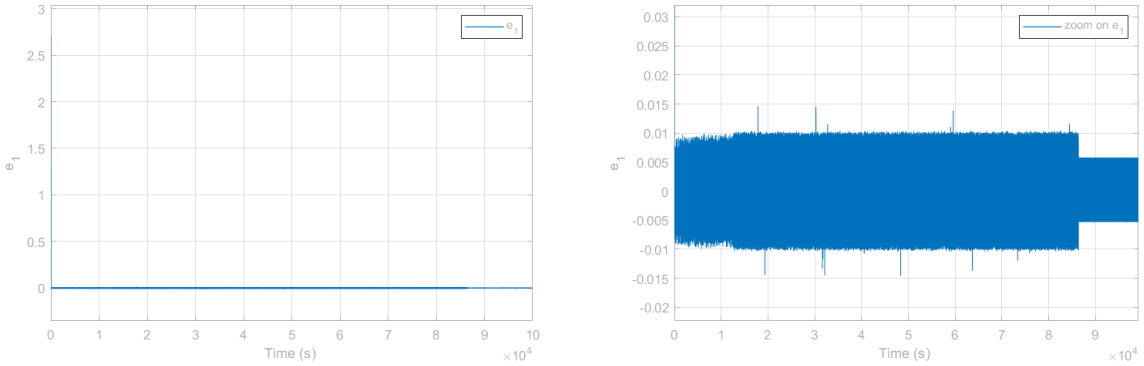

Figure 3.19: $\tilde{y}$ estimation error by the first observer, under measurement noise, assuming constant parameters and initial conditions outside the flat region.

Similarly for $\tilde{y}$, the estimation error increases to less than $0.015V$ which is still very acceptable.

Next, we will consider both model and estimated SOC initial conditions within the flat region as shown in Table 3.3.

Figures 3.20 and 3.21 show respectively model and estimated SOC, and its estimation error.

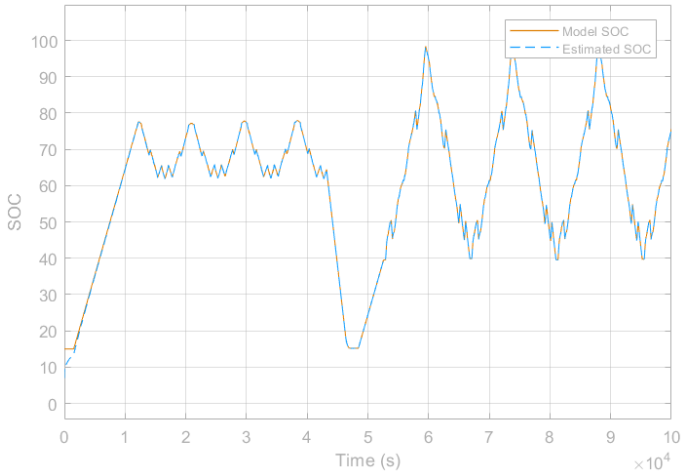

Figure 3.20: Model and estimated *SOC* by the first observer, under measurement noise, assuming constant parameters and initial conditions within the flat region.

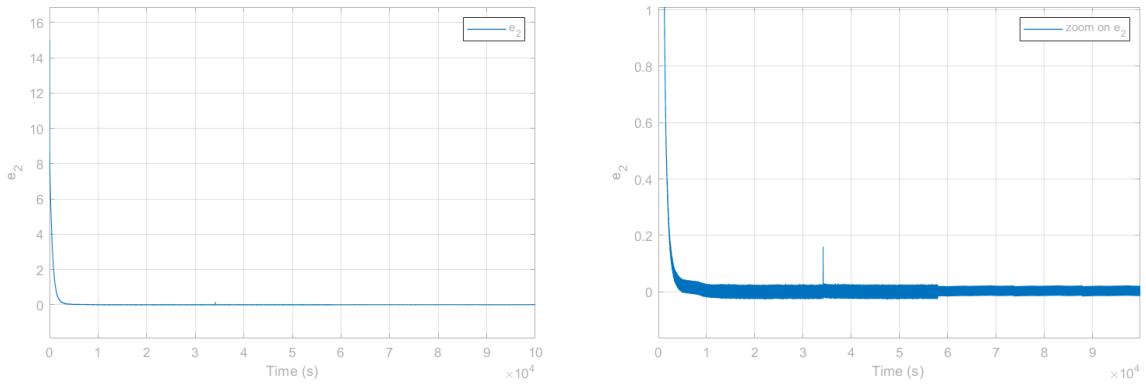

Figure 3.21: *SOC* estimation error by the first observer, under measurement noise, assuming constant parameters and initial conditions within the flat region.

As noticed in the first case, the state of charge estimation error is overall less than 0.2 % even while considering both initial conditions within the flat region and with a difference of 80 %.

Figures 3.22 and 3.23 show respectively model and estimated $\tilde{y}$, and its estimation error.

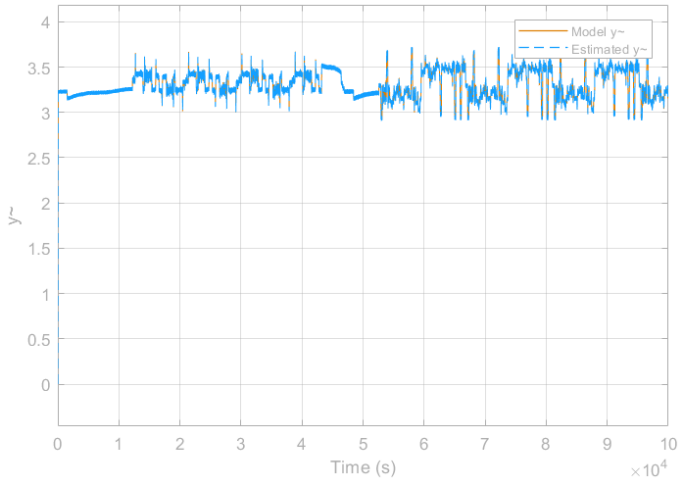

Figure 3.22: Model and estimated $\tilde{y}$ by the first observer, under measurement noise, assuming constant parameters and initial conditions within the flat region.

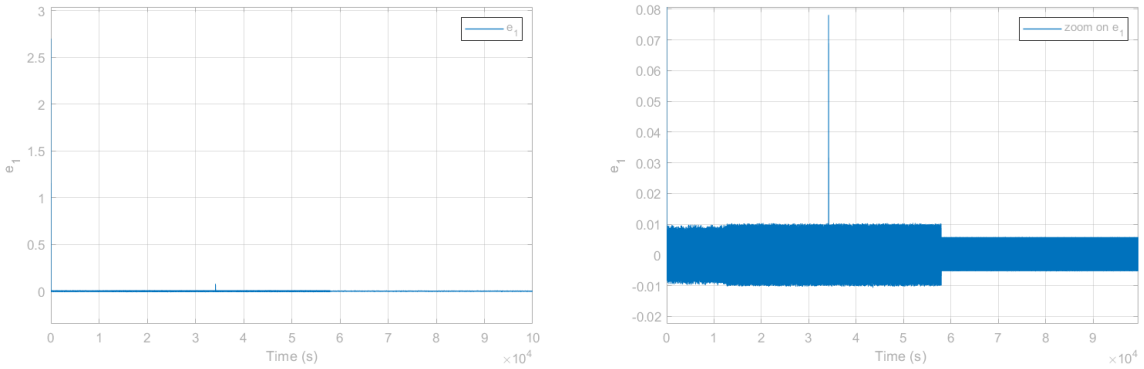

Figure 3.23: $\tilde{y}$ estimation error by the first observer, under measurement noise, assuming constant parameters and initial conditions within the flat region.

Similarly, we obtained a $\tilde{y}$ estimation error mostly stable at $0.01V$.

We have observed that even in the presence of measurement noise, the state of charge SOC and $\tilde{y}$ estimation errors remain minimal regardless of the initial conditions chosen, indicating a high level of robustness in the system. It is interesting to note that the good results we obtained are due to the fact that in the flat region, the open circuit voltage is not absolutely constant.

3.3.2 Alternative sliding mode observer

The idea of this observer is to force the open circuit voltage of the estimated SOC values $V_{oc}(\widehat{SOC})$ to be equal to the real estimation of V_{oc} i.e., $V_{oc}(\widehat{SOC}) = \hat{V}_{oc} = \hat{\tilde{y}} + \hat{U}_{RC}$. First, we will estimate U_{RC} and V_{oc}, only after, we construct the estimate of the state of charge.

3.3.2.1 Change of coordinates

Let us consider the following state variable: $i = \begin{pmatrix} \tilde{y} \\ U_{RC} \end{pmatrix}$

$$\tilde{y} = V_{oc}(SOC) - U_{RC} \tag{3.27}$$

Deriving $\tilde{y}$ from (3.27)

$$\dot{\tilde{y}} = -\big[-\frac{1}{\tau}U_{RC} + \frac{1}{C}I\big] + \frac{\partial V_{oc}(SOC)}{\partial SOC}S\dot{O}C \tag{3.28}$$

That brings us to the following equation for $\dot{\tilde{y}}$:

$$\dot{\tilde{y}} = \frac{1}{\tau}U_{RC} + I\Big(-\frac{1}{C} + \frac{100}{Q}\frac{\partial V_{oc}(SOC)}{\partial SOC}\Big) \tag{3.29}$$

We deduce from (2.6) and (3.29)

$$\begin{cases} \dot{\tilde{y}} = \frac{1}{\tau}U_{RC} + I\Big(-\frac{1}{C} + \frac{100}{Q}\frac{\partial V_{oc}(SOC)}{\partial SOC}\Big) \\ \\ \dot{U}_{RC} = -\frac{U_{RC}}{\tau} + \frac{I}{C} \end{cases} \tag{3.30}$$

The output is $\tilde{y} = V_{oc}(SOC) - U_{RC}$

By estimating $\tilde{y}$ and U_{RC}, we can have the estimate of V_{oc}.

Our goal in the next sections is to build the estimate of SOC so that $V_{oc}(\widehat{SOC}) = \hat{V}_{oc}$.

3.3.2.2 Observer equations

The SMO equations, which are a copy of the model's equations in addition to a correction term, are given below

$$\begin{cases} \dot{\hat{y}} = \frac{1}{\tau}\hat{U}_{RC} - \frac{1}{C}I + \frac{\partial V_{oc}(\widehat{SOC})}{\partial SOC}\Big(100\frac{I}{Q}\Big) + L_{11}e_1 + L_{12}\text{sign}(e_1) \\ \\ \dot{\hat{U}}_{RC} = -\frac{1}{\tau}\hat{U}_{RC} + \frac{1}{C}I + L_2e_1 \end{cases} \tag{3.31}$$

$\widehat{SOC}$ will be generated in the following; L_{11} and L_{12} are scalars to be designed; $e_1 := \tilde{y} - \hat{\tilde{y}}$, and let $e_2 := U_{RC} - \hat{U}_{RC}$.

3.3.2.3 The error dynamics

Subtracting equation (3.30) from equation (3.31) gives the dynamical reconstruction error system as

$$\begin{cases} \dot{e}_1 = \frac{1}{\tau}e_2 + \left[\frac{\partial V_{oc}(SOC)}{\partial SOC} - \frac{\partial V_{oc}(\widehat{SOC})}{\partial SOC}\right]\left(100\frac{I}{Q}\right) - L_{11}e_1 - L_{12}\text{sign}(e_1) \\ \\ \dot{e}_2 = -\frac{1}{\tau}e_2 - L_2 e_1 \end{cases} \tag{3.32}$$

3.3.2.4 Lyapunov analysis

The stability of the previous error system has to be studied. This can be done by the Lyapunov analysis.
Let the first Lyapunov function be $V_1 = \frac{1}{2}e_1^2 \quad \forall e_1 \in \mathbb{R}$ and the second function be $V_2 = \frac{1}{2}\lambda e_2^2$ $\forall e_2 \in \mathbb{R}$ with $\lambda > 0$ to be determined.

We derive V_1 as follows

$$\dot{V}_1 = \frac{1}{\tau}e_2 e_1 + \Delta\partial V_{oc}\left(100\frac{I}{Q}\right)e_1 - L_{11}e_1^2 - L_{12}|e_1| \tag{3.33}$$

Since one has $|\Delta\partial V_{oc}| \leq M$, we obtain

$$\dot{V}_1 \leq -L_{11}e_1^2 - L_{12}|e_1| + \frac{1}{\tau}e_1 e_2 + 100M\frac{|I|}{Q}|e_1| \tag{3.34}$$

By taking $L_{12} := 100M\frac{|I|}{Q} + \tilde{L}_{12}$ with $\tilde{L}_{12} > 0$, we obtain

$$\dot{V}_1 \leq -L_{11}e_1^2 - \tilde{L}_{12}|e_1| + \frac{1}{\tau}e_1 e_2 \tag{3.35}$$

On the other hand, we have

$$\dot{V}_2 = -\frac{\lambda}{\tau}e_2^2 - \lambda L_2 e_1 e_2 \tag{3.36}$$

Hence, for $V = V_1 + V_2$, we obtain

$$\dot{V} \leq \langle \begin{bmatrix} e_1 \\ e_2 \end{bmatrix} \begin{bmatrix} -L_{11} & \frac{1}{2\tau} - \frac{\lambda L_2}{2} \\ \frac{1}{2\tau} - \frac{\lambda L_2}{2} & \frac{-\lambda}{\tau} \end{bmatrix} \begin{bmatrix} e_1 \\ e_2 \end{bmatrix} \rangle - \tilde{L}_{12}|e_1| \tag{3.37}$$

By taking $M_1 = \begin{bmatrix} -L_{11} & \frac{1}{2\tau} - \frac{\lambda L_2}{2} \\ \frac{1}{2\tau} - \frac{\lambda L_2}{2} & \frac{-\lambda}{\tau} \end{bmatrix}$ We can always find L_{11} and L_2 so that $M_1 < 0$

For instance, by considering that $L_{11} > 0$ and $L_2 = \frac{1}{\tau\lambda}$, we obtain the following matrix: $M_1 = \begin{bmatrix} -L_{11} & 0 \\ 0 & \frac{-\lambda}{\tau} \end{bmatrix} < 0$

Hence, we obtain $\dot{V} \leq -\epsilon V$ with $\epsilon > 0$, we have then $e = 0$ Globally Exponentially Stable (GES).

- Finite time convergence of e_1

Since one has $\dot{V}_1 \leq -L_{11}e_1^2 - \tilde{L}_{12}|e_1| + \frac{1}{\tau}|e_1||e_2|$

And that, for any $c > 0$, $\exists T > 0$ so that $\forall t > T$, $|e_2| \leq c$, by taking $L_{12} > \frac{c}{\tau}$, we will have: $\dot{V}_1 \leq -\Big(L_{12} - \frac{c}{\tau}\Big)|e_1|$ from which we deduce that e_1 converges in finite time to 0.

3.3.2.5 Construction of the estimate of SOC

Now, let us consider $\dot{\widehat{SOC}}$ be free. We would like $\widehat{SOC}$ to be so that $\lim_{t\to+\infty} V_{oc}(\widehat{SOC}) - \hat{V}_{oc} \to 0$ with $\hat{V}_{oc} = \hat{\hat{y}} + \hat{U}_{RC}$
Let $e_3 = V_{oc}(\widehat{SOC}) - (\hat{\hat{y}} + \hat{U}_{RC})$

$$\dot{e_3} = \frac{\partial V_{oc}(\widehat{SOC})}{\partial \widehat{SOC}}\dot{\widehat{SOC}} - \left[\frac{\partial V_{oc}(\widehat{SOC})}{\partial \widehat{SOC}}\Big(100\frac{I}{Q}\Big) + L_{11}e_1 + L_{12}\text{sign}(e_1) + L_2e_1\right] \tag{3.38}$$

Let $\dot{\widehat{SOC}} = \Big(100\frac{I}{Q}\Big) + f$

$$\dot{e_3} = \frac{\partial V_{oc}(\widehat{SOC})}{\partial SOC}f - (L_{11} + L_2)e_1 - L_{12}\text{sign}(e_1) \tag{3.39}$$

Let $V_3 = \frac{1}{2}e_3^2$, we derive it and obtain:

$$\dot{V}_3 = e_3\frac{\partial V_{oc}(\widehat{SOC})}{\partial \widehat{SOC}}f - e_3\Big[(L_{11} + L_2)e_1 + L_{12}\text{sign}(e_1)\Big] \tag{3.40}$$

Let us consider $f = -\alpha_{13}\text{sign}(e_3) - \alpha_{23}e_3$

$$\dot{V}_3 = -\frac{\partial V_{oc}(\widehat{SOC})}{\partial \widehat{SOC}}\Big[\alpha_{13}|e_3| + \alpha_{23}e_3^2\Big] - e_3[(L_{11} + L_2)e_1 + L_{12}\text{sign}(e_1)] \tag{3.41}$$

Once e_1 has converged to 0 at time T, from equation (3.33), we will have

$$\Big[L_{12}\text{sign}(e_1)\Big]_{eq} = \frac{1}{\tau}e_2 + \Delta\partial V_{oc}\Big(100\frac{I}{Q}\Big) \tag{3.42}$$

Hence, for $t \geq T$

$$\dot{V}_3 = -\frac{\partial V_{oc}(\widehat{SOC})}{\partial \widehat{SOC}}\Big[\alpha_{13}|e_3| + \alpha_{23}e_3^2\Big] - e_3\Big[\frac{1}{\tau}e_2 + \Delta\partial V_{oc}\Big(100\frac{I}{Q}\Big)\Big] \tag{3.43}$$

By taking α_{13} and α_{23} so that $\frac{\partial V_{oc}(\widehat{SOC})}{\partial SOC}\Big[\alpha_{13}|e_3| + \alpha_{23}e_3^2\Big] >> 0$, we will be able to make e_3 converge to 0 in finite time.

The SMO algorithm is summarized below :

$$\begin{cases} \dot{\hat{\hat{y}}} = \frac{1}{\tau}\hat{U}_{RC} - \frac{1}{C}I + \frac{\partial V_{oc}(\widehat{SOC})}{\partial SOC}\Big(100\frac{I}{Q}\Big) + L_{11}e_1 + L_{12}\text{sign}(e_1) \\ \dot{\hat{U}}_{RC} = -\frac{1}{\tau}\hat{U}_{RC} + \frac{1}{C}I + L_2e_1 \\ \dot{\widehat{SOC}} = -\alpha_{13}\text{sign}(e_3) - \alpha_{23}e_3 + 100\frac{I}{Q} \end{cases} \tag{3.44}$$

where L_{11} and L_2 are so that $\exists\lambda > 0$ for which $\begin{bmatrix} -L_{11} & \frac{1}{2\tau} - \frac{\lambda L_2}{2} \\ \frac{1}{2\tau} - \frac{\lambda L_2}{2} & \frac{-\lambda}{\tau} \end{bmatrix} < 0$, $L_{12} > 0$ and α_{13},$\alpha_{23} > 0$

3.3.2.6 Numerical simulations

We have used Matlab-Simulink to simulate model (3.30) and SMO model (3.44) with the parameters values given in Table 3.4 and initial conditions given in Table 3.5. We have used the same current profile as for the conventional SMO, shown in Figure 3.2.

Parameters	R_0	R	C	τ	Q_n	L_{11}	L_{12}	L_2	α_{13}	α_{23}	λ
Values	0.002	0.002	3500	7	189	0.1	2	$\frac{1}{\tau\lambda}$	2	0.1	2
Units	Ω	Ω	F	s	AH						

Table 3.4: Parameters values.

Variables	$\tilde{y}(0)$	$U_{RC}(0)$	$SOC(0)$	$\hat{\tilde{y}}(0)$	$\hat{U}_{RC}(0)$	$\widehat{SOC}(0)$
Initial conditions	$V_{oc}(SOC(0))+$ $U_{RC}(0)$	0	1	$V_{oc}(\widehat{SOC}(0))+$ $\hat{U}_{RC}(0)$	0.2	0
Units	V	V	%	V	V	%

Table 3.5: Initial conditions.

Figures 3.24 and 3.25 show respectively model and estimated $\tilde{y}$, and its estimation error.

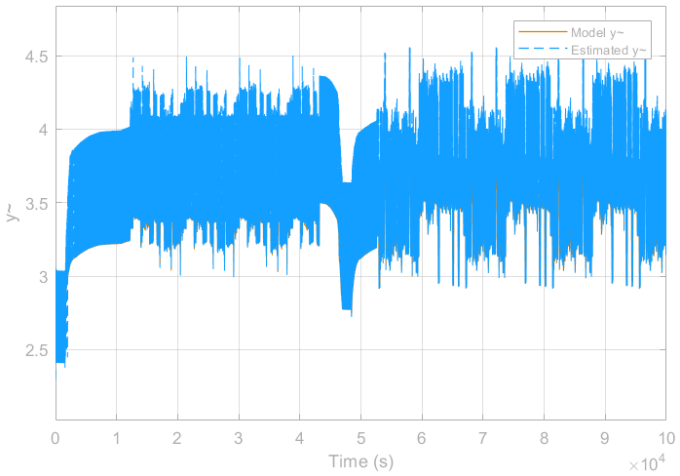

Figure 3.24: Model and estimated $\tilde{y}$ by the second observer.

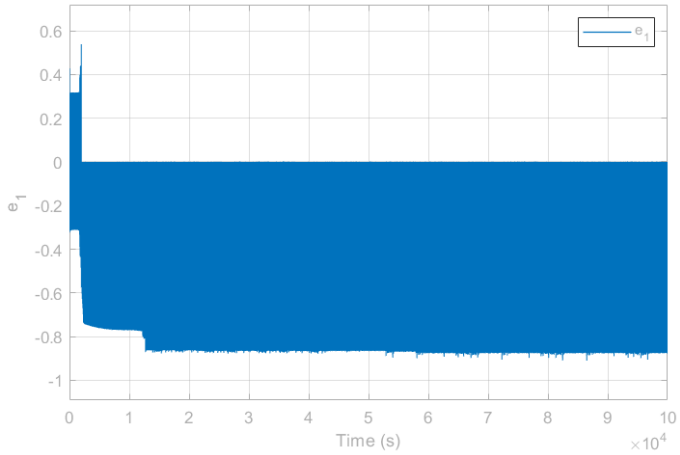

Figure 3.25: $\tilde{y}$ estimation error by the second observer.

Figures 3.26 and 3.27 show respectively model and estimated U_{RC}, and its estimation error.

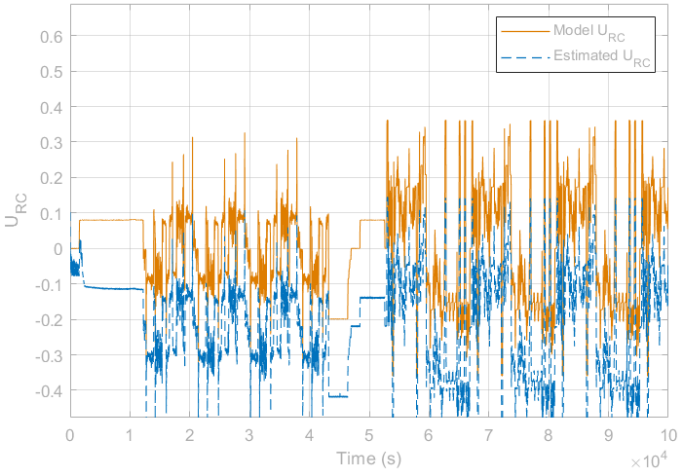

Figure 3.26: Model and estimated U_{RC} by the second observer.

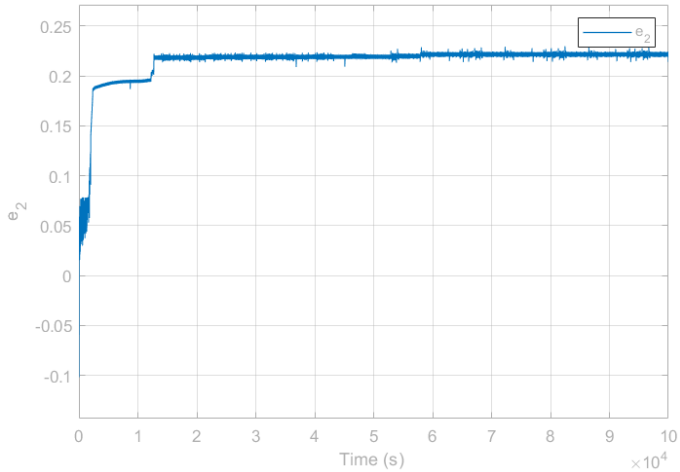

Figure 3.27: U_{RC} estimation error by the second observer.

Figures 3.28 and 3.29 show respectively model and estimated SOC, and its estimation error.

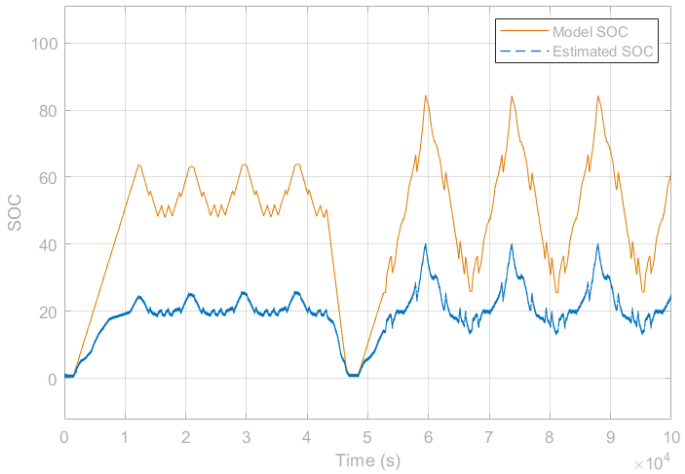

Figure 3.28: Model and Estimated SOC by the second observer.

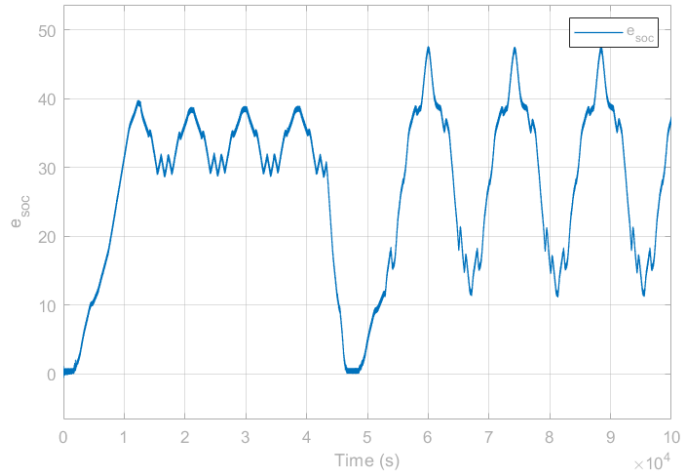

Figure 3.29: SOC estimation error by the second observer.

Similarly here, we have observed a significant amount of chattering, which is noticeably impeding the analysis of the results.
To smoothen the results and reduce the chattering effect, we replaced the sign function in the SMO equations with the following continuous function that can approximate it:

$$f(e) = \frac{e}{\sqrt{e^2 + \epsilon^2}} \tag{3.45}$$

With $\epsilon = 0.01$

We will present the results for different initial SOC and $\widehat{SOC}$ conditions, within and outside the flat region, without and under measurement noise, using the parameters values given in Table 3.6.

Parameters	R_0	R	C	τ	Q_n	L_{11}	L_{12}	L_2	α_{13}	α_{23}	λ

Values	0.002	0.002	3500	7	189	10	10	$\frac{1}{\tau\lambda}$	5	5	2
Units	Ω	Ω	F	s	AH						

Table 3.6: Parameters values.

•Without measurement noise

First, we will consider both model and estimated SOC initial conditions outside the flat region as shown in Table 3.7.

Variables	$\tilde{y}(0)$	$U_{RC}(0)$	$SOC(0)$	$\hat{\tilde{y}}(0)$	$\hat{U}_{RC}(0)$	$\widehat{SOC}(0)$
Initial conditions	$V_{oc}(SOC(0))+$ $U_{RC}(0)$	0.4	6	$V_{oc}(\widehat{SOC}(0))+$ $\hat{U}_{RC}(0)$	0	0
Units	V	V	%	V	V	%

Table 3.7: Initial conditions.

Figures 3.30 and 3.31 show respectively model and estimated SOC, and its estimation error.

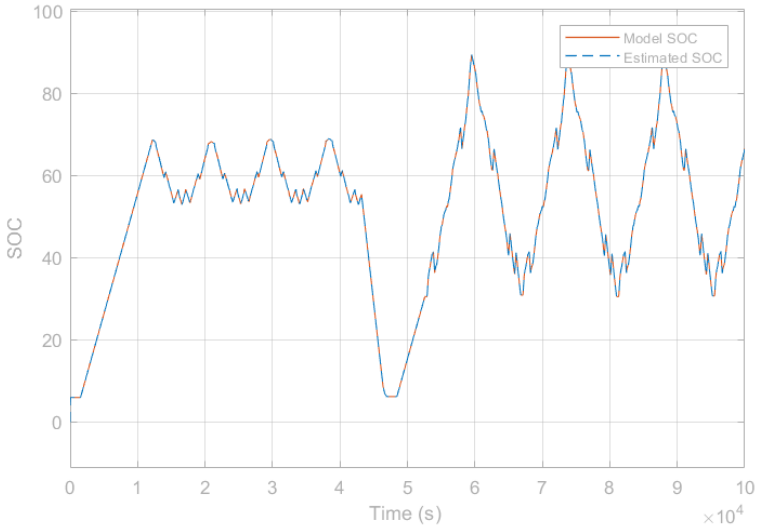

Figure 3.30: Model and estimated SOC by the second observer, without measurement noise, assuming constant parameters and initial conditions outside the flat region.

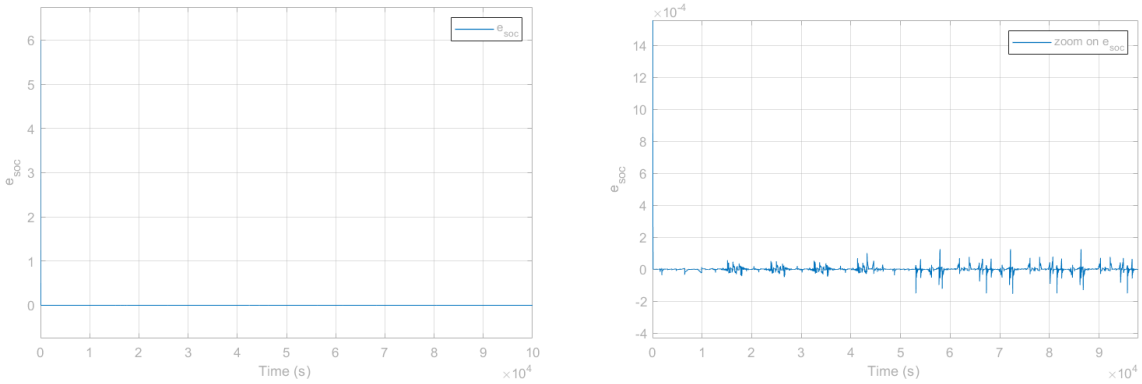

Figure 3.31: *SOC* estimation error by the second observer, without measurement noise, assuming constant parameters and initial conditions outside the flat region.

We notice a very good tracking of the estimated *SOC*. The estimation error is around 0.0001%. We also notice the immediate convergence of the observer.

Figures 3.32 and 3.33 show respectively model and estimated $\tilde{y}$, and its estimation error.

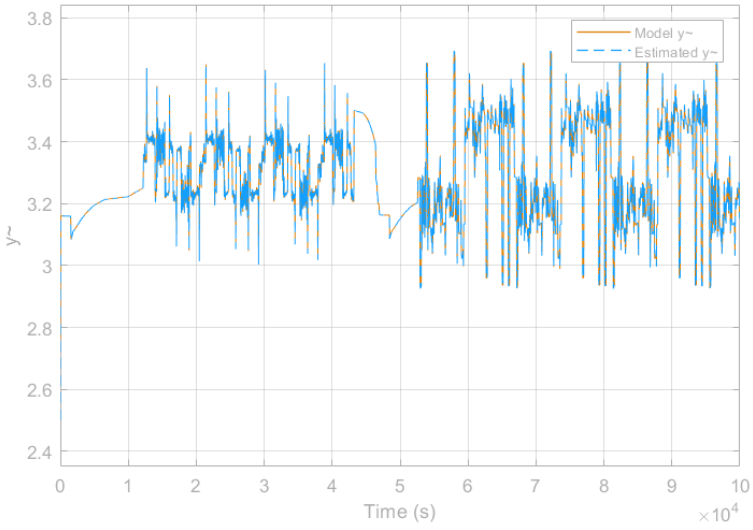

Figure 3.32: Model and estimated $\tilde{y}$ by the second observer, without measurement noise, assuming constant parameters and initial conditions outside the flat region.

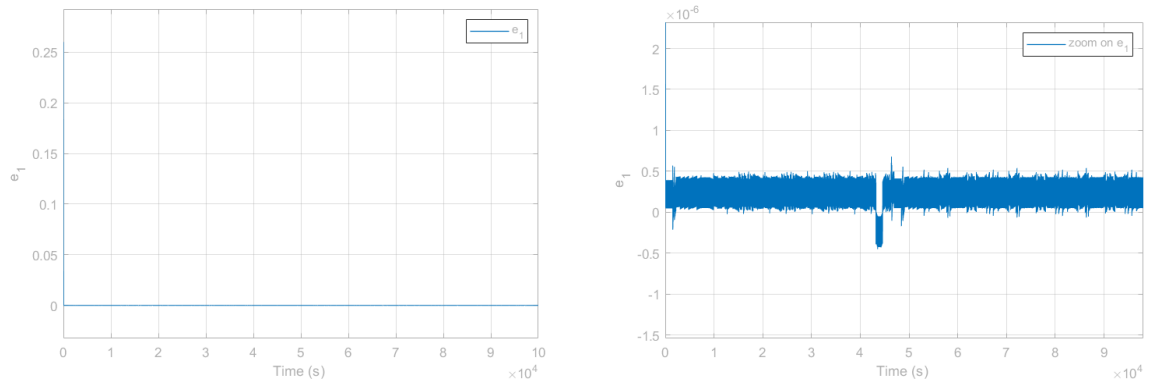

Figure 3.33: $\tilde{y}$ estimation error by the second observer, without measurement noise, assuming constant parameters and initial conditions outside the flat region.

The $\tilde{y}$ estimation error is less than $10^{-6}V$. The estimated $\tilde{y}$ tracks smoothly the real one.

Figures 3.34 and 3.35 show respectively model and estimated U_{RC}, and its estimation error.

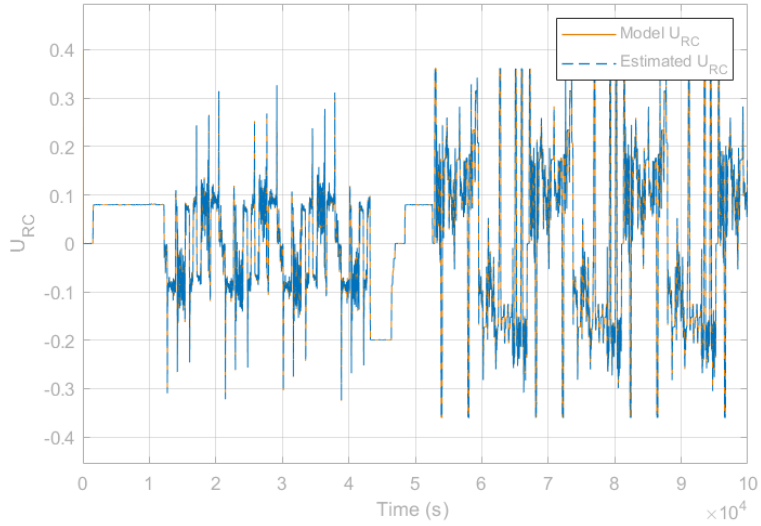

Figure 3.34: Model and estimated U_{RC} by the second observer, without measurement noise, assuming constant parameters and initial conditions outside the flat region.

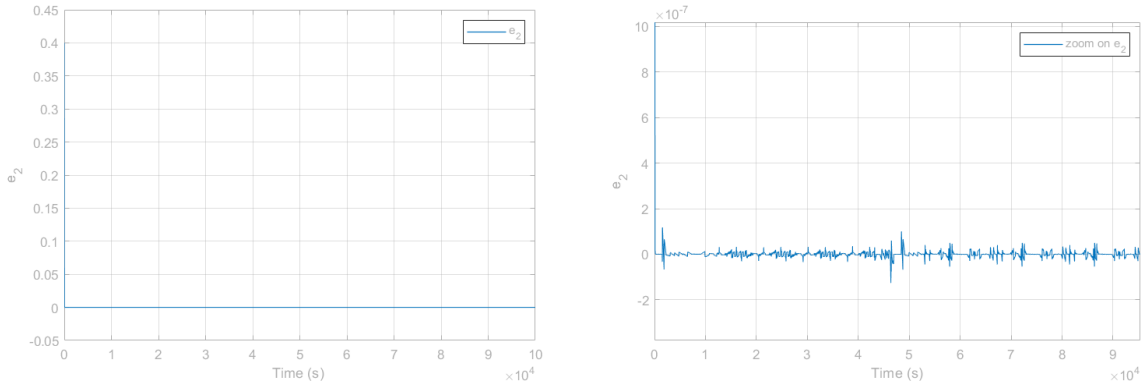

Figure 3.35: U_{RC} estimation error by the second observer, without measurement noise, assuming constant parameters and initial conditions outside the flat region.

We can see that, similarly for U_{RC}, its estimation error is on the order of 10^{-7}, which shows excellent tracking.

Now, we will consider both model and estimated SOC within the flat region as shown in Table 3.8.

Variables	$\tilde{y}(0)$	$U_{RC}(0)$	$SOC(0)$	$\hat{\tilde{y}}(0)$	$\hat{U}_{RC}(0)$	$\widehat{SOC}(0)$
Initial conditions	$V_{oc}(SOC(0))+U_{RC}(0)$	0.4	10	$V_{oc}(\widehat{SOC}(0))+\hat{U}_{RC}(0)$	0	90
Units	V	V	%	V	V	%

Table 3.8: Initial conditions.

Figures 3.36 and 3.37 show respectively model and estimated SOC, and its estimation error.

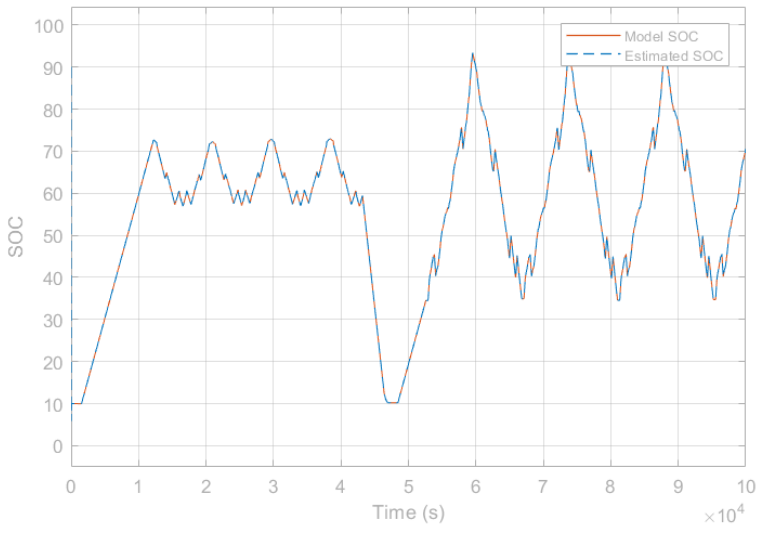

Figure 3.36: Model and estimated SOC by the second observer, without measurement noise, assuming constant parameters and initial conditions within the flat region.

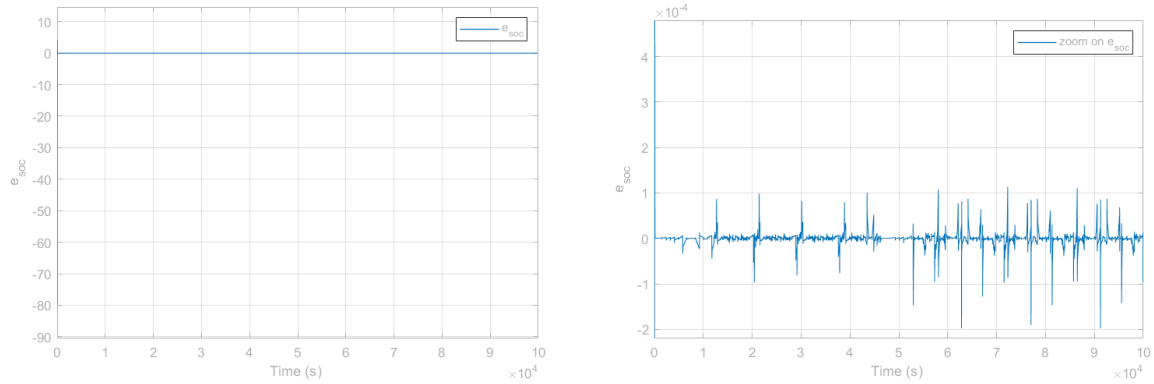

Figure 3.37: *SOC* estimation error by the second observer, without measurement noise, assuming constant parameters and initial conditions within the flat region.

We can once again observe the immediate convergence of the observer and the good tracking of the state of charge with an estimation error of 0.0001%, even while both initial conditions are chosen within the flat area.

Figures 3.38 and 3.39 show respectively model and estimated $\tilde{y}$, and its estimation error.

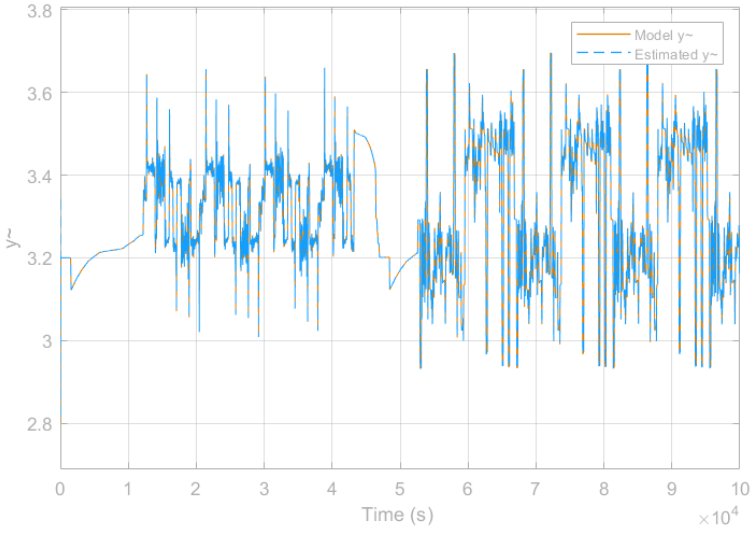

Figure 3.38: Model and estimated $\tilde{y}$ by the second observer, without measurement noise, assuming constant parameters and initial conditions within the flat region.

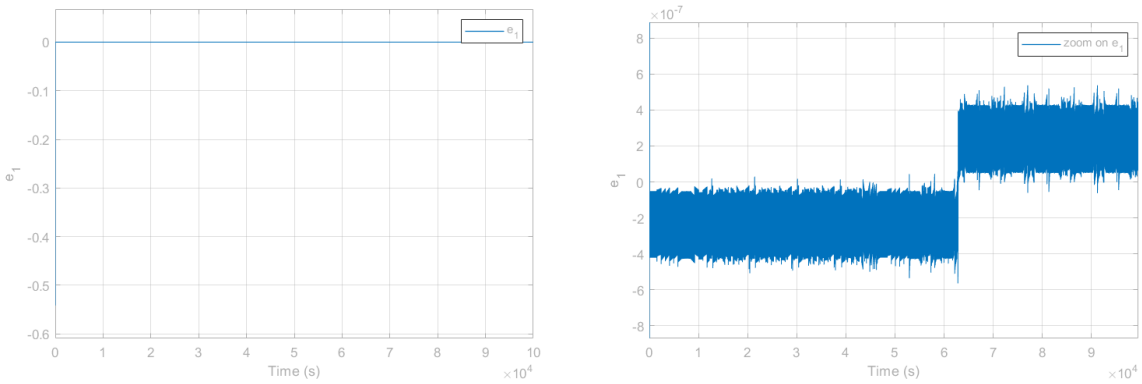

Figure 3.39: $\tilde{y}$ estimation error by the second observer, without measurement noise, assuming constant parameters and initial conditions within the flat region.

The $\tilde{y}$ estimation error is on the order of $10^{-7}V$, the estimated $\tilde{y}$ value is very close the the model $\tilde{y}$ one.

Figures 3.40 and 3.41 show respectively model and estimated U_{RC}, and its estimation error.

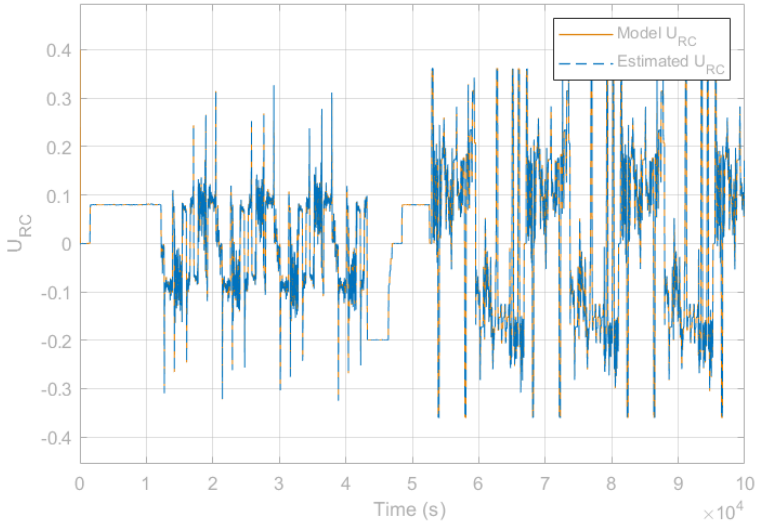

Figure 3.40: Model and estimated U_{RC} by the second observer, without measurement noise, assuming constant parameters and initial conditions within the flat region.

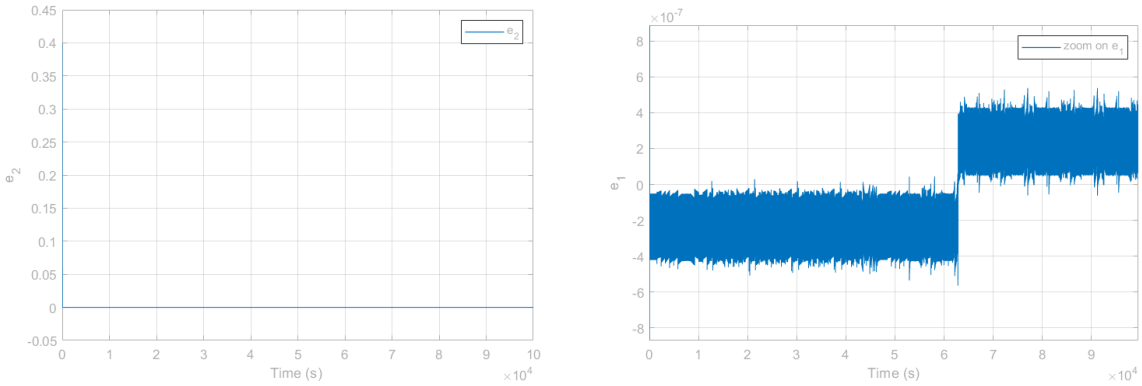

Figure 3.41: U_{RC} estimation error by the second observer, without measurement noise, assuming constant parameters and initial conditions within the flat region.

Likewise, the estimated U_{RC} value is very close to the model U_{RC} one. its estimation error is on the order of $10^{-7}V$.

We can notice that, regardless of the initial conditions chosen, all SOC, $\tilde{y}$ and U_{RC} exhibit flawless tracking with an estimation error as low as 10^{-4}, 10^{-6} and 10^{-7}, respectively.

Let us test the robustness of this observer to noise in the following.

•Under measurement noise

Using the same noise as for the conventional SMO, we will first consider both model and estimated SOC initial conditions outside the flat region as shown in Table 3.7.

Figures 3.42 and 3.43 show respectively model and estimated SOC and its estimation error.

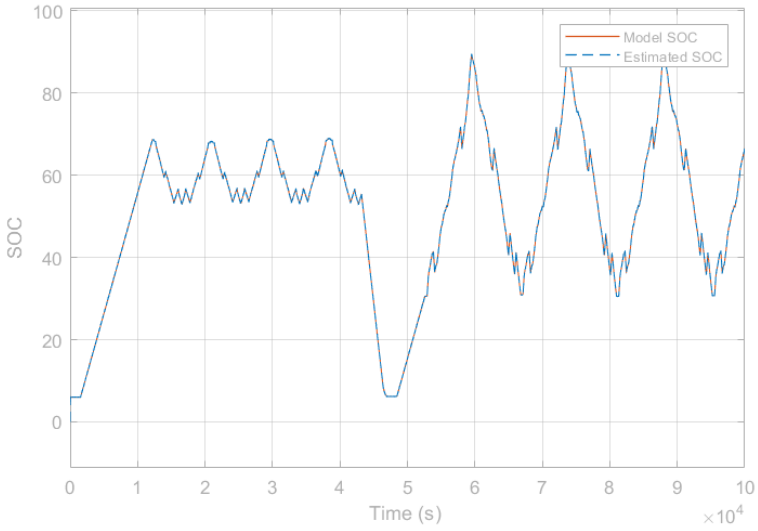

Figure 3.42: Model and estimated SOC by the second observer, under measurement noise, assuming constant parameters and initial conditions outside the flat region.

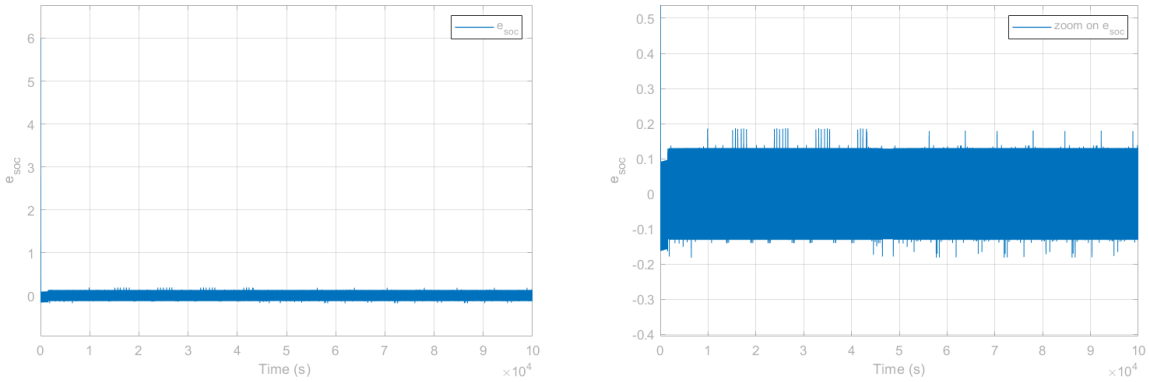

Figure 3.43: *SOC* estimation error by the second observer, under measurement noise, assuming constant parameters and initial conditions outside the flat region.

Even after adding noise to our model, the state of charge tracking is still good with an estimation error that increases to a maximum of 0.2% under noise. We also notice a rise in chattering.

Figures 3.44 and 3.45 show respectively model and estimated $\tilde{y}$ and its estimation error.

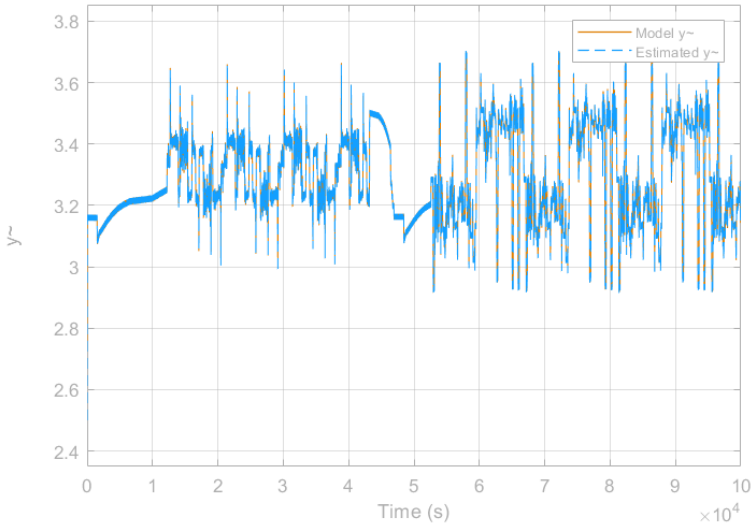

Figure 3.44: Model and estimated $\tilde{y}$ by the second observer, under measurement noise, assuming constant parameters and initial conditions outside the flat region.

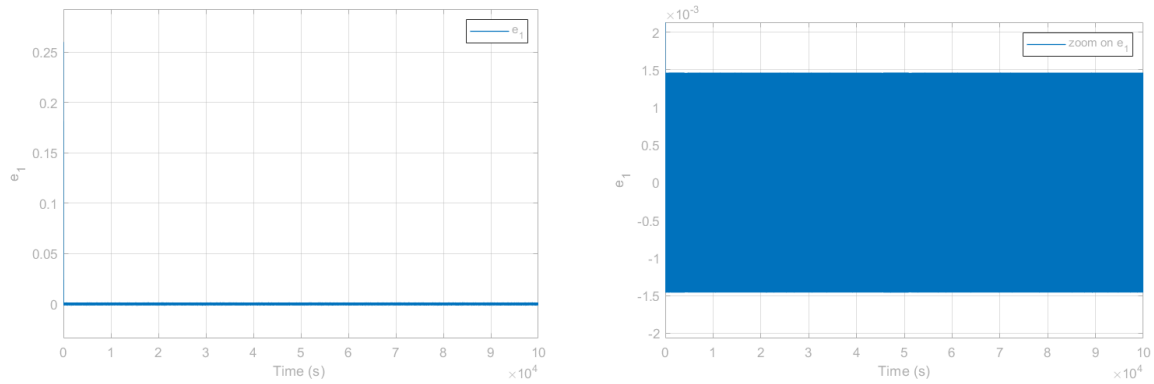

Figure 3.45: $\tilde{y}$ estimation error by the second observer, under measurement noise, assuming constant parameters and initial conditions outside the flat region.

The $\tilde{y}$ tracking is still good with an estimation error that increases to $10^{-3}V$ under noise.

Figures 3.46 and 3.47 show respectively model and estimated U_{RC} and its estimation error.

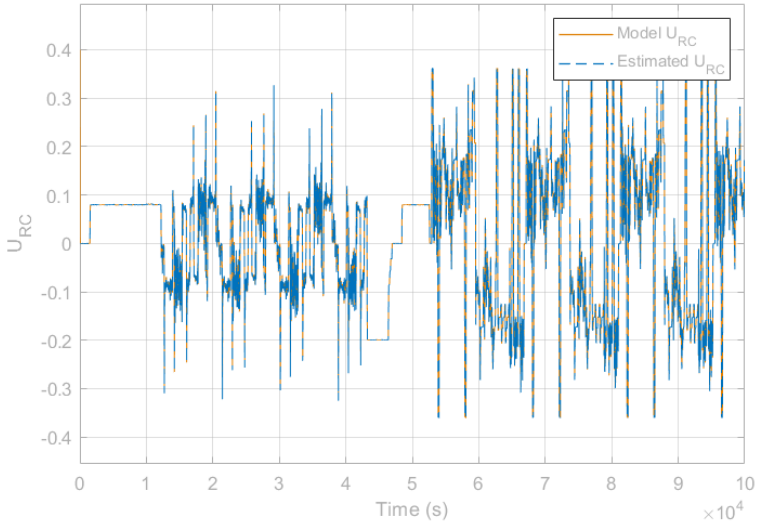

Figure 3.46: Model and estimated U_{RC} by the second observer, under measurement noise, assuming constant parameters and initial conditions outside the flat region.

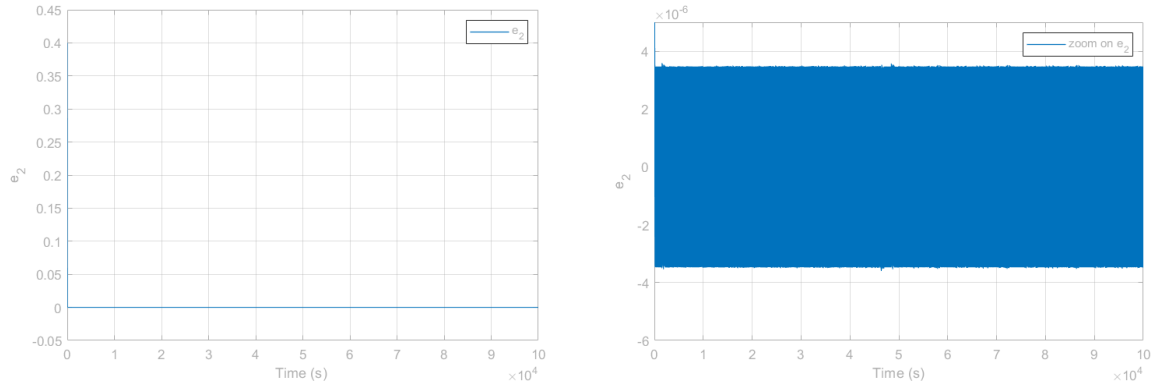

Figure 3.47: U_{RC} estimation error by the second observer, under measurement noise, assuming constant parameters and initial conditions outside the flat region.

Likewise, the U_{RC} estimation error increases to $10^{-6}V$ under noise, which still shows excellent tracking.

Next, we will consider both model and estimated SOC within the flat region as shown in Table 3.8.

Figures 3.48 and 3.49 show respectively model and estimated SOC, and its estimation error.

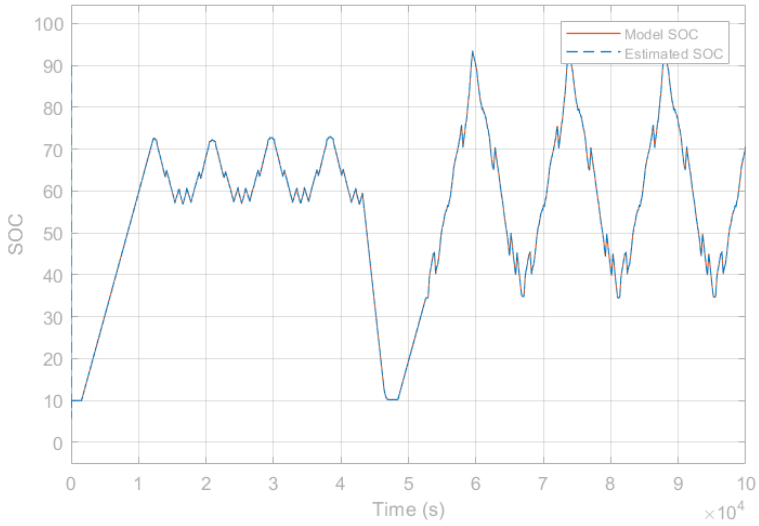

Figure 3.48: Model and estimated SOC by the second observer, under measurement noise, assuming constant parameters and initial conditions within the flat region.

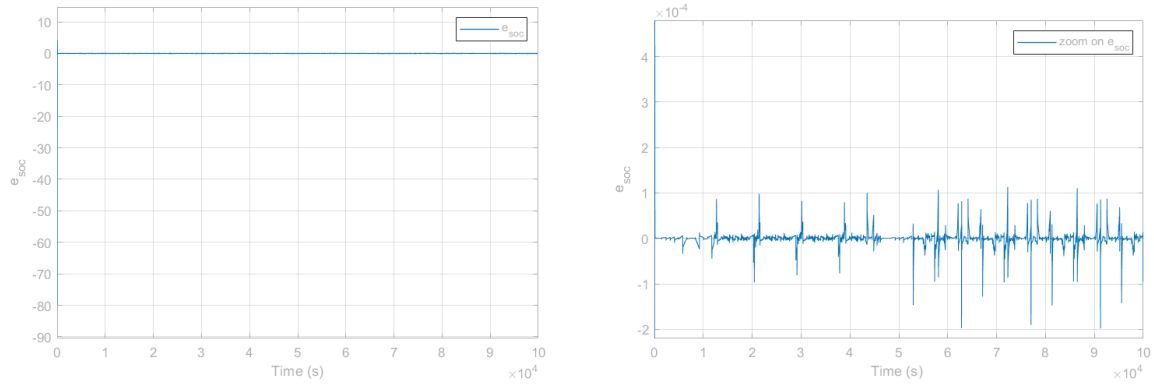

Figure 3.49: *SOC* estimation error by the second observer, under measurement noise, assuming constant parameters and initial conditions within the flat region.

Even when both model and estimated *SOC* initial conditions are taken within the flat region, the state of charge tracking is still good and its estimation error is on the order of $10^{-4}\%$.

Figures 3.50 and 3.51 show respectively model and estimated $\tilde{y}$, and its estimation error.

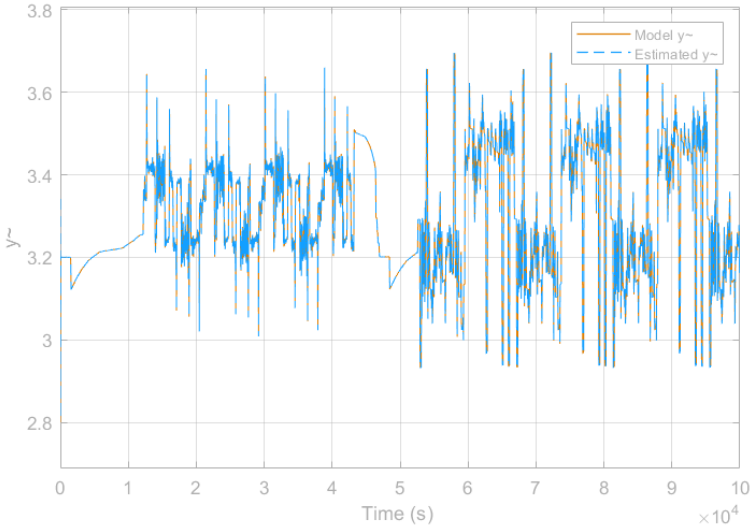

Figure 3.50: Model and estimated $\tilde{y}$ by the second observer, under measurement noise, assuming constant parameters and initial conditions within the flat region.

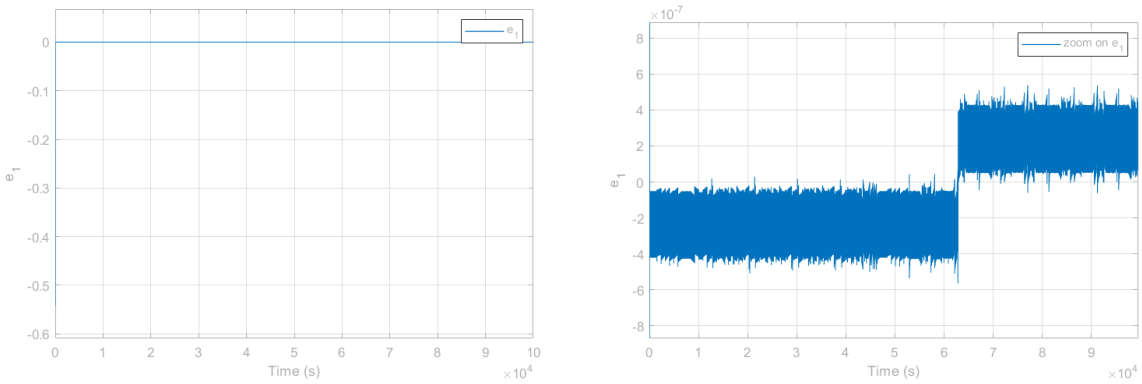

Figure 3.51: $\tilde{y}$ estimation error by the second observer, under measurement noise, assuming constant parameters and initial conditions within the flat region.

Likewise, the $\tilde{y}$ estimation error is on the order of 10^{-7}, the tracking is excellent.

Figures 3.52 and 3.53 show respectively model and estimated U_{RC}, and its estimation error.

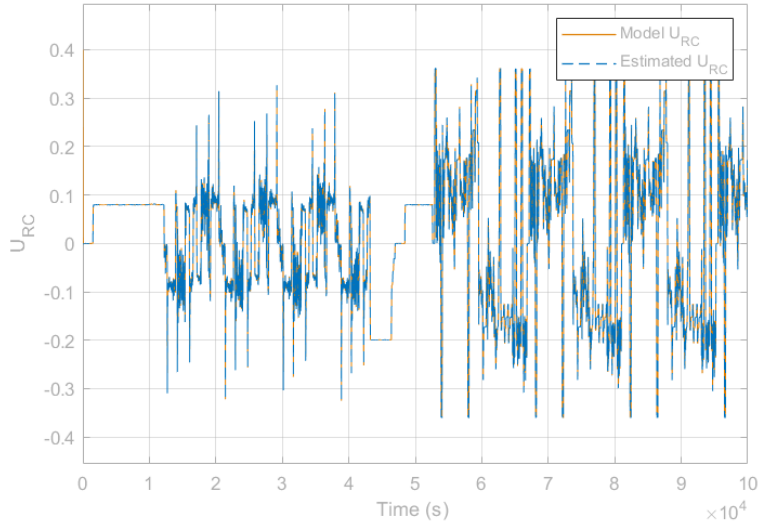

Figure 3.52: Model and estimated U_{RC} by the second observer, under measurement noise, assuming constant parameters and initial conditions within the flat region.

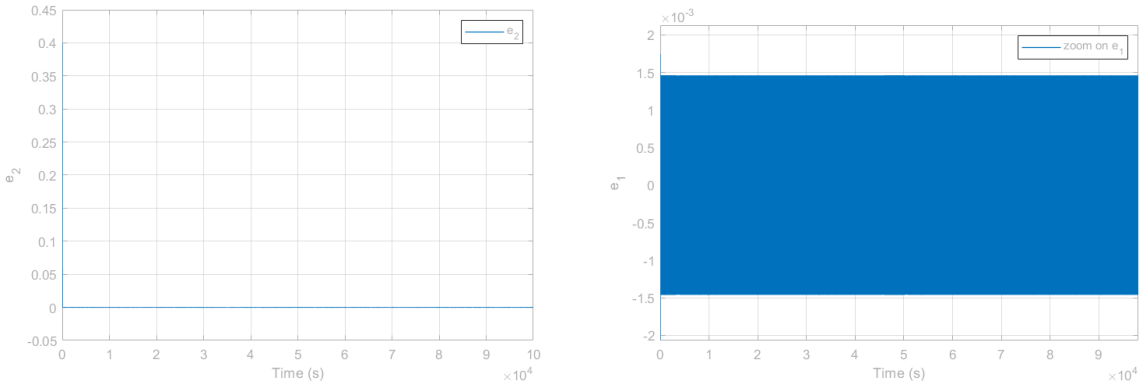

Figure 3.53: U_{RC} estimation error by the second observer, under measurement noise, assuming constant parameters and initial conditions within the flat region.

Lastly, the U_{RC} estimation error is on the order of $10^{-3}V$, which is still good and shows the good performance of the observer.

We notice then that the alternative SMO estimates smoothly all states even under noise and regardless of the initial conditions chosen which proves the robustness of the system.

3.4 Conclusion

In this chapter, we developed two distinct sliding mode observers with the primary goal of accurately estimating the state of charge, regardless of the flat region within the open circuit voltage. We validated the effectiveness of these observers through rigorous Lyapunov analysis. Additionally, we conducted comprehensive numerical simulations, exploring various initial conditions while accounting for both noise-free and noisy measurements, all while assuming known and constant parameters. Our findings revealed good performance from both observers, with smooth state tracking and acceptable estimation errors.

In the upcoming chapter, we will relax the assumption of constant parameters by incorporating their real values, which will depend on battery current (I), temperature (T), and state of charge (SOC). This step will serve as a rigorous test of observer accuracy. Furthermore, we will conduct a comparative analysis of these observers.

Parameters dependencies

Chapter 4

Parameters dependencies

In the previous chapter, we successfully developed and simulated two state observers to estimate the state of charge, assuming constant parameters. However, in order to enhance the realism and accuracy of our model, we must now challenge this assumption. We will move forward by incorporating real-world parameters that dynamically vary with temperature, state of charge, and battery current. Within our Matlab model, each of these parameters was contingent upon dedicated look-up tables driven from SAFT Matlab model, constructed from experimental data. They were conditioned by the current (I), temperature (T), and generated SOC as inputs into their respective look-up tables. Finally we will compare between the two built observers.

4.1 Conventional sliding mode observer

Considering the parameters dependencies on the battery current I, the temperature T and the state of charge SOC, the model (3.6) becomes

$$\begin{cases} \dot{\tilde{y}} = -\frac{1}{\tau(T)}\tilde{y} + \frac{1}{\tau(T)}V_{oc}(SOC) + I\Big(-\frac{1}{C(I,T,SOC)} + \frac{100}{Q}\frac{\partial V_{oc}(SOC)}{\partial SOC}\Big) \\ \dot{SOC} = 100\frac{I}{Q} \end{cases} \tag{4.1}$$

Since one has $\tilde{y} = V_{oc}(SOC) - U_{RC} = y + R_0(I,T,SOC)I$, the model (4.1) becomes

$$\begin{cases} \dot{\tilde{y}} = -\frac{1}{\tau(T)}(y + R_0(I,T,SOC)I) + \frac{1}{\tau(T)}V_{oc}(SOC) + I\beta \\ \dot{SOC} = 100\frac{I}{Q} \\ y = \tilde{y} - R_0(I,T,SOC)I \end{cases} \tag{4.2}$$

where $\beta = \Big(-\frac{1}{C(I,T,SOC)} + \frac{100}{Q}\frac{\partial V_{oc}(SOC)}{\partial SOC}\Big)$, the states vector is $x = \begin{pmatrix} \tilde{y} \\ SOC \end{pmatrix}$; and the measured output is y.

4.1.1 Observer equations

The conventional SMO equations are given below

$$\begin{cases} \dot{\hat{\tilde{y}}} = -\dfrac{1}{\tau(T)}\hat{\tilde{y}} + \dfrac{1}{\tau(T)}V_{oc}(\widehat{SOC}) + I\hat{\beta} + L_1\text{sign}(e_1) \\ \dot{\widehat{SOC}} = 100\dfrac{I}{Q} + L_2\text{sign}(e_1) \\ \hat{y} = \hat{\tilde{y}} - R_0(I,T,\widehat{SOC})I \end{cases} \tag{4.3}$$

where $\hat{\beta} = \Big(-\frac{1}{C(I,T,\widehat{SOC})} + \frac{100}{Q}\frac{\partial V_{oc}(\widehat{SOC})}{\partial SOC}\Big)$, $e_1 := y - \hat{y} := (\tilde{y} - R_0(I,T,SOC)I) - (\hat{\tilde{y}} - R_0(I,T,\widehat{SOC})I)$

4.2 Alternative sliding mode observer

Considering the parameters dependencies on the battery current I, the temperature T and the state of charge SOC, the model (3.30) becomes

$$\begin{cases} \dot{\tilde{y}} = \dfrac{1}{\tau(T)}U_{RC} + I\Big(-\dfrac{1}{C(I,T,SOC)} + \dfrac{100}{Q}\dfrac{\partial V_{oc}(SOC)}{\partial SOC}\Big) \\ \dot{U}_{RC} = -\dfrac{U_{RC}}{\tau(T)} + \dfrac{I}{C(I,T,SOC)} \\ y = \tilde{y} - R_0(I,T,SOC)I \end{cases} \tag{4.4}$$

4.2.1 Observer equations

The alternative SMO equations are given below

$$\begin{cases} \dot{\hat{\tilde{y}}} = \dfrac{1}{\tau(T)}\hat{U}_{RC} - \dfrac{1}{C(I,T,\widehat{SOC})}I + \dfrac{\partial V_{oc}(\widehat{SOC})}{\partial SOC}\Big(100\dfrac{I}{Q}\Big) + L_{11}e_1 + L_{12}\text{sign}(e_1) \\ \dot{\hat{U}}_{RC} = -\dfrac{1}{\tau(T)}\hat{U}_{RC} + \dfrac{1}{C(I,T,\widehat{SOC})}I + L_2e_1 \\ \dot{\widehat{SOC}} = -\alpha_{13}\text{sign}(e_3) - \alpha_{23}e_3 + 100\dfrac{I}{Q} \end{cases} \tag{4.5}$$

where $e_1 := y - \hat{y} := (\tilde{y} - R_0(I,T,SOC)I) - (\hat{\tilde{y}} - R_0(I,T,\widehat{SOC})I)$, $e_3 := V_{oc}(\widehat{SOC}) - \hat{V}_{oc}$, $\hat{V}_{oc} := \hat{\tilde{y}} + \hat{U}_{RC}$

4.3 Numerical simulations for the conventional SMO

Numerical simulations will be conducted using the same current profile used in Chapter 3 as an input as shown in Figure 4.1. We will simulate, as done in Chapter 3, for different initial conditions without and under measurement noise. The real parameters values are obtained from SAFT Matlab Model.

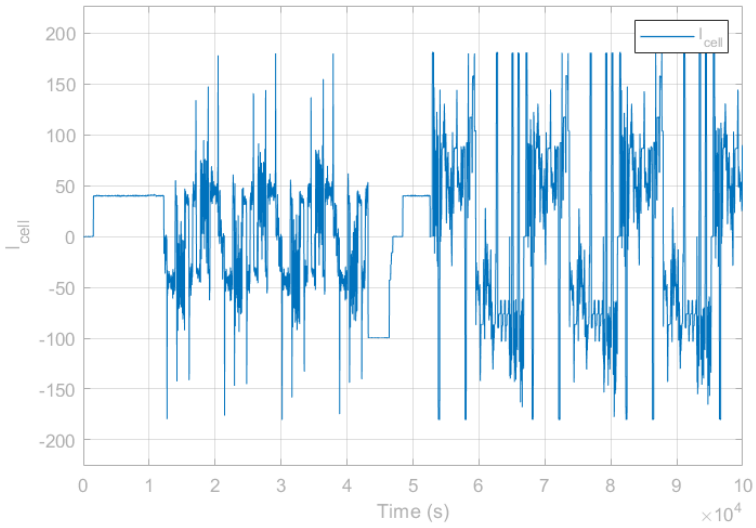

Figure 4.1: First current profile.

4.3.1 Without measurement noise

We will start by presenting simulations of the conventional SMO without the presence of measurement noise. These simulations encompass various initial conditions and employ the first current profile.
We will first consider both model and estimated SOC initial conditions outside the flat region as shown in Table 4.1.

Variables	$SOC(0)$	$\widehat{SOC}(0)$	$\tilde{y}(0)$	$\hat{\tilde{y}}(0)$	L_1	L_2
Values	6	0	2.7	0	20	70
Units	%	%	V	V		

Table 4.1: Initial conditions and gain values.

Figures 4.2 and 4.3 show respectively model and estimated SOC, and its estimation error.

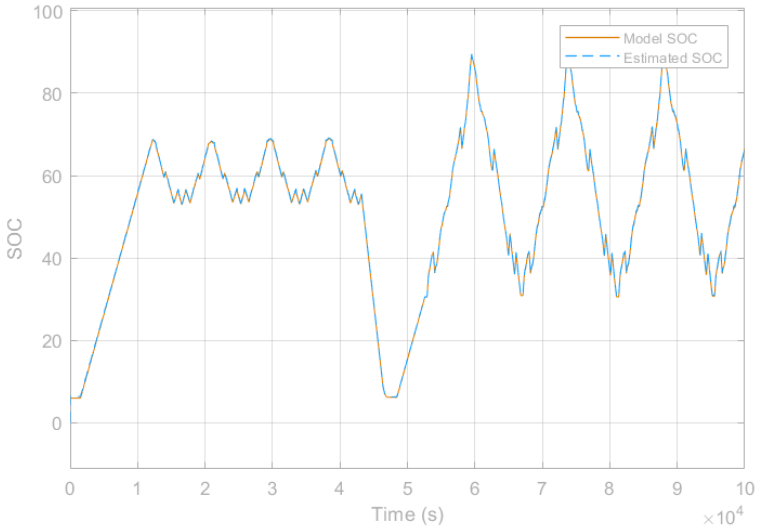

Figure 4.2: Model and estimated *SOC* by the first observer, considering parameter dependencies and initial conditions outside the flat region.

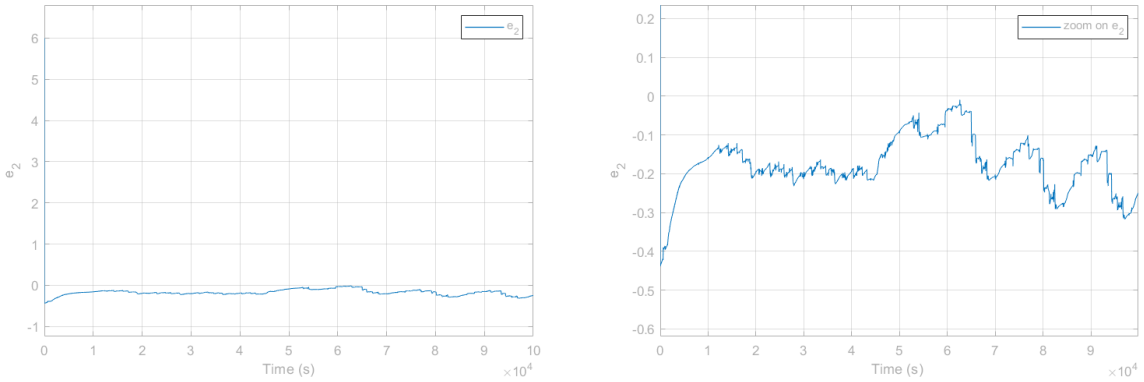

Figure 4.3: *SOC* estimation error by the first observer, considering parameter dependencies and initial conditions outside the flat region.

We can notice that the state of charge tracking is good with an estimation error ranging between 0% and 0.4%.

Figures 4.4 and 4.5 show respectively model and estimated $\tilde{y}$, and the output estimation error.

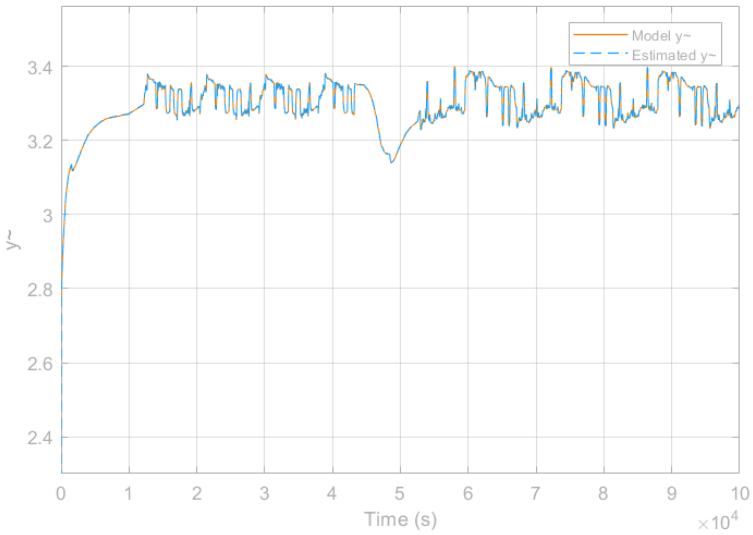

Figure 4.4: Model and estimated $\tilde{y}$ by the first observer, considering parameter dependencies and initial conditions outside the flat region.

We can see the smooth tracking of $\tilde{y}$ in Figure 4.4.

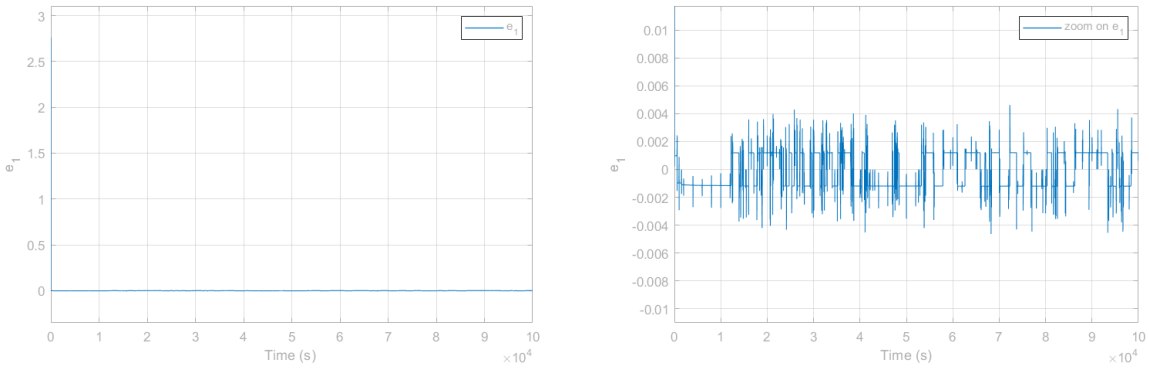

Figure 4.5: The output estimation error by the first observer, considering parameter dependencies and initial conditions outside the flat region.

The output estimation error does not exceed $0.005V$ which shows a good estimation of y.

Now, we will consider both model and estimated SOC initial conditions within the flat region as shown in Table 4.2.

Variables	$SOC(0)$	$\widehat{SOC}(0)$	$\tilde{y}(0)$	$\hat{\tilde{y}}(0)$	L_1	L_2
Values	10	90	2.7	0	20	70
Units	%	%	V	V		

Table 4.2: Initial conditions and gain values.

Figures 4.6 and 4.7 show respectively model and estimated SOC, and its estimation error.

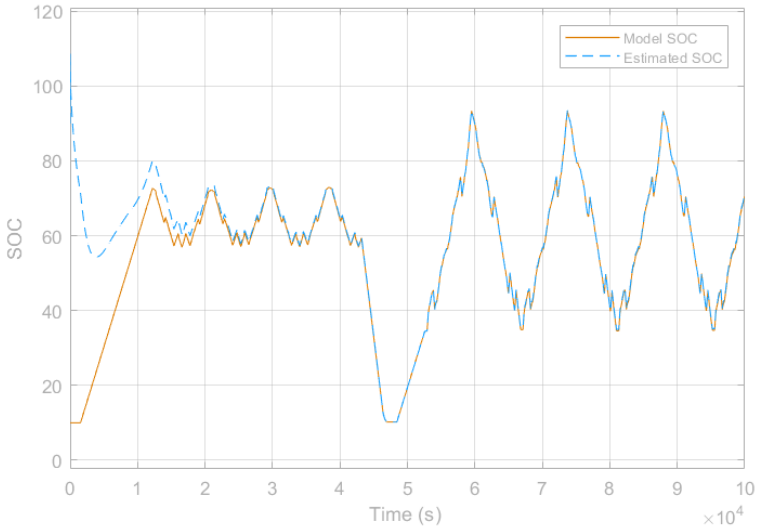

Figure 4.6: Model and estimated *SOC* by the first observer, considering parameter dependencies and initial conditions within the flat region.

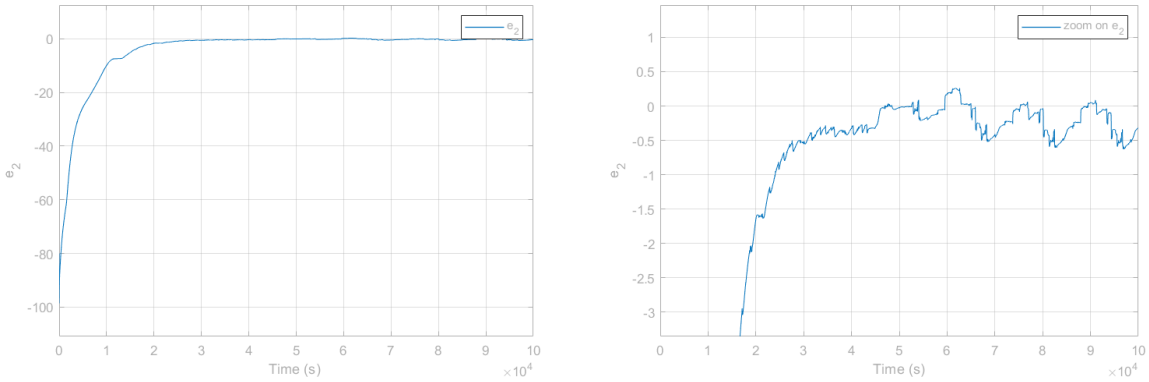

Figure 4.7: *SOC* estimation error by the first observer, considering parameter dependencies and initial conditions within the flat region.

We can observe that even when both initial conditions are situated within the flat region, the state of charge estimation remains accurate, with an estimation error ranging from 0

Figures 4.8 and 4.9 show respectively model and estimated $\tilde{y}$, and the output estimation error.

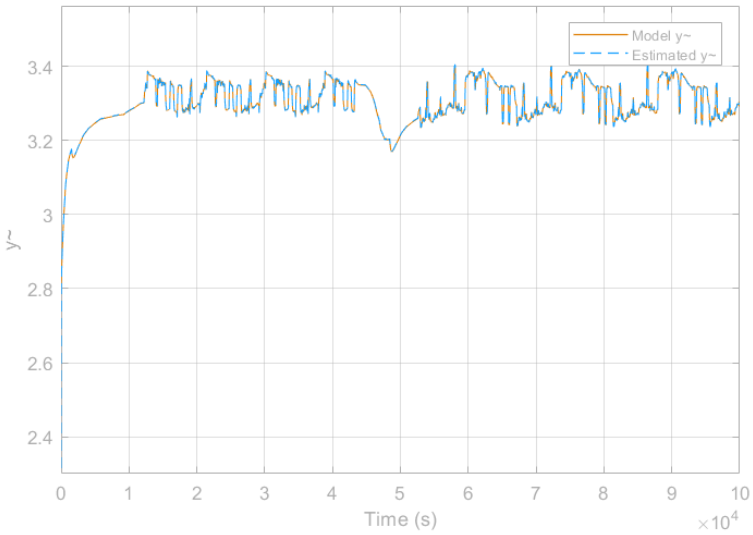

Figure 4.8: Model and estimated $\tilde{y}$ by the first observer, considering parameter dependencies and initial conditions within the flat region.

Similarly, the $\tilde{y}$ estimation is smooth regardless of the initial conditions chosen.

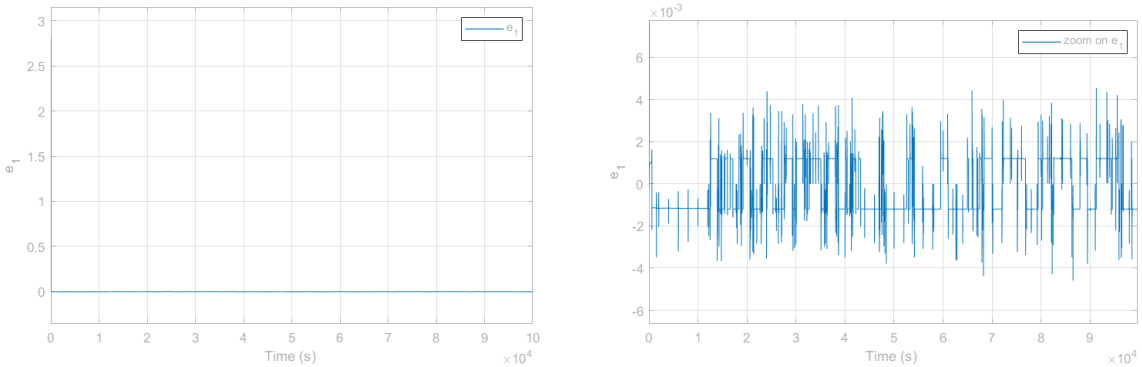

Figure 4.9: y estimation error by the first observer, considering parameter dependencies and initial conditions within the flat region.

Likewise, the output estimation error is on the order of $10^{-3}V$.

4.3.2 Under measurement noise

We will now present the simulations conducted under measurement noise to test the robustness of the conventional SMO with the real parameters.
We will first consider both model and estimated SOC initial conditions outside the flat region as shown in Table 4.1.
Figures 4.10 and 4.11 show respectively model and estimated SOC, and its estimation error.

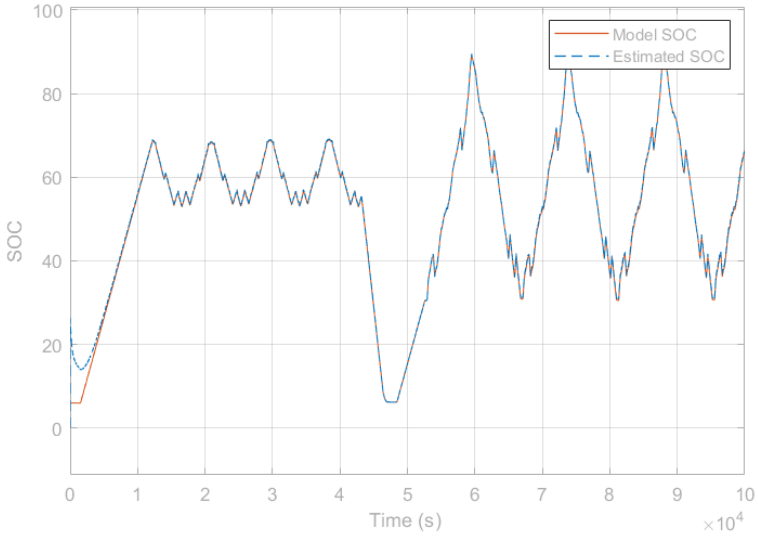

Figure 4.10: Model and estimated *SOC* by the first observer, under measurement noise, considering parameter dependencies and initial conditions outside the flat region.

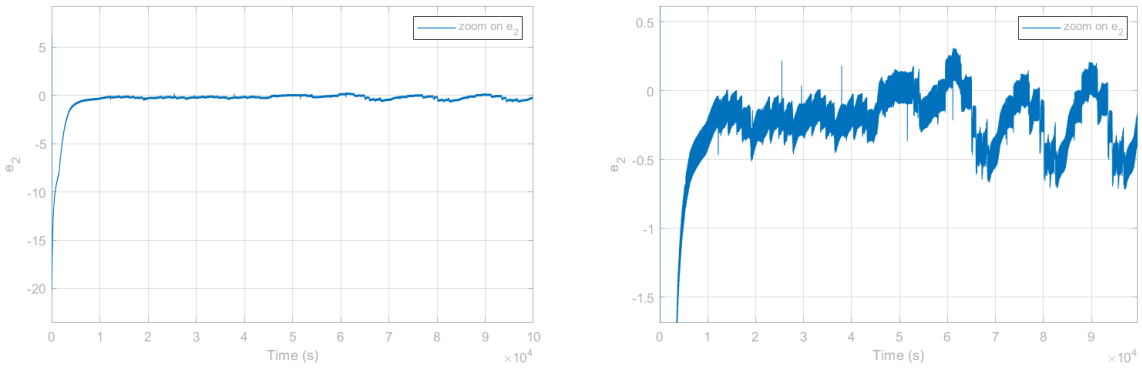

Figure 4.11: *SOC* estimation error by the first observer, under measurement noise, considering parameter dependencies and initial conditions outside the flat region.

We can notice that the state of charge tracking is good with an estimation error ranging between 0% and 0.4%.

Figures 4.12 and 4.13 show respectively model and estimated $\tilde{y}$, and the output estimation error.

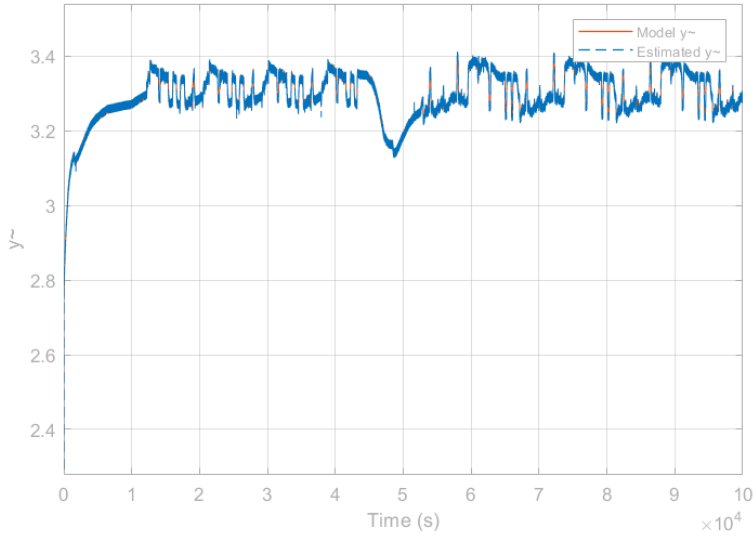

Figure 4.12: Model and estimated $\tilde{y}$ by the first observer, under measurement noise, considering parameter dependencies and initial conditions outside the flat region.

We can see the smooth tracking of $\tilde{y}$ in Figure 4.12.

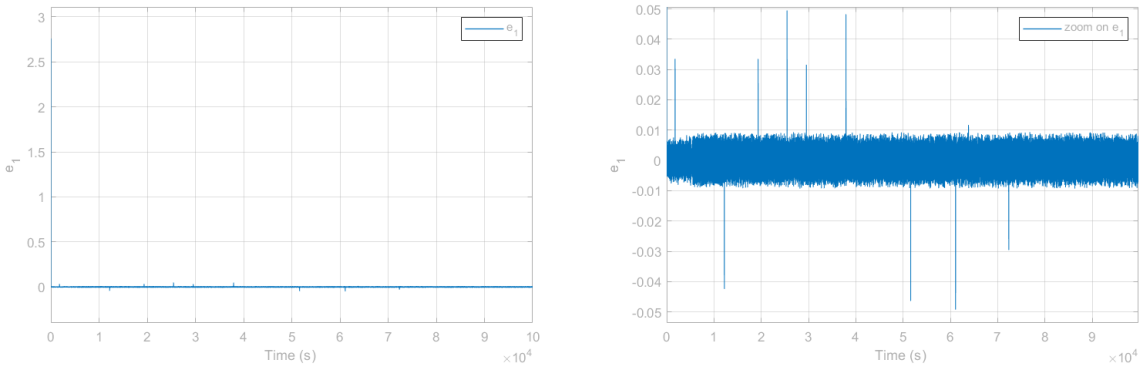

Figure 4.13: The output estimation error by the first observer, under measurement noise, considering parameter dependencies and initial conditions outside the flat region.

The output estimation error does not exceed $0.05V$ which shows a good estimation of y.

Next, we will consider both model and estimated SOC initial conditions within the flat region as shown in Table 4.2.

Figures 4.14 and 4.15 show respectively model and estimated SOC, and its estimation error.

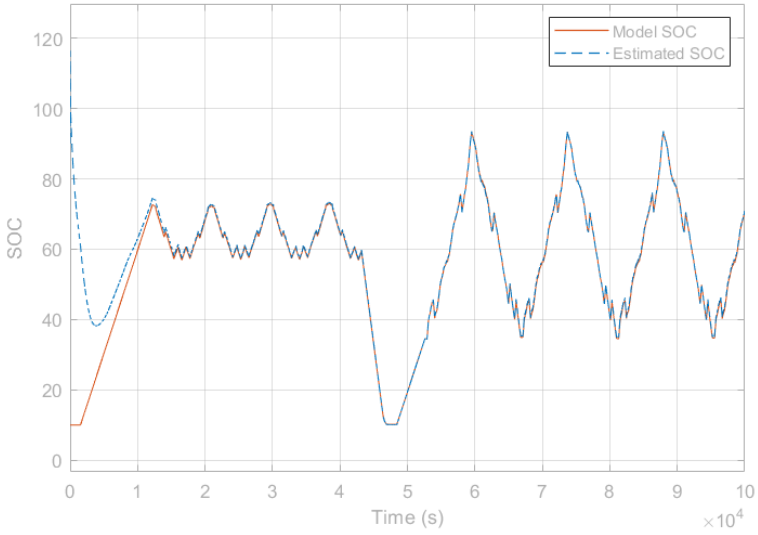

Figure 4.14: Model and estimated *SOC* by the first observer, under measurement noise, considering parameter dependencies and initial conditions within the flat region.

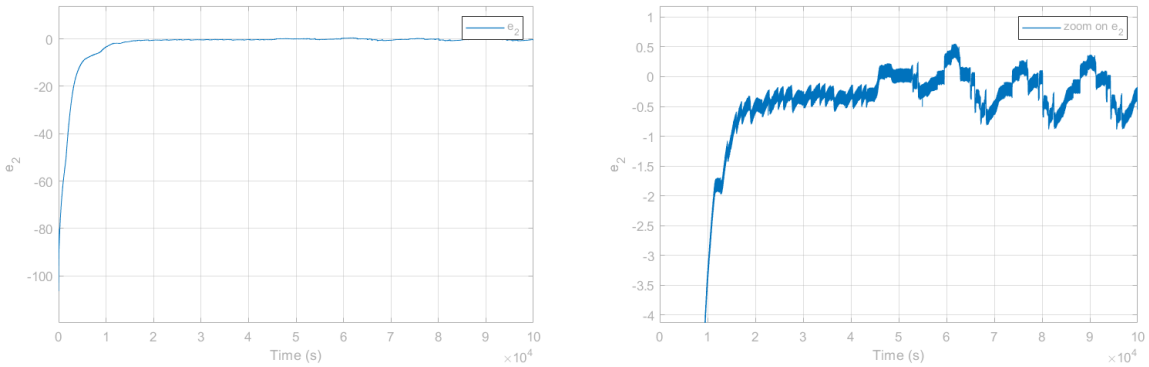

Figure 4.15: *SOC* estimation error by the first observer, under measurement noise, considering parameter dependencies and initial conditions within the flat region.

We can observe that even when both initial conditions are situated within the flat region, the state of charge estimation remains accurate, with an estimation error ranging between 0% and 0.6%.

Figures 4.16 and 4.17 show respectively model and estimated $\tilde{y}$, and the output estimation error.

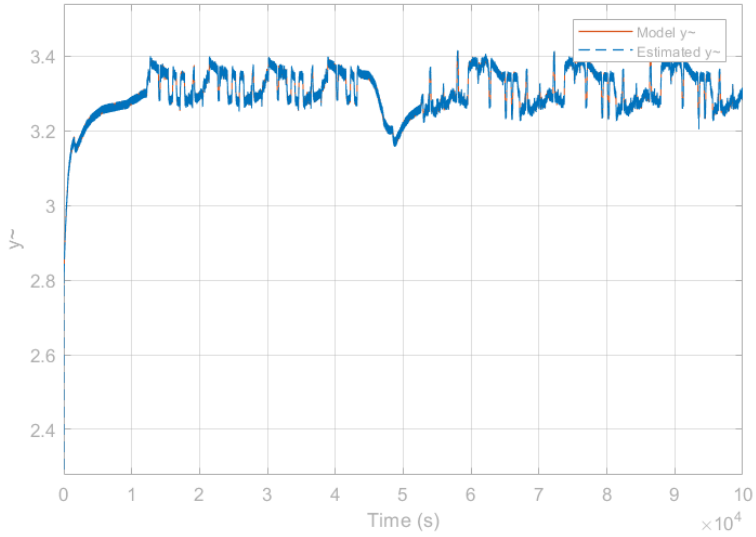

Figure 4.16: Model and estimated $\tilde{y}$ by the first observer, under measurement noise, considering parameter dependencies and initial conditions within the flat region.

Similarly, the $\tilde{y}$ estimation is smooth regardless of the initial conditions chosen.

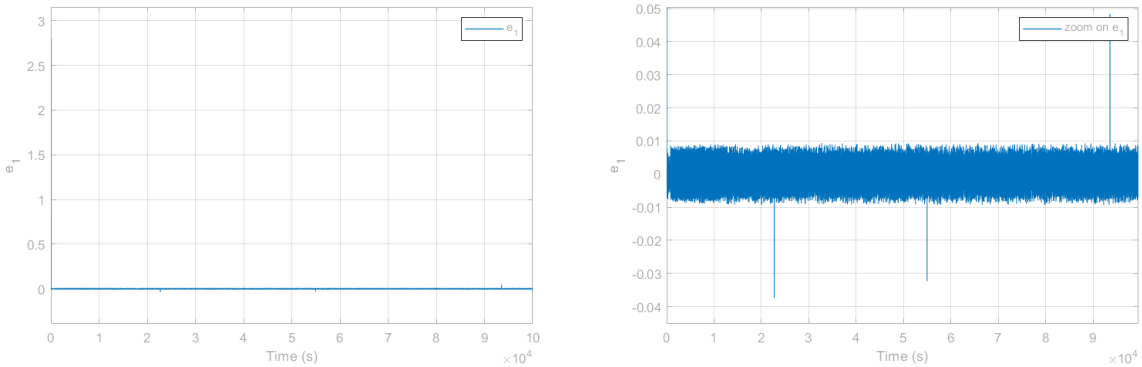

Figure 4.17: y estimation error by the first observer, under measurement noise, considering parameter dependencies and initial conditions within the flat region.

Likewise, the output estimation error is mostly on the order of $0.01V$.
We observed that the conventional SMO maintains its performance even in the presence of parameter dependencies. The simulations consistently exhibited minimal estimation errors and reliable tracking.

In the next section, we will present the numerical simulations conducted on the second observer in order to do a comparison between both observers.

4.4 Numerical simulations for the alternative SMO

We now proceed to present the simulations conducted for the alternative SMO, both in the absence and presence of measurement noise, using the first current profile.

4.4.1 Without measurement noise

We will consider both model and estimated SOC initial conditions outside the flat region as shown in Table 4.1.
Figures 4.18 and 4.19 show respectively model and estimated SOC, and its estimation error.

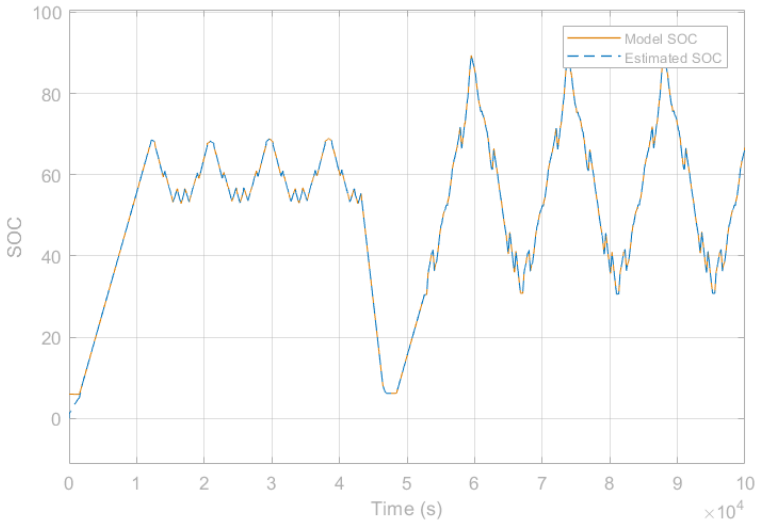

Figure 4.18: Model and estimated SOC by the second observer, considering parameter dependencies and initial conditions outside the flat region.

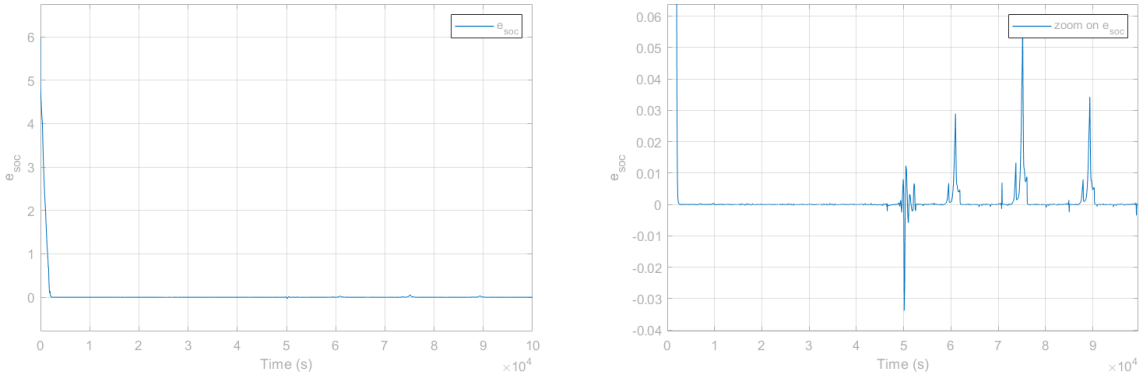

Figure 4.19: SOC estimation error by the second observer, considering parameter dependencies and initial conditions outside the flat region.

We notice that the SOC estimation error does not exceed 0.06%. We also notice the fast convergence of the alternative observer.

Figures 4.20 and 4.21 show respectively model and estimated U_{RC}, and its estimation error.

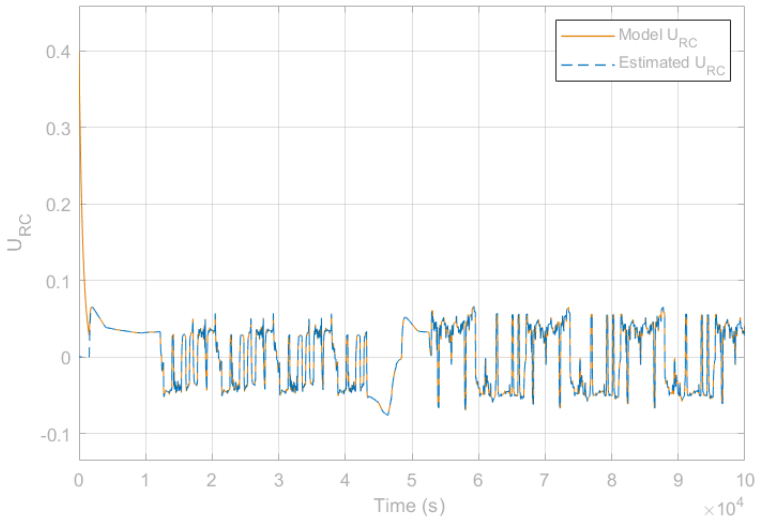

Figure 4.20: Model and estimated U_{RC} by the second observer, considering parameter dependencies and initial conditions outside the flat region.

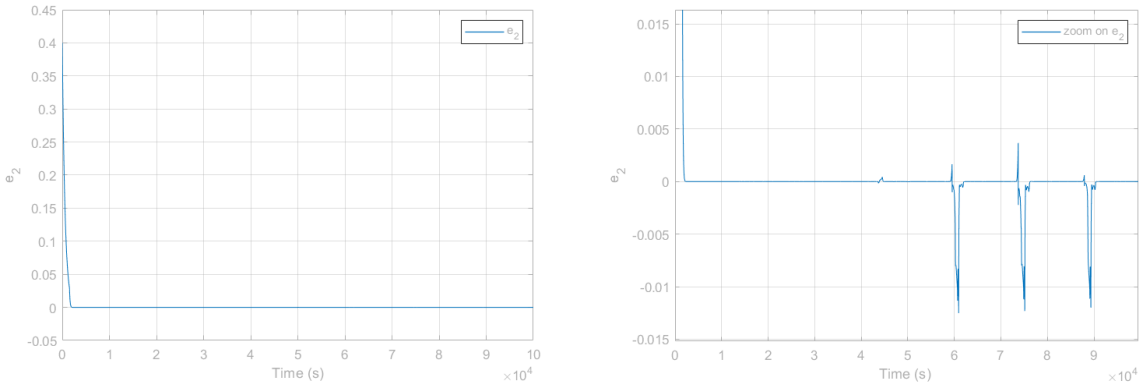

Figure 4.21: U_{RC} estimation error by the second observer, considering parameter dependencies and initial conditions outside the flat region.

The U_{RC} estimation error ranges between $0V$ and $0.01V$.

Figures 4.22 and 4.23 show respectively model and estimated $\tilde{y}$, and the output estimation error.

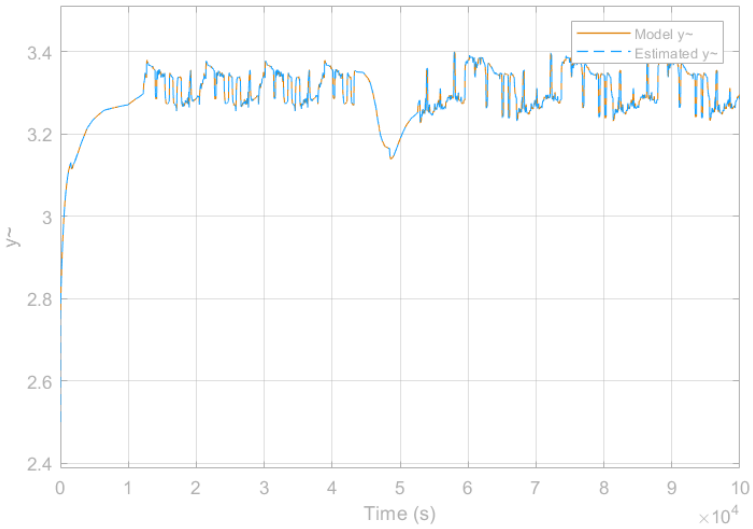

Figure 4.22: Model and estimated $\tilde{y}$ by the second observer, considering parameter dependencies and initial conditions outside the flat region.

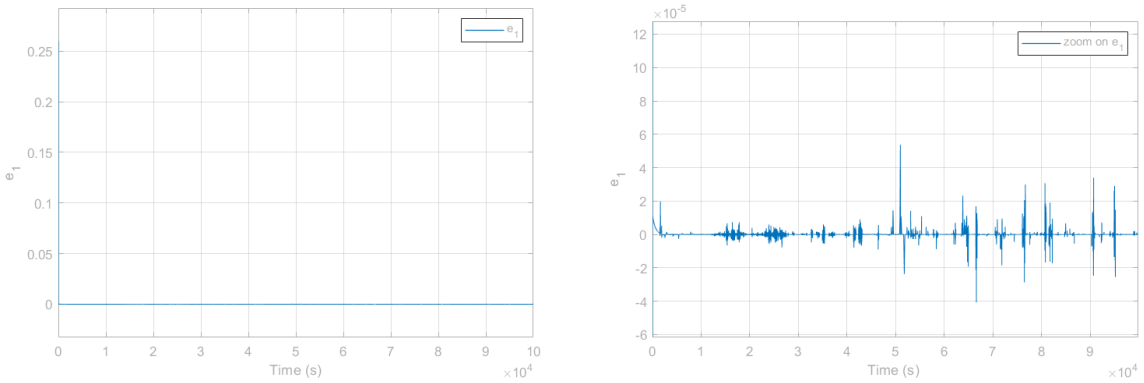

Figure 4.23: The output estimation error by the second observer, considering parameter dependencies and initial conditions outside the flat region.

The output estimation error is on the order off $10^{-5}V$, which shows the good tracking of the observer.

Next, we will consider both model and estimated SOC initial conditions within the flat region as shown in Table 4.2.
Figures 4.24 and 4.25 show respectively model and estimated SOC, and its estimation error.

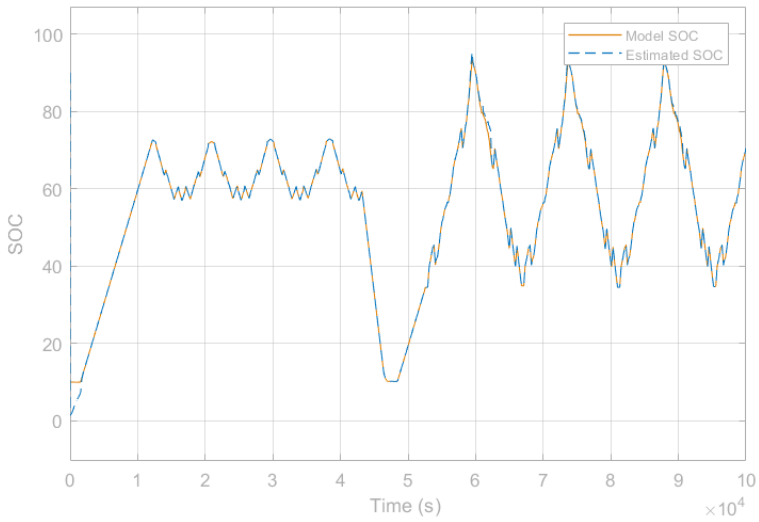

Figure 4.24: Model and estimated *SOC* by the second observer, considering parameter dependencies and initial conditions within the flat region.

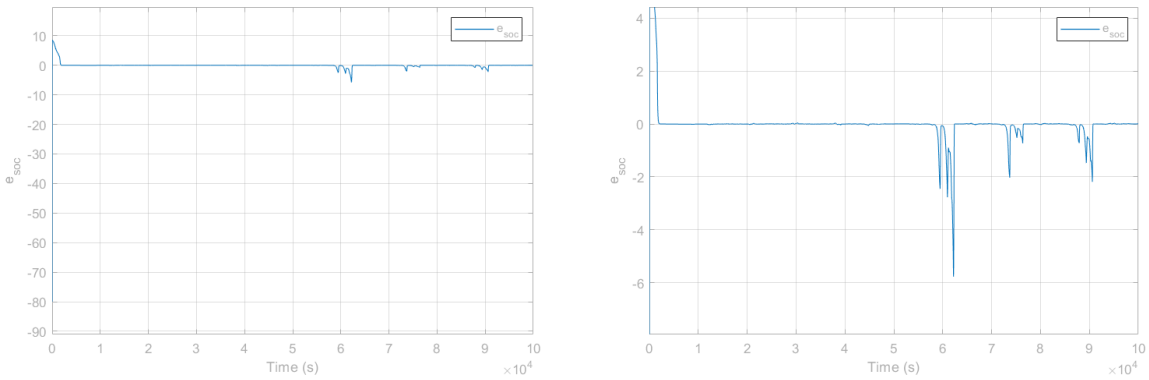

Figure 4.25: *SOC* estimation error by the second observer, considering parameter dependencies and initial conditions within the flat region.

We observe that, in this scenario, the estimation error for SOC experiences an increase when compared to the results of previous simulations.

Figures 4.26 and 4.27 show respectively model and estimated U_{RC}, and its estimation error.

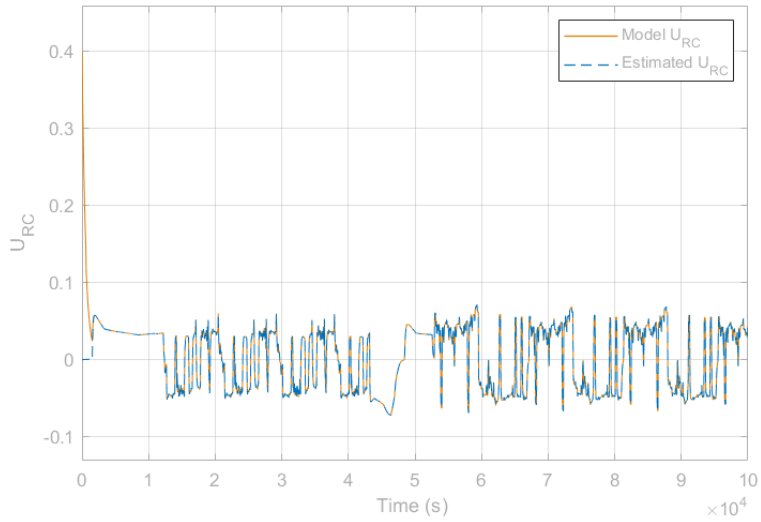

Figure 4.26: Model and estimated U_{RC} by the second observer, considering parameter dependencies and initial conditions within the flat region.

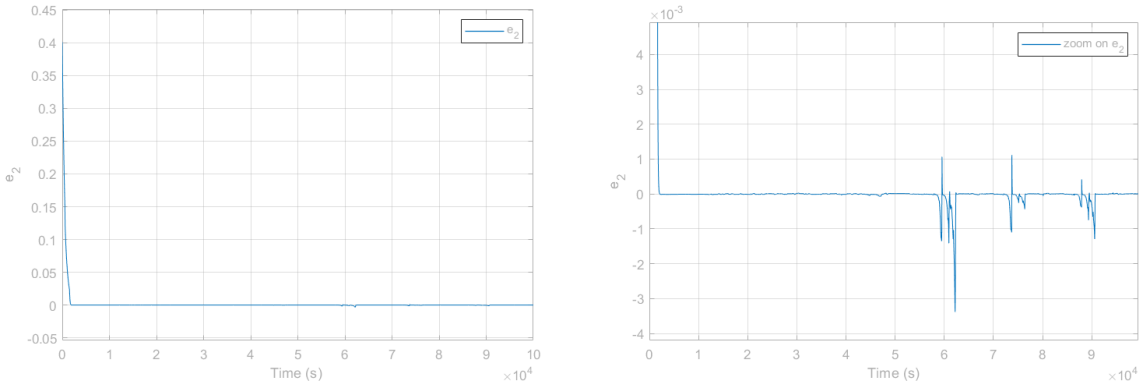

Figure 4.27: U_{RC} estimation error by the second observer, considering parameter dependencies and initial conditions within the flat region.

Similarly, we notice an increase in the U_{RC} estimation error attaining $3V$.

Figures 4.28 and 4.29 show respectively model and estimated $\tilde{y}$, and the output estimation error.

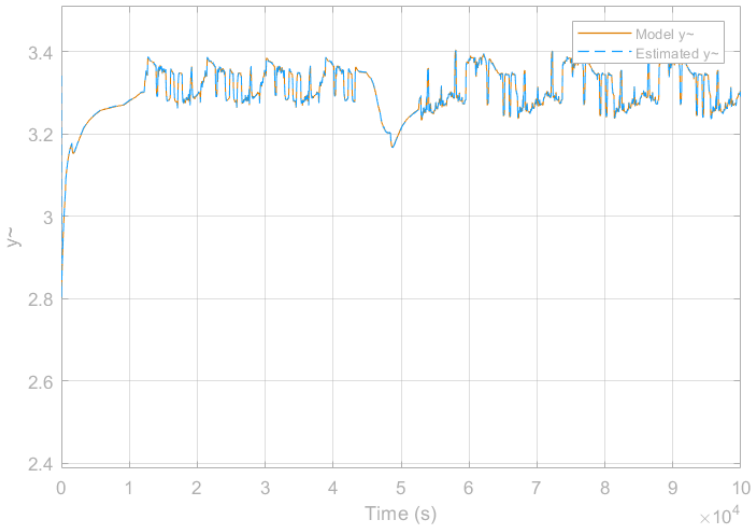

Figure 4.28: Model and estimated $\tilde{y}$ by the second observer, considering parameter dependencies and initial conditions within the flat region.

We can notice the good tracking of $\tilde{y}$.

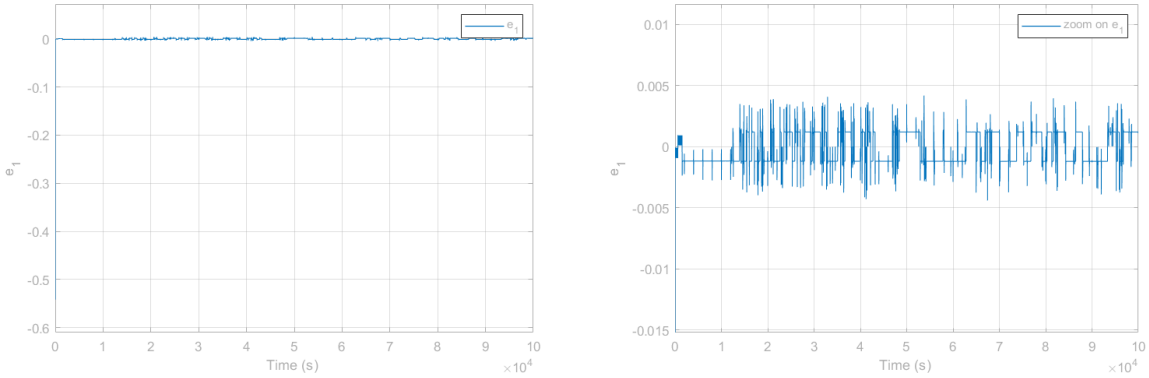

Figure 4.29: The output estimation error by the second observer, considering parameter dependencies and initial conditions within the flat region.

The output estimation error ranges between 0 and 0.005%.

4.4.2 Under measurement noise

In this section, we will show simulations conducted on the second observer under measurement noise.
First, we will consider both model and estimated SOC initial conditions outside the flat region as shown in Table 4.1.

Figures 4.30 and 4.31 show respectively model and estimated SOC, and its estimation error.

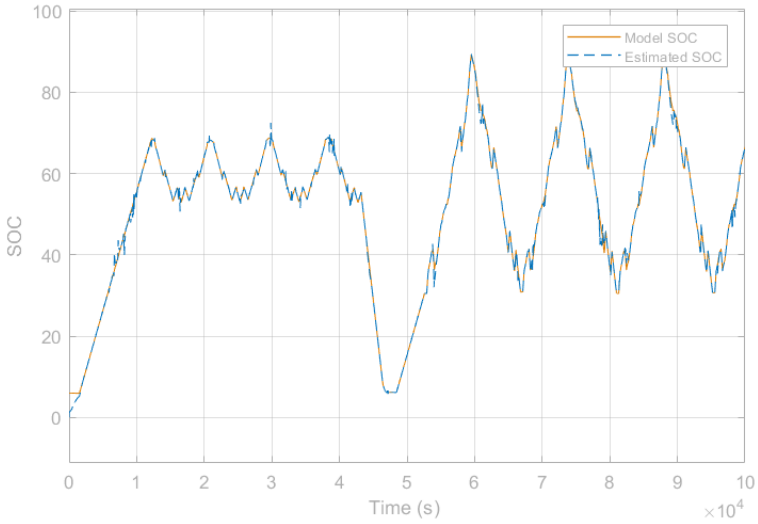

Figure 4.30: Model and estimated *SOC* by the second observer, under measurement noise, considering parameter dependencies and initial conditions outside the flat region.

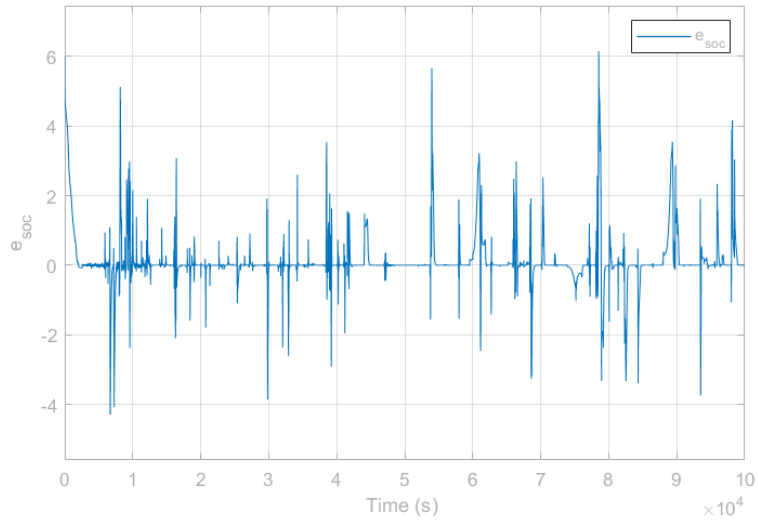

Figure 4.31: *SOC* estimation error by the second observer, under measurement noise, considering parameter dependencies and initial conditions outside the flat region.

We notice that the *SOC* estimation error increases and attains $4-6\%$ under noise.

Figures 4.32 and 4.33 show respectively model and estimated U_{RC}, and its estimation error.

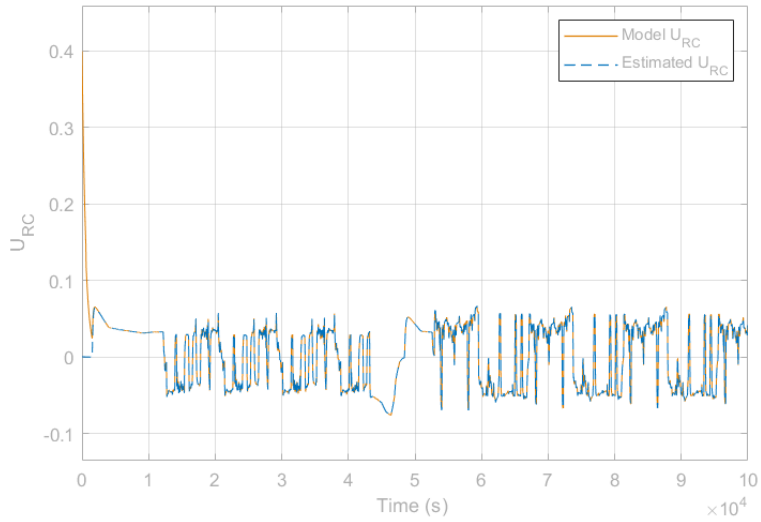

Figure 4.32: Model and estimated U_{RC} by the second observer, under measurement noise, considering parameter dependencies and initial conditions outside the flat region.

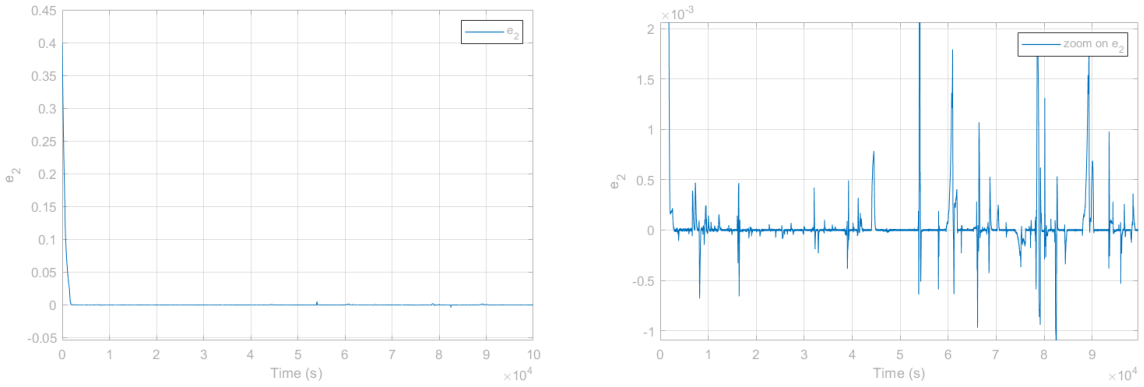

Figure 4.33: U_{RC} estimation error by the second observer, under measurement noise, considering parameter dependencies and initial conditions outside the flat region.

The U_{RC} estimation error is on the order of $10^{-3}V$.

Figures 4.34 and 4.35 show respectively model and estimated $\tilde{y}$, and the output estimation error.

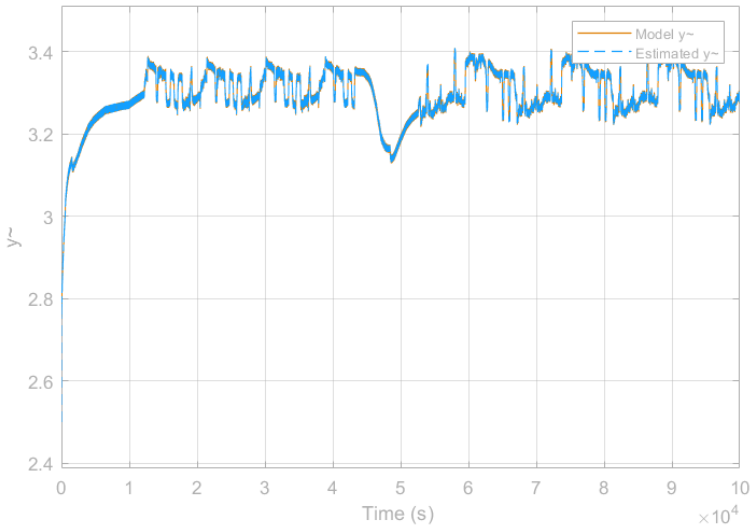

Figure 4.34: Model and estimated $\tilde{y}$ by the second observer, under measurement noise, considering parameter dependencies and initial conditions outside the flat region.

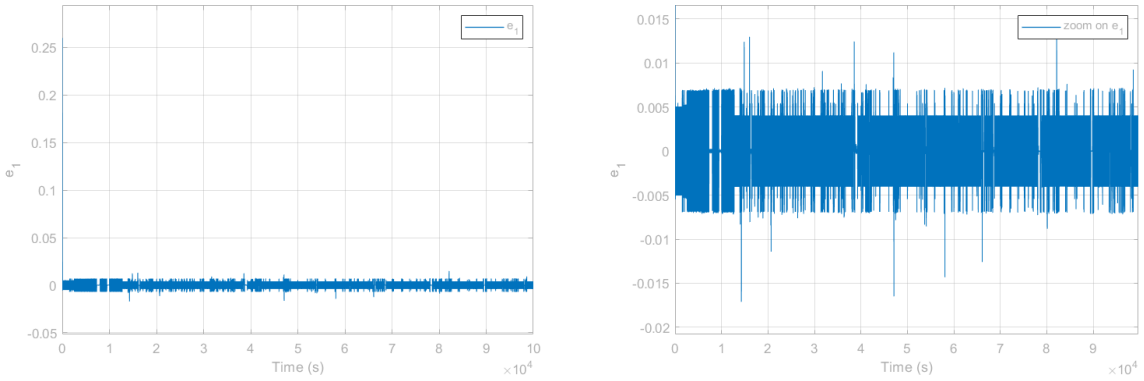

Figure 4.35: The output estimation error by the second observer, under measurement noise, considering parameter dependencies and initial conditions outside the flat region.

The output estimation error slightly increases and attains $0.01V$.

Next, we will consider both model and estimated SOC initial conditions within the flat region.

Figures 4.36 and 4.37 show respectively model and estimated SOC, and its estimation error.

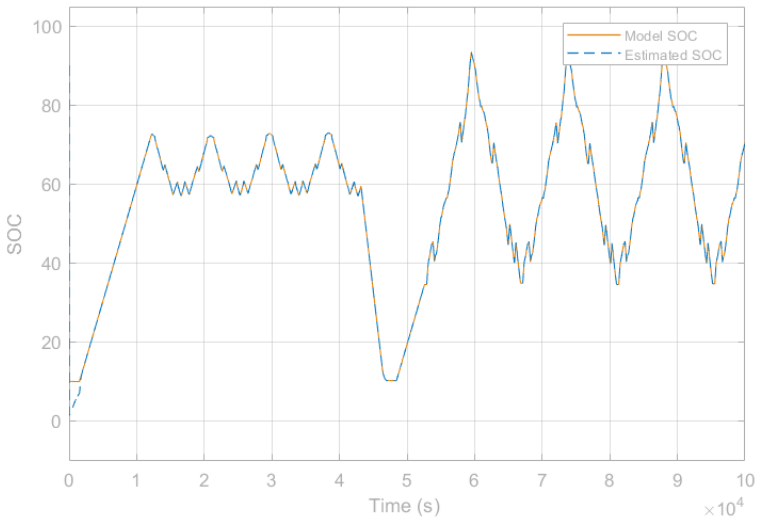

Figure 4.36: Model and estimated *SOC* by the second observer, under measurement noise, considering parameter dependencies and initial conditions within the flat region.

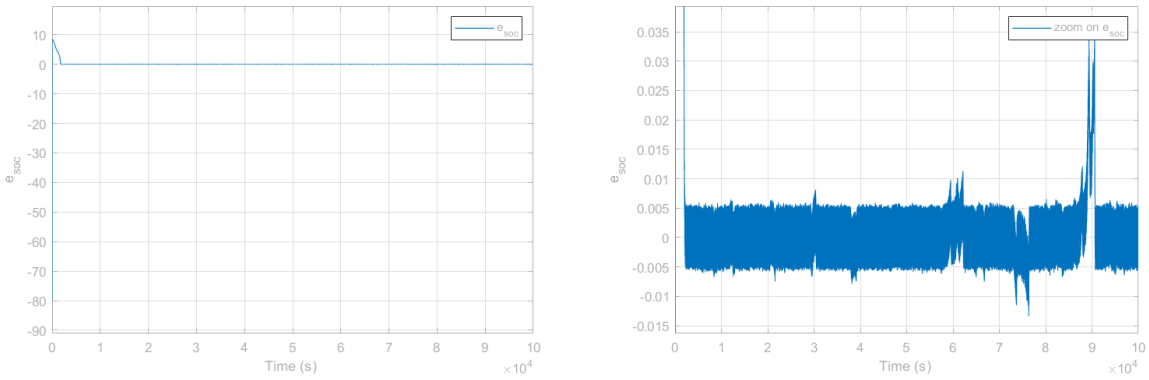

Figure 4.37: *SOC* estimation error by the second observer, under measurement noise, considering parameter dependencies and initial conditions within the flat region.

The *SOC* estimation error ranges between 0% and 0.04%.

Figures 4.38 and 4.39 show respectively model and estimated U_{RC}, and its estimation error.

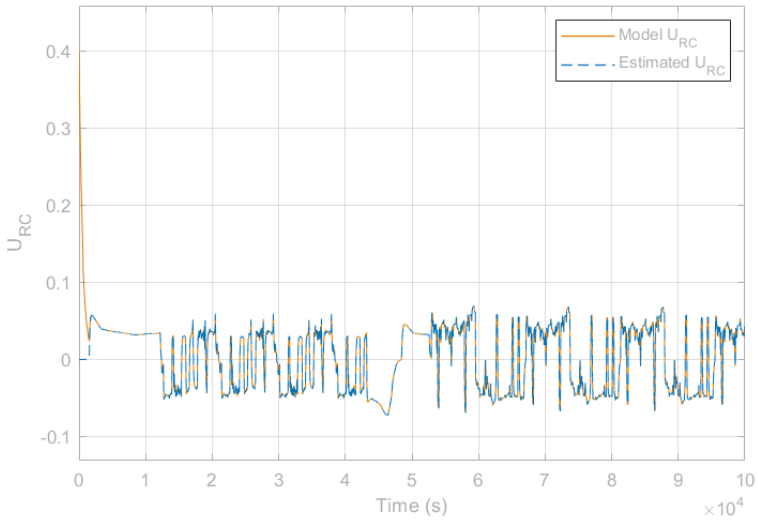

Figure 4.38: Model and estimated U_{RC} by the second observer, considering parameter dependencies and initial conditions within the flat region.

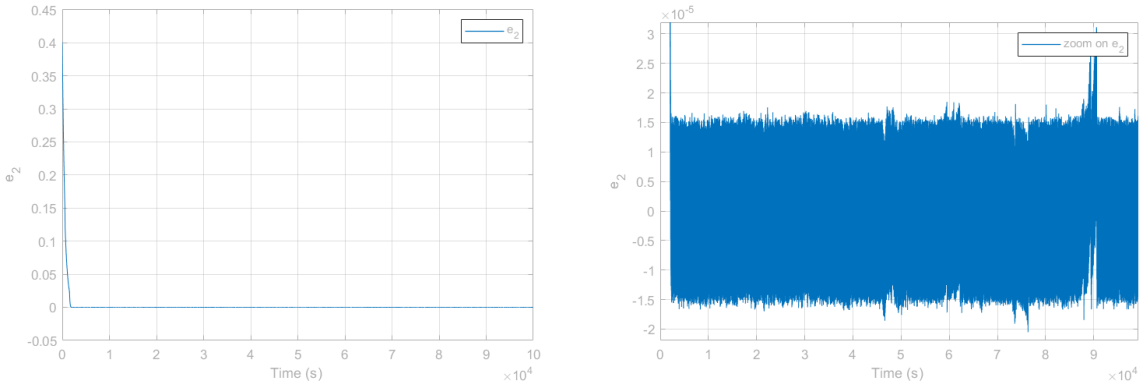

Figure 4.39: U_{RC} estimation error by the second observer, considering parameter dependencies and initial conditions within the flat region.

The U_{RC} estimation error is on the order of $10^{-4}V$.

Figures 4.40 and 4.41 show respectively model and estimated $\tilde{y}$, and the output estimation error.

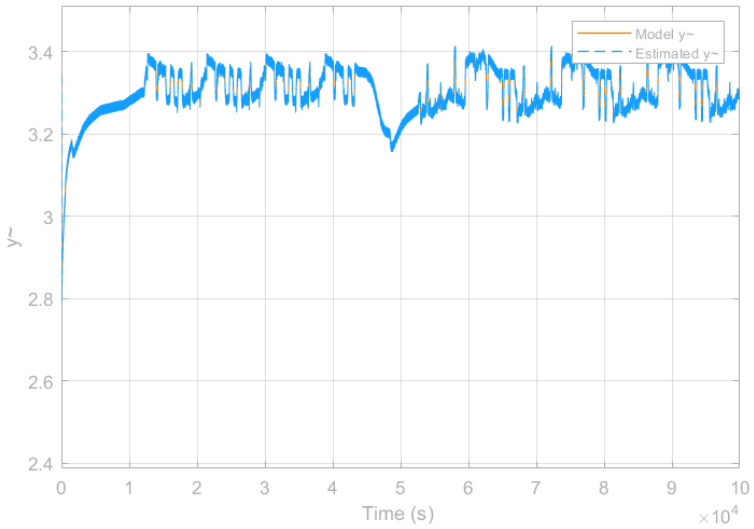

Figure 4.40: Model and estimated $\tilde{y}$ by the second observer, considering parameter dependencies and initial conditions within the flat region.

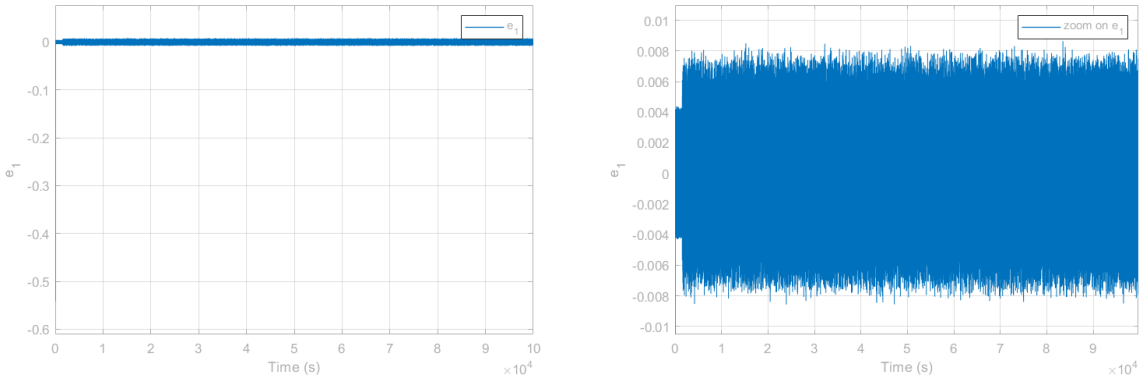

Figure 4.41: The output estimation error by the second observer, considering parameter dependencies and initial conditions within the flat region.

The output estimation error slightly increases and attain $0.008V$.

We have observed that the alternative SMO method does not maintain its performance when confronted with parameter dependencies, particularly in the presence of noise, which leads to an increase in estimation errors.

4.5 Comparison of the two observers

We have developed two distinct sliding mode observers. The first is a conventional SMO, which primarily focuses on driving the output error to zero ($e_1 = \tilde{y} - \hat{\tilde{y}} = 0$). In contrast, the second observer is an alternative SMO designed not only to achieve output error convergence but also to utilize the estimated OCV and enforce its convergence to the OCV corresponding to the estimated SOC ($\hat{V}_{oc} = V_{oc}(\widehat{SOC})$).

In Chapter 3, under the assumption of constant parameters, both SMOs demonstrated robust performance, exhibiting precise state variable tracking and minimal estimation errors, even in the presence of measurement noise. Notably, the alternative SMO exhibited faster convergence and a swifter arrival at the sliding surface than the conventional SMO.

However, in Chapter 4, when considering parameter dependencies on current, temperature, and SOC, we observed that the first SMO continued to yield commendable results with minimal estimation errors, even in the presence of measurement noise. On the other hand, the second SMO, while still achieving rapid convergence and quicker arrival at the sliding surface, did not maintain the same level of performance as with constant parameters, particularly when confronted with measurement noise.

4.6 Conclusion

In this chapter, we have undertaken an evaluation of the accuracy and robustness of the two observers introduced in Chapter 3. Our investigation accounts for the parameter dependencies on current, temperature, and SOC. Through extensive numerical simulations involving diverse SOC initial conditions, both within and outside the flat region, and conducted under conditions with and without measurement noise, we sought to comprehensively assess their performance.

Our findings reveal the robustness and reliability of the conventional SMO. Even when real parameters are introduced, this observer continues to exhibit consistent and minimal estimation errors across all scenarios. While there is a slight uptick in errors in the presence of measurement noise, they remain well within acceptable limits.

In contrast, the alternative SMO, while demonstrating impressive speed in convergence, exhibits a decrease in performance when confronted with real parameters, particularly in scenarios involving measurement noise. It falls short in accurately tracking the true values across all conditions.

These insights underscore the resilience and stability of the conventional SMO, making it a dependable choice for SOC estimation under varied conditions. However, the alternative SMO, although swift in convergence, requires further refinement to maintain its accuracy, particularly when faced with the challenges posed by real parameter variations and measurement noise.

Conclusions

In this project, our primary objective was to improve the State of Charge (SOC) estimation for LFP batteries in order to enhance their overall lifespan.

In Chapter 1, we established a foundational understanding of Lithium-ion batteries, with a specific emphasis on LFP batteries. We delved into their composition, operational principles, and conducted a comparative analysis of their advantages and disadvantages in relation to other battery types.

Chapter 2 immersed us in the world of Lithium-ion battery modeling. We introduced two prominent modeling approaches commonly found in literature, highlighting their respective strengths and weaknesses. Additionally, we selected a model that best suited our study and performed simulations to gain familiarity with its key variables.

Chapter 3 focused on exploring the observability regions within the Open Circuit Voltage (OCV) function. To achieve this, we developed two sliding mode observers, primarily designed for SOC estimation. Leveraging their finite-time convergence characteristics and assuming constant parameters, we conducted a Lyapunov analysis prior to numerical simulations. The first observer, a conventional SMO based on output estimation error convergence, demonstrated promising results across various initial conditions, even in the presence of measurement noise. The SOC estimation error remained consistently below 1

Chapter 4 sought to evaluate the accuracy of both observers by relaxing the assumption of constant parameters and accounting for their dependencies on the current, the temperature, and the SOC. The conventional SMO maintained its performance, offering reliable results across different initial conditions, even when dealing with measurement noise. However, the alternative SMO, despite its faster convergence, did not consistently track states under various initial conditions, particularly in the presence of measurement noise.

Overall, this work contributes significantly to prolonging the lifespan of LFP batteries by providing precise state of charge estimations to BMS. Particularly noteworthy is the fact that, in the existing literature, Sliding Mode Observers (SMOs) have not been extensively investigated for the examination of the flat Open Circuit Voltage (OCV) function in LFP batteries and their associated State of Charge (SOC) estimation.

In the future, our goal is to seamlessly incorporate these observers into the Battery Management System (BMS) software, where we will rigorously assess their effectiveness in real-world scenarios for accurate State of Charge (SOC) estimation.

The potential for improvement in this project could lie in the utilization of larger datasets than those employed in these simulations. With an expanded dataset, it becomes feasible to identify the OCV function through mathematical expressions to enhance the overall results.

Alternatively, investigating the implementation of adaptive gains for the sliding mode observers developed in this project can contribute to enhancing both the outcomes and the func-

tionality of the Battery Management System (BMS).

Bibliography

[1] Henrik Beelen, Henk Jan Bergveld **and** M. C. F. Donkers. "Joint Estimation of Battery Parameters and State of Charge Using an Extended Kalman Filter: A Single-Parameter Tuning Approach". en. **in***IEEE Transactions on Control Systems Technology*: 29.3 (**may** 2021), **pages** 1087–1101. ISSN: 1063-6536, 1558-0865, 2374-0159. DOI: 10.1109/TCST.2020.2992523.

[2] Pierre Blondel. "Estimation de l'état interne d'une batterie lithium-ion à l'aide d'un modèle électrochimique." phdthesis. Université de Lorraine, 2019.

[3] Pierre G. Blondel, Romain Postoyan, Stéphane Raël, Sébastien Benjamin **and** Phillippe Desprez. "Observer design for an electrochemical model of lithium ion batteries based on a polytopic approach". en. **in***IFAC-PapersOnLine*: 50.1 (**july** 2017), **pages** 8127–8132. ISSN: 24058963. DOI: 10.1016/j.ifacol.2017.08.1252.

[4] H. Bouchareb, K. Saqli, N.K. M'sirdi, M. Oudghiri Bentaie **and** A. Naamane. "Sliding Mode Observer Design for Battery State of Charge estimation". en. **in***2020 5th International Conference on Renewable Energies for Developing Countries (REDEC)*: Marrakech, Morocco, Morocco: IEEE, **june** 2020, **pages** 1–5. ISBN: 978-1-72815-595-1. DOI: 10.1109/REDEC49234.2020.9163592.

[5] Long Cai **and** Ralph E. White. "Mathematical modeling of a lithium ion battery with thermal effects in COMSOL Inc. Multiphysics (MP) software". en. **in***Journal of Power Sources*: 196.14 (**july** 2011), **pages** 5985–5989. ISSN: 03787753. DOI: 10.1016/j.jpowsour.2011.03.017.

[6] Min Chen **and** G.A. Rincon-Mora. "Accurate electrical battery model capable of predicting runtime and I-V performance". en. **in***IEEE Transactions on Energy Conversion*: 21.2 (**june** 2006), **pages** 504–511. ISSN: 0885-8969, 1558-0059. DOI: 10.1109/TEC.2006.874229.

[7] Xiaopeng Chen, Weixiang Shen, Zhenwei Cao **and** Ajay Kapoor. "Adaptive gain sliding mode observer for state of charge estimation based on combined battery equivalent circuit model". en. **in***Computers & Chemical Engineering*: 64 (**may** 2014), **pages** 114–123. ISSN: 00981354. DOI: 10.1016/j.compchemeng.2014.02.015.

[8] Yi-Hsien Chiang, Wu-Yang Sean **and** Jia-Cheng Ke. "Online estimation of internal resistance and open-circuit voltage of lithium-ion batteries in electric vehicles". en. **in***Journal of Power Sources*: 196.8 (**april** 2011), **pages** 3921–3932. ISSN: 03787753. DOI: 10.1016/j.jpowsour.2011.01.005.

[9] Marc Doyle, Thomas F. Fuller **and** John Newman. "Modeling of Galvanostatic Charge and Discharge of the Lithium/Polymer/Insertion Cell". en. **in***Journal of The Electrochemical Society*: 140.6 (**june** 1993), **pages** 1526–1533. ISSN: 0013-4651, 1945-7111. DOI: 10.1149/1.2221597.

[10] Jiani Du, Zhitao Liu, Youyi Wang **and** Changyun Wen. "An adaptive sliding mode observer for lithium-ion battery state of charge and state of health estimation in electric vehicles". en. **in***Control Engineering Practice*: 54 (**september** 2016), **pages** 81–90. ISSN: 09670661. DOI: 10.1016/j.conengprac.2016.05.014.

[11] Yong Feng, Chen Xue, Qing-Long Han, Fengling Han **and** Jiacheng Du. "Robust Estimation for State-of-Charge and State-of-Health of Lithium-Ion Batteries Using Integral-Type Terminal Sliding-Mode Observers". **in***IEEE Transactions on Industrial Electronics*: 67.5 (**may** 2020), **pages** 4013–4023. ISSN: 0278-0046, 1557-9948. DOI: 10.1109/TIE.2019.2916389.

[12] Xiaosong Hu, Shengbo Li **and** Huei Peng. "A comparative study of equivalent circuit models for Li-ion batteries". en. **in***Journal of Power Sources*: 198 (**january** 2012), **pages** 359–367. ISSN: 03787753. DOI: 10.1016/j.jpowsour.2011.10.013.

[13] Y. Hu, S. Yurkovich, Y. Guezennec **and** B.J. Yurkovich. "A technique for dynamic battery model identification in automotive applications using linear parameter varying structures". en. **in***Control Engineering Practice*: 17.10 (**october** 2009), **pages** 1190–1201. ISSN: 09670661. DOI: 10.1016/j.conengprac.2009.05.002.

[14] Y. Hu, S. Yurkovich, Y. Guezennec **and** B.J. Yurkovich. "Electro-thermal battery model identification for automotive applications". en. **in***Journal of Power Sources*: 196.1 (**january** 2011), **pages** 449–457. ISSN: 03787753. DOI: 10.1016/j.jpowsour.2010.06.037.

[15] Hassan K. Khalil. *Nonlinear systems*. en. 3rd ed. Upper Saddle River, N.J: Prentice Hall, 2002. ISBN: 978-0-13-067389-3.

[16] Il-Song Kim. "The novel state of charge estimation method for lithium battery using sliding mode observer". en. **in***Journal of Power Sources*: 163.1 (**december** 2006), **pages** 584–590. ISSN: 03787753. DOI: 10.1016/j.jpowsour.2006.09.006.

[17] N. Legrand, S. Raël, B. Knosp, M. Hinaje, P. Desprez **and** F. Lapicque. "Including double-layer capacitance in lithium-ion battery mathematical models". en. **in***Journal of Power Sources*: 251 (**april** 2014), **pages** 370–378. ISSN: 0378-7753. DOI: 10.1016/j.jpowsour.2013.11.044.

[18] Jiahao Li, Joaquin Klee Barillas, Clemens Guenther **and** Michael A. Danzer. "A comparative study of state of charge estimation algorithms for LiFePO4 batteries used in electric vehicles". en. **in***Journal of Power Sources*: 230 (**may** 2013), **pages** 244–250. ISSN: 03787753. DOI: 10.1016/j.jpowsour.2012.12.057.

[19] KaiChin Lim, Hany Ayad Bastawrous, Van-Huan Duong, Khay Wai See, Peng Zhang **and** Shi Xue Dou. "Fading Kalman filter-based real-time state of charge estimation in LiFePO4 battery-powered electric vehicles". en. **in***Applied Energy*: 169 (**may** 2016), **pages** 40–48. ISSN: 03062619. DOI: 10.1016/j.apenergy.2016.01.096.

[20] Xinfan Lin, Hector E. Perez, Shankar Mohan, Jason B. Siegel, Anna G. Stefanopoulou, Yi Ding **and** Matthew P. Castanier. "A lumped-parameter electro-thermal model for cylindrical batteries". en. **in***Journal of Power Sources*: 257 (**july** 2014), **pages** 1–11. ISSN: 03787753. DOI: 10.1016/j.jpowsour.2014.01.097.

[21] Kong Soon Ng, Chin-Sien Moo, Yi-Ping Chen **and** Yao-Ching Hsieh. "Enhanced coulomb counting method for estimating state-of-charge and state-of-health of lithium-ion batteries". en. **in***Applied Energy*: 86.9 (**september** 2009), **pages** 1506–1511. ISSN: 03062619. DOI: 10.1016/j.apenergy.2008.11.021.

[22] Kong-Soon Ng, Chin-Sien Moo, Yi-Ping Chen **and** Yao-Ching Hsieh. "State-of-charge estimation for lead-acid batteries based on dynamic open-circuit voltage". en. **in***2008 IEEE 2nd International Power and Energy Conference*: Johor Bahru, Malaysia: IEEE, **december** 2008, **pages** 972–976. ISBN: 978-1-4244-2404-7. DOI: 10.1109/PECON.2008.4762614.

[23] Gregory L. Plett. *Battery management systems*. en. Artech House Power engineering series. Boston: Artech house, 2016. ISBN: 978-1-63081-027-6.

[24] Stephane Rael. *cours-batteries-2022-2023*.

[25] S. Raël **and** M. Hinaje. "Using electrical analogy to describe mass and charge transport in lithium-ion batteries". en. **in***Journal of Power Sources*: 222 (**january** 2013), **pages** 112–122. ISSN: 03787753. DOI: 10.1016/j.jpowsour.2012.08.071.

[26] Kandler Smith **and** Chao-Yang Wang. "Power and thermal characterization of a lithium-ion battery pack for hybrid-electric vehicles". en. **in***Journal of Power Sources*: 160.1 (**september** 2006), **pages** 662–673. ISSN: 0378-7753. DOI: 10.1016/j.jpowsour.2006.01.038.

[27] Sarah K. Spurgeon. "Sliding mode observers: a survey". en. **in***International Journal of Systems Science*: 39.8 (**august** 2008), **pages** 751–764. ISSN: 0020-7721, 1464-5319. DOI: 10.1080/00207720701847638.

[28] Xin Sui, Shan He, Daniel-Ioan Stroe, Xinrong Huang, Jinhao Meng **and** Remus Teodorescu. "A review of sliding mode observers based on equivalent circuit model for battery SoC estimation". en. **in***2019 IEEE 28th International Symposium on Industrial Electronics (ISIE)*: Vancouver, BC, Canada: IEEE, **june** 2019, **pages** 1965–1970. ISBN: 978-1-72813-666-0. DOI: 10.1109/ISIE.2019.8781412.

[29] Xiaopeng Tang, Yujie Wang **and** Zonghai Chen. "A method for state-of-charge estimation of LiFePO4 batteries based on a dual-circuit state observer". en. **in***Journal of Power Sources*: 296 (**november** 2015), **pages** 23–29. ISSN: 03787753. DOI: 10.1016/j.jpowsour.2015.07.028.

[30] Jinpeng Tian, Rui Xiong, Weixiang Shen **and** Jiahuan Lu. "State-of-charge estimation of LiFePO4 batteries in electric vehicles: A deep-learning enabled approach". en. **in***Applied Energy*: 291 (**june** 2021), **page** 116812. ISSN: 03062619. DOI: 10.1016/j.apenergy.2021.116812.

[31] V. I. Utkin. *Sliding mode and their application in variable structure systems*. Moscow, 1978.

[32] Chunyu Wang, Naxin Cui, Miao Liu **and** Chenghui Zhang. "A new state of charge estimation method for lithium-ion battery based on sliding mode observer". en. **in***2017 IEEE Energy Conversion Congress and Exposition (ECCE)*: Cincinnati, OH: IEEE, **october** 2017, **pages** 5625–5630. ISBN: 978-1-5090-2998-3. DOI: 10.1109/ECCE.2017.8096936.

[33] Yinjiao Xing, Eden Ma, Kwok-Leung Tsui **and** Michael Pecht. "Battery Management Systems in Electric and Hybrid Vehicles". **in***Energies*: 4 (**december** 2011). DOI: 10.3390/en4111840.

[34] B Yannliaw. "Modeling of lithium ion cells?A simple equivalent-circuit model approach". en. **in***Solid State Ionics*: 175.1-4 (**november** 2004), **pages** 835–839. ISSN: 01672738. DOI: 10.1016/j.ssi.2004.09.049.